Time Domain Analysis of a Floating Ice Sheet due to a Moving Load over Different Types of Sea-beds

by

Mahesh Kumar Nehra

DEPARTMENT OF MATHEMATICS
INDIAN INSTITUTE OF TECHNOLOGY GUWAHATI
GUWAHATI-781039, ASSAM, INDIA
December, 2025

Time Domain Analysis of a Floating Ice Sheet due to a Moving Load over Different Types of Sea-beds

A Thesis Submitted
in Partial Fulfillment of the Rrequirements
for the Degree of

DOCTOR OF PHILOSOPHY

by

Mahesh Kumar Nehra

(Roll No: 206123102)

DEPARTMENT OF MATHEMATICS

INDIAN INSTITUTE OF TECHNOLOGY GUWAHATI

GUWAHATI-781039, ASSAM, INDIA

December, 2025

Dedicated To My Beloved
Grandparents
Smt. Patasi Devi
and
Shri Rameshwar Lal Nehra

Declaration

I do hereby declare that this thesis entitled **Time Domain Analysis of a Floating Ice Sheet due to a Moving Load over Different Types of Sea-beds** is a presentation of my original research work done under the supervision of **Dr. Swaroop Nandan Bora**, Professor, Department of Mathematics, Indian Institute of Technology Guwahati for the award of the degree of Doctor of Philosophy and this work has not been submitted elsewhere for a degree.

December, 2025

Mahesh Kumar Nehra
Roll No. 206123102
Department of Mathematics
Indian Institute of Technology Guwahati


भारतीय प्रौद्योगिकी संस्थान गुवाहाटी
Indian Institute of Technology Guwahati

Certificate

It is to certify that the work contained in this thesis entitled **Time Domain Analysis of a Floating Ice Sheet due to a Moving Load over Different Types of Sea-beds** has been carried out by **Mahesh Kumar Nehra**, a student in the Department of Mathematics, Indian Institute of Technology Guwahati, under my supervision for the award of the degree of Doctor of Philosophy and this work has not been submitted elsewhere for a degree.

December, 2025

Dr. Swaroop Nandan Bora
Professor
Department of Mathematics
Indian Institute of Technology Guwahati

Acknowledgements

The path to completing a PhD thesis is demanding and filled with countless challenges. This achievement would not have been possible without the unwavering support and guidance of numerous individuals. I am sincerely thankful to everyone who contributed to this academic journey. I take this opportunity to express my sincere gratitude to all of them.

I am deeply grateful to God for giving me strength, resilience, and the clarity of mind that helped me pursue and complete my Ph.D.

My heartfelt thanks go to my thesis supervisor, Prof. Swaroop Nandan Bora, whose mentorship, encouragement, and valuable suggestions shaped this thesis. I feel privileged to have worked as a research scholar under his supervision. His patience and steady support helped me navigate every challenge in this journey. He motivated me to pursue my work with dedication while giving me the independence to develop my ideas. His vast knowledge played a key role in the progress of my research. I am truly grateful for his continuous support and guidance in all aspects of my academic life. Thank you so much, Sir!

I sincerely extend my gratitude to the members of my Doctoral Committee, Prof. Durga Charan Dalal, Prof. Natesan Srinivasan and Prof. Bhupen Deka, for their constant encouragement, constructive feedback, and insightful suggestions throughout my Ph.D. journey, which significantly enhanced the quality of my research. I would also like to express my heartfelt thanks to all the faculty members of the department for their support and guidance during my research work.

I would like to extend my heartfelt thanks to my friends and seniors Dr. Kuldeep, Dr. Koushik, Dr. Raman, Dr. Gouranga, Dr. Shiva, Dr. Matap, Dr. Shilpi, Dr. Abhijit, Sunil, Mandeep, Rahul, Nabanita, Sohini, Smriti, Karabee, Sumit for their constant support and encouragement throughout my journey. My special gratitude goes to my close friends Sunil, Mandeep, Rahul and Sonam with whom I have shared some of the most memorable moments of my time at this campus. I am truly fortunate to have worked and grown alongside all of you over the years, and I deeply appreciate your companionship and support during my stay at IIT Guwahati. Additionally, I am grateful to my friends Shankar Lal, Subhash Bhamu, Rajendra Sou, Lokesh Barala, whose encouragement, care, and unwavering support have inspired me to persevere at every step of this journey and beyond.

I am deeply grateful to my parents, Smt. Durga Devi and Shri Laxman Singh Nehra, for their unconditional love, care, and encouragement, which have been the foundation of my strength and perseverance throughout life. I am also thankful to my family members Madan Lal, Manohari Devi, Raju, Pinky, Komal, Nisha, Vishesh, Nimmi and Navya, for their constant care, support, and affection, which have always inspired and motivated me. Their presence has been a source of comfort and strength at every stage of this journey, and I dedicate this thesis to them. I also extend my heartfelt thanks to all other family members for their blessings, love, and encouragement throughout my life.

I would like to acknowledge the joy and laughter that have brightened my journey. Special thanks to the characters from the epic TV series *Taarak Mehta Ka Ooltah Chashmah*, especially Jethalal Champaklal Gada, whose humor and lightheartedness brought smiles and moments of relief during the most stressful days of my research.

I am also immensely grateful to the Ministry of Education (earlier known as the Ministry of Human Resource Development), Government of India for providing me financial assistance to pursue my research. I would like to thank Indian Institute of Technology Guwahati for providing me various facilities to carry out my research work.

December, 2025 **Mahesh Kumar Nehra**


भारतीय प्रौद्योगिकी संस्थान गुवाहाटी
Indian Institute of Technology Guwahati

Abstract

This thesis presents a comprehensive investigation into the dynamic response of a floating ice sheet subjected to moving loads under diverse physical and environmental conditions. The study systematically examines the influences of a porous sea-bed, an undulating sea-bed, a flexible sea-bed and a trench shaped sea-bed in the presence/absence of uniform current and a variable-speed moving load. These factors are analyzed to understand their effects on wave propagation, ice deflection, and steady-state behavior within ice-water interaction systems.

The governing equations are formulated based on linear potential flow theory, assuming an incompressible, inviscid fluid undergoing an irrotational motion. Analytical and semi-analytical techniques such as the Fourier transform, Laplace-Fourier transform and asymptotic methods are employed to solve the governing equations and derive expressions for the ice sheet deflection under concentrated point or line loads moving at constant or variable speeds. The dispersion relation is established for each case, serving as a foundation to study the variations in phase and group speeds, and to interpret the steady and transient responses of the ice sheet.

For the porous sea-bed, both the sea-bed permeability and the internal stress are found to significantly alter wave generation and propagation in the floating ice sheet. Variations in these parameters lead to noticeable changes in the dispersion characteristics, as well as in the phase and group speeds of the flexural-gravity waves. The long-time response of the ice sheet shows that steady deflection states occur for both subcritical and supercritical load speed regimes, while a growing response develops near a critical speed.

In the case of an undulating sea-bed, the interaction between the moving load and the sinusoidal bottom topography results in the occurrence of Bragg resonance. The ice sheet deflection is found to depend strongly on the load speed and the characteristics of the bottom undulation. As the number of ripples in the undulating sea-bed increases, the ice sheet behavior approaches that corresponding to a flat sea-bed.

When a flexible sea-bed and a uniform current are considered, strong interactions between the current dynamics and sea-bed elasticity are observed. These interactions lead to significant modifications in wave dispersion, phase and group speeds, and ice sheet deflection. Changes in the elastic properties of the sea-bed and the strength of the current result in considerable variations in wave propagation due to the moving load.

A further study considers a moving load distributed over a finite length with harmonic time dependence, traveling over a floating ice sheet in the presence of a uniform current. We consider that the load moves with variable speed, including cases of constant speed as well as phases of uniform acceleration and deceleration. The ice sheet deflection is obtained in integral form using Laplace and Fourier transform techniques. The resulting integrals exhibit singularities when the load moves at a constant speed, which play a dominant role in determining the ice response. In contrast, such singularities are absent when the load undergoes uniform acceleration or deceleration, leading to distinct deformation patterns for different moving characteristics.

The response of a floating ice sheet over a rectangular trench-shaped sea-bed is also examined for a concentrated load moving at a constant speed. The governing equations are formulated in a moving coordinate system, and the fluid domain is divided into multiple regions corresponding to the trench geometry. The matching of boundary conditions across these regions leads to a system of algebraic equations, whose numerical solutions provide the steady-state deflection profiles. The results show pronounced effects of trench geometry on wave formation, with significant changes in the amplitudes of the waves.


भारतीय प्रौद्योगिकी संस्थान गुवाहाटी
Indian Institute of Technology Guwahati

Contents

List of Figures

List of Tables

CHAPTER 1

Introduction

1.1 Preamble

A fluid is a substance that continuously deforms when subjected to shear stress and does not retain a fixed shape of its own. Fluid mechanics is the discipline of science that addresses the behavior of fluids, including liquids and gases, at rest and in motion, as well as their interactions with boundaries, such as solid surfaces or different fluids. This field of study is invaluable for modern multidisciplinary research in engineering and applied sciences. Fluid mechanics has a wide range of applications: blood circulates through veins and arteries, the human heart functions as a pump, and fluid principles are used in processes such as breathing, swimming, and the operation of fans, wind turbines, airplanes, ships, missiles, jets, sprinklers, pipelines, etc. Events that happen naturally like rainfall, weather patterns, groundwater movement, ocean currents, and wave propagation are all subject to fluid motions. The analysis of fluid behavior is based on fundamental mechanical laws such as mass, momentum, and energy conservation. The continuum hypothesis is used to describe fluid properties, such as density, viscosity, volume, pressure, and temperature, which assume that these properties vary smoothly as point functions without abrupt discontinuities as long as the system size is much larger than the gaps between molecules. Since the outermost fluid molecules have a tendency to stick to the solid surface, fluids at solid surfaces follow the no-slip condition, which means that the fluid in contact with the boundary has the same velocity as the boundary itself.

Fluid motion can be characterized in two different manners. The first is the Lagrangian approach, which tracks the motion of each individual fluid particle from its starting position as it moves through space and time. The second method is the Eulerian approach, which focuses on specific points in space, and investigates how fluid parameters like velocity, pressure, and temperature vary as the flow passes through them. The Eulerian approach is more frequently employed to analyze real-world fluid flow complications, even though the Lagrangian approach has its uses, particularly in particle tracking and multiphase flows. The Eulerian analogy for fluid motion uses three types of curves to describe and explain flow behavior: streamlines, pathlines, and streaklines. A streamline is a curve that is tangent to the velocity vector at every point in time and represents the instantaneous direction of flow. A pathline represents the actual route of a single fluid particle as it passes through the flow field. A streakline is formed by combining the positions of all particles that pass through a given point in the flow. These curves are frequently used in experiments to visualize motion, such as when dye or seed particles are introduced. While streamlines, pathlines, and streaklines overlap in steady flow conditions, they diverge and provide unique insights into fluid dynamics in unsteady flows.

One important characteristic of fluids that indicates their resistance to shear stress is their viscosity. The idea of an ideal fluid is the starting point for many theoretical investigations in fluid mechanics. Adjacent layers in an ideal fluid only apply normal forces, like pressure, to one another rather than tangential forces, or shear stresses. This indicates that there is no internal resistance in an ideal fluid. The presence of these tangential forces illustrates the impact of viscosity, whereas a real fluid experiences both normal and tangential stresses. A number of characteristics can be used to categorize fluid motion. The flow is called *inviscid* or *non-viscous* if viscosity can be ignored; otherwise, it is called *viscous*. When pressure or temperature changes cause a significant change in density or volume, the flow is *compressible*; when these changes are minimal, the flow is *incompressible*. The ratio of flow velocity to the local speed of sound, or Mach number, aids in distinguishing between compressible and incompressible flows. A flow is said to be *steady* if its characteristics do not change over time at certain points; if they do, the flow is said to be *unsteady*. Flow can also be classified as *turbulent* when it shows chaotic motion, recirculation, and irregular variations. The flow is termed *laminar* if it flows smoothly in layers without mixing, i.e., no turbulence exists. Shear stress and rate of strain have a nearly linear relationship in Newtonian fluids (like water and air) but not in non-Newtonian fluids (like blood and honey). Subsonic, transonic, and hypersonic flows can also be distinguished by their Mach number.

Rotation is used for another classification used for different flows. When the curl of a flow field with velocity vector $\overrightarrow{U}$ is zero, it is referred to as *irrotational flow*; otherwise, it is called a *rotational flow*. When the flow is irrotational, a scalar function Φ exists, and this function is known as the *velocity potential*. Laplace's equation, the continuity equation for potential flow, is satisfied by the velocity potential for irrotational and incompressible flows.

In physics, mathematics, and other fields of science, a wave is described as a disturbance or oscillation that causes a transient displacement from an equilibrium state. Because of this disturbance, energy can go through a medium or space without causing any net movement of matter. The two primary categories of waves are *mechanical waves* and *electromagnetic waves*.

A material medium is essential for the transmission of a mechanical wave, in which the changes in stress and strain are caused by oscillations of the particles of the medium around their equilibrium positions. Water waves, sound waves and seismic activity are common examples. An electromagnetic wave moves across the space at the speed of light and is made up of time-varying electric and magnetic fields, which do not require a medium. X-rays, gamma rays, ultraviolet rays, visible light, infrared radiation, and radio waves are a few examples.

The direction of particle motion in relation to the direction of wave propagation is another way to categorize waves. In a longitudinal wave (sound wave), particles of the medium vibrate parallel to the direction of propagation. On the other hand, in a transverse wave (light wave), the particle motion is perpendicular to the wave direction.

A familiar example of water waves is the one when a stone is thrown into a pond, generating ripples that spread outward from the source of disturbance. Other examples include wind-generated ripples on the surface of lakes or oceans, as well as waves generated by ships moving through water. The oscillation amplitudes of these waves are often small. On the other hand, larger waves including tsunamis, rogue waves and tidal waves, have noticeably larger amplitudes. Huge amounts of energy are carried by these waves, which frequently cause serious damage to coasts, offshore infrastructure, and hazard to floating vessels. The study of wave-structure interaction has become a crucial field in fluid mechanics to address these issues.

The study of water wave theory dates back to several centuries. A detailed historical account can be found in Craik (2004). The earliest known attempt was made by Sir Isaac Newton, who introduced a preliminary theory of water waves. In Principia, Book II, Prop. XLV (1687), he suggested an analogy with oscillations in a U–tube and correctly deduced that the frequency of deep-water waves is inversely proportional to the square root of the breadth of the wave. This reasoning was later revisited by Wilhelm-Jacobs Gravesande (1721) and Charles Bossut (1786), who repeated Newton's argument. Subsequently, Joseph Louis Lagrange (1781, 1786) advanced the theory by deriving the linearized governing equations for small-amplitude waves and obtaining solutions for long plane waves in shallow water. A similar formulation later appeared in his Mécanique Analytique (1788). For shallow-water waves, Lagrange (1786) proposed that the propagation speed could be expressed as the velocity acquired by a falling body through half the water depth, i.e., $\sqrt{gH}$, where g represents gravitational acceleration and H denotes the fluid depth. Before the 19th century, several additional contributions were made. Notably, M. Flaugergues (1793) and Francois de la Coudraye (1796) conducted significant studies on wave motion, which were later synthesized and summarized by Weber and Weber (1825).

The earliest exact nonlinear solution for finite-amplitude waves in deep water was introduced by Franz Joseph von Gerstner (1802). However, because the motion described in his formulation was not generally irrotational, the Gerstner wave solution received little attention for a long period and has often been regarded more as a mathematical curiosity than a result of direct practical significance. Much later, W.J. Macquorn Rankine (1863) independently rediscovered the solution, thereby reviving interest in the subject.

A significant milestone in the development of water wave theory occurred in 1813, when the French Académie des Sciences announced a prize competition on the propagation of surface waves in a fluid of infinite depth. In response, Augustin-Louis Cauchy, at the age of 25, submitted his entry in July 1815. Shortly afterward, one of the judges, Siméon Denis Poisson, also produced a memoir presenting his independent findings. The prize was awarded to Cauchy in 1816, while Poisson's work was published in 1818. Cauchy's full contribution, enriched with approximately 188 pages of supplementary notes, was eventually published in 1827, reflecting the depth and breadth of his analysis.

Later, Horace Lamb included the Cauchy-Poisson analysis in his influential text *Hydrodynamics*. In the first edition of the book published in 1895, the treatment was relatively brief, incomplete, and restricted primarily to two-dimensional disturbances. However, in the fourth edition in 1916, Lamb provided a significantly expanded and more comprehensive account. The Cauchy-Poisson analysis is now widely recognized as a fundamental development in the mathematical formulation of initial value problems in wave theory.

In 1825, Ernst Heinrich Weber and Wilhelm Eduard Weber published their influential work *Wellenlehre auf Experimente gegrundet* in Leipzig. This text presented their systematic laboratory investigations on plane periodic wave trains in a channel, accompanied by critical commentary on the theoretical studies available at the time. Subsequently, Russell and Robinson (1837) produced a remarkable study on wave phenomena in oceans, rivers, and canals. Through experiments, they identified the nonlinear solitary wave, a discovery of lasting significance. Their work categorized waves into four distinct types: (i) waves of translation, which included the newly observed solitary waves along with tides and bores; (ii) oscillatory or periodic wave trains; (iii) capillary waves; and (iv) corpuscular waves, identified as compressional sound waves in water.

In the following year, Green (1838) presented an analytical treatment of the influence of slow variations in depth and width, focusing on the case of long linear shallow-water waves. Around the same period, Kelland (1840) investigated wave motion in fluids of finite depth under the assumption of parallel sections, correctly deriving the expression for wave speed. In 1847, Earnshaw (1847) explored the representation of solitary waves using discontinuous functions. He highlighted the persistent difficulties in obtaining general solutions to the governing hydrodynamic equations and stressed the necessity of restricting theoretical

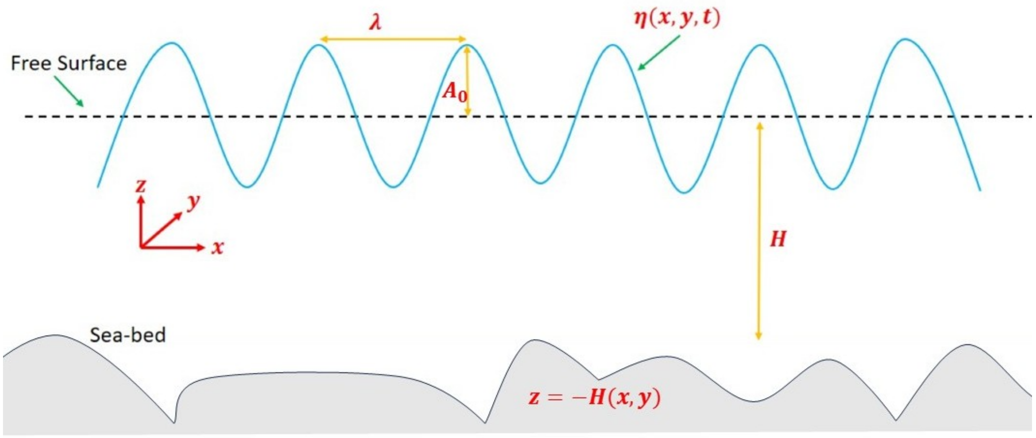

Figure 1.1: Schematic diagram of wave propagation

models to simplified classes of motion inspired by experimental observations. Although his attempt at a nonlinear theory ultimately failed, it was later advanced by Stokes (1847), who developed a more rigorous framework. Subsequently, Rayleigh (1876) not only provided an accurate approximate solution, but also demonstrated that Earnshaw's formulation did not describe an irrotational flow.

Earlier, in 1841, George Biddell Airy published his renowned article *Tides and Waves* in the *Encyclopaedia Metropolitana*. At the time of its publication, Airy had already achieved recognition both as a mathematician and an astronomer. This article has since been acknowledged as one of the foundational contributions to the mathematical theory of water waves.

1.2 Relevent Equations and Conditions

In this section, we present a set of fundamental equations and definitions relevant to the study of water waves. These are essential for developing a basic understanding of water wave theory. In particular, we adopt the framework of *linearized water wave theory*, which enables us to describe different boundary conditions under simplified assumptions. The motion is assumed to be irrotational, and the fluid is considered incompressible, homogeneous, and non-viscous. Furthermore, the sea-bed is usually taken to be flat and impermeable.

The principal parameters that govern wave motion are the water depth, wave height, and wavelength. Other important quantities such as wave-induced particle velocities and accelerations can be derived once these parameters are specified. Figure 1.1 illustrates a right-handed Cartesian coordinate system, where the xy-plane corresponds to the mean undisturbed free surface of the ocean, and the z-axis denotes the upward vertical direction. A *crest* is defined as the location on a wave where the surface elevation reaches its maximum, while a *trough* is the point of minimum displacement in the wave cycle. The horizontal distance between two successive crests (or troughs) is referred to as the *wavelength* λ. The commonly used notations in water wave mechanics are summarized below:

- H: water depth, measured from the mean water level to the sea-bed,
- $\eta(x, y, t)$: vertical displacement of the free surface above the mean water level,
- A_0: wave amplitude,
- T: wave period,
- $k = \frac{2\pi}{\lambda}$: wavenumber,
- $\omega = \frac{2\pi}{T}$: angular frequency.

In reality, ocean waves are typically irregular and random, formed by the superposition of multiple regular wave components with varying frequencies and amplitudes. A *regular wave* (or component wave) is characterized by a single frequency (or wavelength) and a definite amplitude. Examples include *wind waves* and *swells.* By contrast, *irregular waves* include *surf, beats, harbour resonance, seiches*, and *tsunamis.* Depending on the relative depth, defined as H/λ, waves are classified into three categories:

- For $H/\lambda < 1/20$, the depth is considered small relative to the wavelength. The resulting waves are termed *shallow-water waves* or *long waves* (e.g., tides, tsunamis).
- For $H/\lambda > 1/2$, the waves are classified as *deep-water waves* or *short waves*, with *rogue waves* being a notable example.
- For $1/20 < H/\lambda < 1/2$, waves are known as *intermediate-depth waves.*

When the wave amplitude is assumed to be small compared with the wavelength, the governing framework is called the *linearized theory of water waves.* Although natural ocean waves are nonlinear, in most engineering applications, the error incurred by applying linear theory is relatively small. Hence, the linear small-amplitude theory is widely adopted for modeling wave problems. In this thesis, all problems are formulated within this framework.

For an inviscid and incompressible fluid with velocity $\vec{U}$, the governing conservation laws are

$$\nabla \cdot \vec{U} = 0, \tag{1.1}$$

$$\frac{\partial \vec{U}}{\partial t} + (\vec{U} \cdot \nabla)\vec{U} = \vec{g} - \frac{1}{\rho}\nabla P, \tag{1.2}$$

where ρ denotes the fluid density, $\vec{g}$ the gravitational acceleration, and P the hydrodynamic pressure. Assuming the flow to be irrotational, a scalar potential function Φ exists such that

$$\vec{U} = -\nabla\Phi. \tag{1.3}$$

Although both signs are mathematically valid, the negative sign is adopted to be consistent with the convention that gravity waves propagate from higher to lower potential, thereby representing an energy loss. Substituting Eq. (1.3) in Eq. (1.1) yields the continuity equation for potential flow as

$$\nabla^2\Phi = 0, \tag{1.4}$$

which is known as the **Laplace's equation**. For time-harmonic motions, the velocity potential in Cartesian coordinates (x, y, z) may be expressed as

$$\Phi(x, y, z, t) = \mathrm{Re}\Big[\phi(x, y, z)e^{-\mathrm{i}\omega t}\Big], \tag{1.5}$$

where $\phi(x, y, z)$ is the complex spatial potential function, and "Re" denotes the real part. Considering gravity acting in the negative z-direction, one can write

$$\vec{g} = \nabla(-gz). \tag{1.6}$$

Substituting it in Eq. (1.2) gives

$$\nabla\left[-\frac{\partial\Phi}{\partial t} + \frac{1}{2}\nabla\Phi\cdot\nabla\Phi + \frac{P}{\rho} + gz\right] = 0. \tag{1.7}$$

After integration, this reduces to

$$-\frac{\partial\Phi}{\partial t} + \tfrac{1}{2}\nabla\Phi\cdot\nabla\Phi + \frac{P}{\rho} + gz = 0, \tag{1.8}$$

which represents the **Bernoulli's equation** (dynamic boundary condition). The free surface kinematic condition at $z = \eta(x, y, t)$ is given by

$$-\frac{\partial\Phi}{\partial z} = \frac{\partial\eta}{\partial t} + \frac{\partial\eta}{\partial x}\frac{\partial\Phi}{\partial x} + \frac{\partial\eta}{\partial y}\frac{\partial\Phi}{\partial y}. \tag{1.9}$$

Neglecting nonlinear terms yields the linearized form

$$-\frac{\partial\Phi}{\partial z} = \frac{\partial\eta}{\partial t} \quad \text{at} \quad z = 0. \tag{1.10}$$

Similarly, linearizing Eq. (1.8) at $z = \eta$ gives

$$-\frac{\partial\Phi}{\partial t} + \frac{P}{\rho} + g\eta = 0. \tag{1.11}$$

Within the linearized theory, using Eq. (1.5), the governing boundary value problem is expressed as

$$\nabla^2\phi = 0, \tag{1.12}$$

subject to appropriate boundary conditions. Assuming zero hydrodynamic pressure at the free surface, combining Eq. (1.10) and Eq. (1.11) leads to the free surface condition at $z = 0$:

$$\frac{\partial \phi}{\partial z} - K\phi = 0, \tag{1.13}$$

where $K = \omega^2/g$. It should be noted that while the form of waves may vary, in the small-amplitude limit, they all satisfy Eq. (1.12) or related variants.

The ocean bottom can exhibit a variety of characteristics depending on the geological and sedimentary conditions. It may be rigid flat, porous, undulating, or elastic in nature, among other possibilities. To account for such variations, an appropriate bottom boundary condition must be applied. Therefore, the bottom condition can be

$$\frac{\partial \phi}{\partial \mathbf{n}} = 0 \quad \text{at} \quad z = -H(x, y), \tag{1.14}$$

where $\mathbf{n}$ denotes the outward normal to $H(x, y)$. However, this condition (1.14) is not valid when the sea-bed is not impermeable.

1.3 Sea Ice

Ice manifests in various forms across the natural environment, including snow, hail, glaciers, and frozen layers covering lakes, rivers, and oceans. Although these types of ice exhibit distinct macroscopic characteristics depending on their mode of formation and environmental conditions, they all share a common microscopic identity. The underlying crystal structure of ice remains fundamentally the same in each case, illustrating the consistency of its molecular arrangement despite the diversity of its external appearances.

During freezing conditions, if the ocean surface is disturbed by wind and wave activity, the initial stages of ice formation give rise to a viscous, semi-consolidated layer known as *grease ice*. As freezing progresses, this layer develops into a discontinuous cover composed of circular or irregular fragments referred to as *pancake ice*. Conversely, under relatively calm atmospheric and oceanic conditions, a more uniform and continuous ice sheet may form. Nevertheless, the integrity of this sheet is often disrupted by the formation of *leads*, which are linear or irregular openings of open water that emerge within the sea ice due to thermal contraction, mechanical stress, or differential motion in the ice field. These leads are significant not only as zones of ice deformation, but also as critical pathways for heat exchange, gas transfer, and brine drainage between the ocean and atmosphere, thereby influencing the thermodynamic and dynamic behavior of the polar sea ice system.

When sea ice is subjected to compressive or shear stresses induced by wind forcing or ocean currents, the ice cover undergoes significant mechanical deformation. In regions where the ice is relatively thin, one floe may override another, forcing the lower sheet downward in a process termed rafting. Such failures are often initiated at structurally weaker zones, notably at refrozen leads, where the mechanical strength is reduced compared to the surrounding consolidated ice. In contrast, where the ice is thicker, deformation commonly occurs through buckling, resulting in fracture into discrete blocks that accumulate to form pressure ridges. These ridges are blocky aggregations characterized by low mechanical integrity. The portion of a ridge protruding above the water surface is referred to as the sail, while the submerged extension, known as the keel, can reach depths several times greater than the sail height.

A significant portion of the sea ice in polar oceans exists only seasonally, persisting through the winter and spring months before breaking up, dispersing, and melting with the arrival of summer. During the short polar summer, large areas of the Arctic and Antarctic seas become largely ice-free. With the onset of autumn, declining air temperatures initiate the cooling of the ocean surface. One of the earliest observable indicators of ice formation is the attenuation of capillary waves, caused by the development of a thin, flexible, and nearly transparent ice skim on the water surface.

Once this initial ice skim forms, further ice growth proceeds primarily through the removal of latent heat by vertical conduction across the ice layer. As the ice thickens, the growth rate decreases, since the ice sheet functions as an insulating barrier between the ocean and the cold atmosphere. Beneath the transitional layer lies the columnar zone in which ice crystals elongate in the direction of heat flow. In some cases, a single crystal grain may extend through nearly the entire thickness of the ice sheet, reflecting the anisotropic nature of heat transfer during freezing.

While much of this description applies specifically to sea ice, similar processes also occur in the formation of lake and river ice. For instance, the relationship between water disturbance during freezing and the resulting size and orientation of ice crystals holds regardless of salinity. However, the presence or absence of impurities can have a pronounced influence on ice microstructure. Freshwater ice, such as that formed on lakes and rivers, typically develops a smooth, glass-like, planar icewater interface. This contrasts with sea ice, where the salt content leads to a more complex microstructure characterized by cellular features at the freezing interface. These structural differences are significant, as they influence not only the mechanical properties of the ice, but also its thermal conductivity, permeability, and overall role in polar and freshwater systems.

1.3.1 The Floating Ice Plate

The conventional mathematical framework employed to analyze the dynamic response of a floating ice sheet subjected to a moving load is founded on the thin plate theory, a concept extensively used in structural mechanics. In this approach, the ice sheet is idealized as a thin elastic plate resting on a fluid foundation, with the underlying water

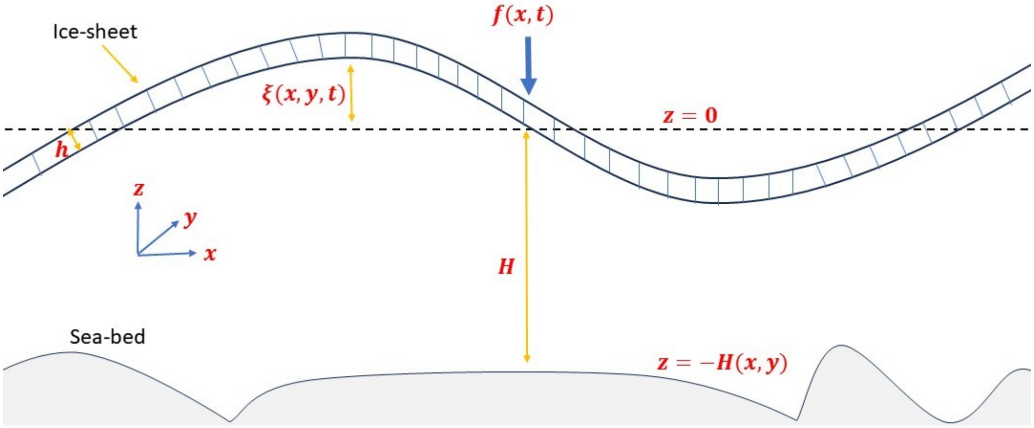

Figure 1.2: Schematic diagram of a floating ice sheet over a sea-bed

treated as an inviscid, incompressible fluid undergoing irrotational flow described by a velocity potential. The thin plate approximation assumes that the ice thickness is small relative to its horizontal dimensions, allowing simplification of the governing equations by neglecting transverse shear deformation and normal stress variations through the thickness of the plate. This assumption enables the use of classical plate bending theory to describe the elastic behavior of the ice under load.

The system is impacted by two main restoring forces in this model. The first arises from the bending stiffness of the plate itself, which resists deformation and tends to restore the plate to its undeformed state. The second originates from gravitational forces, which act to level the water surface, opposing any displacement caused by the load. These restoring mechanisms interact to define the overall dynamical behavior of the ice sheet.

The mechanical coupling between the floating ice plate and the underlying water is described through a Bernoulli-type pressure equation applied at the ice-water interface, along with the implicit non-cavitation condition which ensures that the ice always remains in contact with the water.

Elastic Model

Consider an infinite, homogeneous ice sheet of thickness h and density ρ_i, floating on water of density ρ. The underlying water has depth $z = -H$, with the undisturbed ice-water interface located at $z = 0$. The water is bounded below by the sea-bed, which may possess varying characteristics depending on geological and environmental conditions; for example, it can be rigid, elastic, porous, or layered with different mechanical properties. The elastic plate equation for an inviscid, incompressible fluid foundation describes the dynamics of the ice sheet and the underlying fluid. This equation accounts for both the bending stiffness of the ice and the hydrodynamic pressure exerted by the fluid, which itself depends on the properties of the underlying sea-bed. The schematic diagram shown in Figure 1.2 illustrates a floating ice sheet in a finite depth ocean. The structure of sea ice is inherently complex, and its physical properties vary significantly with the characteristics of the underlying sea-bed. Let $\xi(x, y, t)$ represent the small vertical displacement of the ice sheet. Mathematically, the governing equation takes the general form

$$D\nabla^4\xi + N\nabla^2\xi + \rho_i h\xi_{tt} = p - f(x, y, t) \quad \text{at} \quad z = 0, \tag{1.15}$$

where ∇^4 is the biharmonic operator, $f(x, y, t)$ represents the external force applied to the ice plate because of the moving load and the water pressure component p at the interface due to the buoyancy of the fluid foundation. $D = \frac{Eh^3}{12(1-\nu^2)}$ denotes the effective flexural rigidity of the plate with Young's modulus E and Poisson's ratio ν. The term $N\nabla^2\xi$ denotes the stress term where N is an in-plane force (compressive stress for $N > 0$ and tensile stress for $N < 0$).

The linearized Bernoulli's equation for an incompressible irrotational flow defines the water pressure at $z = 0$ as

$$p = -\rho g\xi - \rho\Phi_t, \tag{1.16}$$

where the hydrostatic contribution is represented by the first term and the fluid inertia effect by the second term on the right-hand side. Therefore, Eq. (1.15) becomes

$$D\nabla^4\xi + N\nabla^2\xi + \rho_i h\xi_{tt} = -\rho g\xi - \rho\Phi_t - f(x, y, t), \tag{1.17}$$

representing the dynamic loading condition for a thin elastic plate subjected to in-plane forces. If the in-plane force is negligible ($N = 0$), the above equation simplifies to

$$D\nabla^4\xi + \rho_i h\xi_{tt} = -\rho g\xi - \rho\Phi_t - f(x, y, t), \tag{1.18}$$

which describes the dynamic loading condition of a thin elastic plate without in-plane stress effects.

The mathematical formulation of the problem involves solving the three-dimensional Laplace's equation, which must be solved subject to the physically relevant bottom boundary condition, the kinematic condition at the icewater interface, and the dynamic boundary condition given by Eqs. (1.17) or (1.18). The objective is to determine $\xi(x, y, t)$ for a prescribed, time-dependent loading function $f(x, y, t)$.

1.4 Mathematical Tools

Since our works in the thesis are solved mainly through the application of Laplace and Fourier transforms, some basic definitions and results are presented here.

1.4.1 Fourier Transform

The Fourier transform of a function $\mathscr{R}(x,t)$ with respect to x is defined by

$$\mathscr{F}\{\mathscr{R}(x,t)\} = \hat{\mathscr{R}}(k,t) = \frac{1}{\sqrt{2\pi}} \int_{-\infty}^{\infty} \mathscr{R}(x,t) e^{-\mathrm{i}kx}\, dx. \tag{1.19}$$

The inverse Fourier transform is defined by

$$\mathscr{F}^{-1}\{\hat{\mathscr{R}}(k,t)\} = \mathscr{R}(x,t) = \frac{1}{\sqrt{2\pi}} \int_{-\infty}^{\infty} \hat{\mathscr{R}}(k,t) e^{\mathrm{i}kx}\, dk. \tag{1.20}$$

1.4.2 Laplace-Fourier Transform

Let $\bar{\mathscr{R}}(x,s)$ be the Laplace transform of the function $\mathscr{R}(x,t)$ in time t, defined by

$$\mathscr{L}\{\mathscr{R}(x,t)\} = \bar{\mathscr{R}}(x,s) = \int_{0}^{\infty} \mathscr{R}(x,t) e^{-st}\, dt, \tag{1.21}$$

and let $\hat{\bar{\mathscr{R}}}(k,s)$ be the Fourier transform of $\bar{\mathscr{R}}(x,s)$ with respect to x, defined by

$$\mathscr{F}\{\bar{\mathscr{R}}(x,s)\} = \hat{\bar{\mathscr{R}}}(k,s) = \int_{-\infty}^{\infty} \bar{\mathscr{R}}(x,s) e^{-\mathrm{i}kx}\, dx, \tag{1.22}$$

where s and k are the transformed variables corresponding to the Laplace and Fourier transforms, respectively.

1.4.3 Some Theorems and Results

The Riemann-Lebesgue Lemma: The Riemann-Lebesgue lemma states that, for a function $f(x)$ for which the integral $\int_a^b |f(x)|\, dx < \infty$, where a and b are real numbers, we have $\int_a^b f(x) e^{\mathrm{i}xt}\, dx = 0$ as $t \to \infty$. □

Residue Theorem: If $f(z)$ is analytic inside and on a simple closed positively-oriented contour $\boldsymbol{C}$, except for finitely many isolated singularities inside $\boldsymbol{C}$, then

$$\oint_{\boldsymbol{C}} f(z)\, dz = 2\pi i \sum \mathrm{Res}(f, z_k),$$

where the sum is taken over the residues at the singularities z_k inside $\boldsymbol{C}$. Res denotes the residue. □

Method of Stationary Phase: For finding the asymptotic behaviour of an oscillatory integral for large time around a stationary point, we use the following result:
Result 1:- Let the integral given in the form

$$I(t) = \int_a^b \mathcal{F}(k) e^{\mathrm{i}\Psi(k)t} dk, \tag{1.23}$$

with $\mathcal{F}(k)$, $\Psi(k)$, a, b, t all real, be called a *generalized Fourier integral.* For asymptotic expansion of the integral as $t \to +\infty$, we use the method of stationary phase.

Let s_0 be a stationary point, and if $\mathcal{F}(s_0) \neq 0$, then the integral gives

$$I(t) \sim \mathcal{F}(s_0) \left(\frac{n!}{t|\Psi^{(n)}(s_0)|} \right)^{1/n} \left(\frac{\Gamma 1/n}{n} \right) \exp\left(\mathrm{i}t\Psi(s_0) \pm \mathrm{i}\frac{\pi}{2n} \right), \tag{1.24}$$

where $\Psi^{(n)}(s_0) \neq 0$ but $\Psi^{(1)}(s_0) = \Psi^{(2)}(s_0) = \cdots = \Psi^{(n-1)}(s_0) = 0$. Furthermore, we use the factor $\exp(+\mathrm{i}\frac{\pi}{2n})$ if $\Psi^{(n)}(s_0) > 0$ and the factor $\exp\left(-\mathrm{i}\frac{\pi}{2n}\right)$ if $\Psi^{(n)}(s_0) < 0$ (Bender and Orszag (2013)). ☐

1.5 Existing Literature and Background

The analysis of floating ice sheets subjected to moving loads has significant importance in many engineering and scientific applications, especially in cold regions. Floating ice sheets form natural platforms for transportation, research, and logistics. In countries such as Canada, ice roads provide crucial winter routes for commercial vehicles, enabling access to remote areas during harsh weather conditions. Similarly, aircraft operations in Antarctica, particularly at McMurdo Sound, rely on ice runways to transport supplies and personnel efficiently (Hosking and Milinazzo (2022)). Understanding the mechanical response of ice sheets under moving loads is thus essential for ensuring the safety and reliability of these operations.

1.5.1 Studies on Moving Loads over Floating Ice Sheets

The fundamental theoretical framework for analyzing moving loads on ice plates was established by Squire et al. (1996) in the monograph *Moving Load on Ice Plates*, which compiles theoretical and experimental research conducted up to 1996. Early investigations, such as those by Greenhill (1886), developed the basic dispersion relation for a homogeneous elastic ice plate floating on water. A subsequent work by Wilson (1958) demonstrated that, when the load speed is below the minimum phase speed of the waves, the ice response resembles that of a static load. Kheisin (1971) later analyzed the time-dependent response of an ice sheet subjected to a steadily moving line load, which provided a basis for several subsequent studies. Takizawa (1985) confirmed through field experiments that significant wave generation occurs as the load speed approaches the minimum phase speed. Davys et al. (1985) further analyzed the formation of flexural-gravity waves induced by a continuously moving load, while Schulkes et al. (1987) examined the effects of lateral stresses on the ice plate, revealing modifications in the dispersion relation with limited practical implications. Extending this analysis, Schulkes and Sneyd (1988) applied asymptotic methods to the problem of an impulsively starting load, showing that the deflection of the ice sheet grows with time when the load moves with critical speeds.

Hosking et al. (1988) introduced viscoelastic effects into the analysis, showing how ice rheology influences wave propagation and damping. Milinazzo et al. (1995) and Wang et al. (2004) analyzed the steady and transient responses of floating ice sheets subjected to moving loads of various geometries. Miles and Sneyd (2003) employed an integral-transform approach to study the linearized response of an accelerating line load, laying the groundwork for later refinements. Extending this, Hosking and Milinazzo (2022) examined variable-speed line loads and demonstrated how acceleration influenced solitary wave evolution, consistent with earlier findings by Guyenne and Părău (2014).

Recent advancements have incorporated nonlinear effects, which become critical near resonance speeds (Marchenko (2016), Părău and Dias (2002), Dinvay et al. (2022)). These nonlinear models capture phenomena such as amplitude growth and solitary wave generation that are not described by linearized theories. Sturova (2021) investigated the influence of non-uniform compression within the ice sheet on wave disturbance, while Malenko and Yaroshenko (2024) explored responses under periodically varying loads, showing that compression and tension forces alter critical velocities and wave propagation zones.

Further studies have extended the classical models to account for variable environmental and material conditions. Pogorelova et al. (2016) examined the effect of spatially varying ice thickness on deflection behavior, while Khabakhpasheva et al. (2019) investigated the long-term response of ice-covered channels, identifying both steady and standing wave components dependent on critical load speeds. Using numerical techniques such as the boundary integral method, Xue et al. (2021) studied the hydroelastic response of both continuous and cracked ice sheets under moving pressures. Recent works by Tkacheva (2022) and Tkacheva (2023) extended these analyses to include the effects of shear currents, compression, and load direction, whereas Shishmarev et al. (2023) and Wang et al. (2023) analyzed viscoelastic and nonlinear potential flow models to evaluate steady-state hydroelastic waves. In a more recent development, Boral and Ni (2025) utilized the Kelvin-Voigt viscoelastic framework to describe flexural-gravity waves induced by periodic moving loads, identifying the role of plate viscosity and compressive forces in wave blockage conditions.

Most early analyses assumed a rigid sea-bed beneath the floating ice. However, later studies recognized that the porosity of the sea-bed can significantly influence the fluid-structure interaction and the resulting wave dynamics. The interaction of water waves with porous sea-beds has been studied within the framework of linearized water wave theory by several authors. Silva et al. (2002) analyzed linear wave propagation over finite porous sea-beds with rapidly varying permeability, while Zhu (2001) and Martha and Bora (2007) studied the scattering and diffraction of waves over permeable bottoms.

Building upon this foundation, Kundu and Chakraborty (2021) examined gravity wave generation on an ice-covered ocean with a porous bottom using Laplace and Hankel transforms. Hossain et al. (2022) considered moving oscillatory pressure disturbances in the presence of a porous sea-bed and demonstrated their effect on wave patterns. A porous viscoelastic model incorporating the mechanical response of the sea-bed was developed by Chen et al. (2019). In a two-layer fluid system, Hossain et al. (2023a) analyzed oscillatory surface pressure-induced waves over a porous sea-bed, while Hossain et al. (2023) explored how surface tension and bottom flexibility influenced the wave characteristics and critical velocities. These studies collectively highlight that sea-bed porosity can significantly modify wave amplitude, damping, and resonance conditions.

Considering a flat sea-bed is often unrealistic, especially in coastal and continental shelf regions where bed undulations are common. Davies (1982b) and Davies and Heathershaw (1984) first identified the occurrence of Bragg resonance for the situation of the wavelength of incident waves being approximately twice the sea-bed undulation wavelength. Extending this concept, Davies et al. (1989) analyzed both resonant and non-resonant interactions for sinusoidal sea-bed ripples. The development of sand ripple formations was explained through linear stability analysis by Blondeaux (1990), and Dalrymple and Kirby (1986), who used the Boundary Integral Equation Method (BIEM) to study waveripple interactions.

Subsequent numerical studies, including those by Liu and Yue (1998) and Wu et al. (2006), generalized Bragg scattering mechanisms using perturbation and pseudo-spectral methods. Martha and Bora (2007) further examined oblique wave diffraction over small bottom undulations, while Huang et al. (2011) used the Navier-Stokes framework to simulate flow over permeable rippled sea-beds. In a two-layer fluid, Panda and Martha (2013) studied wave scattering over porous sea-bed undulations with an overlying elastic ice cover, and Binder et al. (2015) utilized the Korteweg-de Vries framework to evaluate the steady free-surface flow over periodic bed topographies. These results underscore the crucial role of bottom irregularities in modifying surface and flexural-gravity wave behavior.

The interaction between surface waves and elastic sea-beds has also received considerable attention. Mohapatra and Sahoo (2011) presented a hydroelastic model incorporating small-amplitude wave theory and plate deflection to study wave spectra over an elastic bed. Saha and Bora (2015) analyzed trapped wave modes around submerged cylinders above elastic bottoms, while Barman and Bora (2021) investigated flexural-gravity wave motion over elastic foundations through dispersion relations. In the presence of mild sea-bed undulations, Chanda and Bora (2021) demonstrated that bed elasticity could strongly alter the wave dynamics.

More recently, Saha et al. (2022) studied trapping resonance in the presence of ocean currents and ice compression, while Barman et al. (2024a) and Barman et al. (2024b) explored the combined effects of membrane-covered surfaces, uneven sea-beds, and currents. Jain and Bora (2024) analyzed oblique water wave scattering by porous barriers near rigid floating structures, and Aggarwal et al. (2024) proposed asymptotic techniques for flexural-gravity wave scattering through variable-thickness ice sheets with uniform currents. These developments emphasize the complex coupling between hydrodynamic forces, sea-bed properties, and ice elasticity in realistic marine environments.

1.6 Motivation and Scope of the Present Work

The mechanical and hydrodynamic behavior of floating ice sheets is strongly influenced by the physical characteristics of the sea-bed beneath them. In natural marine environments, the sea-bed rarely remains uniform or rigid; instead, it often exhibits variations in composition, permeability, and elasticity depending on geological and sedimentary processes. The sea-bed may consist of layers of sand, silt, clay, or gravel, each possessing distinct porosity and permeability properties. Such heterogeneous sea-beds play a crucial role in modulating the propagation and attenuation of water waves. When a moving load, such as a vehicle or aircraft, traverses the surface of a floating ice sheet, the induced hydrodynamic pressure propagates through the water column and interacts with the sea-bed. This interaction, in turn, affects the reflected and transmitted wave fields, thereby altering the dynamic response of the ice cover.

In regions such as the Arctic, Antarctic, and sub-Arctic coastal zones, these interactions become especially significant. Here, ice sheets frequently overlay shallow seas where the sea-bed is composed of porous sediments or flexible deposits. The porosity of the sea-bed allows partial transmission and dissipation of wave energy, which influences both the amplitude and phase of flexural-gravity waves. Hence, understanding the impact of sea-bed permeability on wave generation and propagation beneath a moving load is fundamental for accurately predicting ice sheet deflection and stress distribution. The response becomes even more complex when additional factors such as in-plane stress, variable ice thickness, or underlying ocean currents are considered. Each of these parameters can modify the dispersion characteristics of the system and lead to changes in the critical speeds at which resonance or instability occurs.

Furthermore, natural ocean currents are omnipresent in most polar regions due to tidal motions, density-driven circulation, and wind forcing. The presence of such a uniform current beneath an ice sheet alters the energy transfer between the moving load and the underlying fluid. It can modify the direction of wave propagation, influence the critical velocity thresholds, and affect the asymmetry in deflection patterns. The combined effect of current-induced shear, sea-bed porosity, and ice stress introduces complex coupled dynamics that cannot be captured by simplified rigid-bed or quiescent-water models.

From an applied perspective, these interactions are of vital importance in designing and operating infrastructure in polar environments. Ice roads and runways used for heavy transportation and logistics, offshore oil platforms supported by ice, and pipelines buried beneath shallow Arctic shelves all rely on an accurate understanding of ice-water-seabed coupling. Failure to account for these combined effects may result in underestimation of stresses and deflections in the ice sheet, potentially leading to structural instability or safety hazards. Therefore, the development of a comprehensive hydroelastic model that simultaneously considers sea-bed porosity, internal ice stress, and the influence of a uniform current under a moving load becomes essential.

The present study aims to address this need by formulating and analyzing a theoretical model for wave generation in a floating ice sheet in an ocean, subjected to a moving line load in the presence/absence of a uniform current with different types of sea-bed. By integrating the effects of sea-bed, internal stress, and current, the study seeks to elucidate their combined influence on the wave field, critical speeds, and long-term stability of the ice sheet. The findings of these investigation are expected to contribute to a deeper understanding of coupled hydroelastic-seabed interactions and provide insights applicable to the design and management of ice-related operations in polar marine environments.

1.7 Outline of the Thesis

This thesis is organized in seven chapters, with five chapters addressing distinct aspects of the overall research theme. The current chapter introduces the fundamental concepts and governing equations associated with the linearized theory of water waves and floating ice sheets. It also presents a comprehensive review of the existing literature and outlines the motivation behind the present investigation. Chapters 2 to 6 are devoted to the detailed formulation and analysis of five specific problems that collectively encompass the influence of various physical effects such as sea-bed properties, in-plane stress, and uniform currents on the hydroelastic behavior of floating ice sheets under moving loads. Each of these chapters develops the corresponding mathematical models, derives analytical or numerical solutions, and discusses the physical interpretations of the results. Finally, Chapter 7 summarizes the key findings of this study, highlights the major contributions, and suggests potential directions for future research aimed at advancing the theoretical and applied understanding of hydroelastic wave phenomena in ice-covered waters.

Chapter 2 investigates the hydroelastic response of a floating ice sheet subjected to a moving load over a porous sea-bed. The study primarily focuses on the physical effects of the sea-bed porosity and in-plane stress within the ice sheet on the generation and propagation of flexural-gravity waves. The porous nature of the sea-bed introduces additional damping and energy dissipation into the system, altering the amplitude and wavelength of the resulting waves. Simultaneously, the internal stress within the ice modifies the stiffness characteristics of the plate, thereby influencing the overall deflection pattern and wave speed. Overall, the results highlight that both the porous sea-bed and stress within the ice sheet have substantial impacts on the formation and evolution of flexural-gravity waves under moving loads.

Chapter 3 investigates the generation and propagation of waves in a floating ice sheet induced by a moving line load in the presence of an undulating sea-bed. The study considers a two-dimensional configuration and emphasizes the physical influence of sea-bed irregularities on the ice-water interaction. The undulating bottom, modeled as a sinusoidal ripple bed, introduces periodic variations that affect the deflection pattern of the ice sheet and give rise to resonance phenomenon. As the number of sea-bed ripples increases, the response of the ice sheet tends to approach that corresponding to a flat sea-bed, indicating a diminishing influence of bottom undulations. The occurrence of Bragg resonance is also captured, highlighting the strong coupling between the sea-bed topography and surface wave fields. Overall, the findings provide meaningful insights into how sea-bed geometry modifies the dynamic response of ice-covered waters under moving loads.

Chapter 4 explores the wave response of a floating ice sheet subjected to a moving load in the presence of a uniform current and a flexible sea-bed of finite depth. The sea-bed is modeled as an elastic plate to account for its deformability. The study focuses on how the combined effects of bottom elasticity and uniform current influence the propagation characteristics and deflection patterns of the ice sheet. Results show that the presence of a flexible sea-bed significantly alters the dispersion behavior, affecting both phase and group speeds of flexural-gravity waves. The uniform current further modifies wave symmetry and energy distribution, leading to directional variations in the ice response. This study highlights the critical roles of current and sea-bed elasticity in governing the complex hydroelastic interactions that occur in ice-covered waters.

Chapter 5 focuses on the dynamic response of a floating ice sheet subjected to a time-dependent moving load in the presence of a uniform underlying current. The moving load is distributed over a finite region of the ice surface and varies with time, representing a realistic model of vehicle or aircraft motion across ice-covered waters. The study investigates how the combined effects of load motion, frequency variation, and background current influence the wave pattern and deflection characteristics of the ice sheet. It is observed that, when the load moves at a constant speed, distinct singularities appear in the governing integral expressions, which dominate the deflection behavior. In contrast, these singularities disappear when the load undergoes uniform acceleration or deceleration, leading to smoother wave responses. Results reveal that both the speed variation of the load and the current significantly alter the amplitude and propagation of flexural-gravity waves.

Chapter 6 examines the dynamic response of a floating ice sheet subjected to a moving load over a rectangular trench-shaped sea-bed. The study shows that the ice sheet behavior is affected by the trench depth: an increase in the trench depth leads to a reduction in ice deflection, indicating that deeper trenches mitigate ice deformation. At very low load speeds, the deflection profile closely resembles that produced by a stationary load. As the load speed increases, wave generation becomes more pronounced, and the dynamic wave response of the ice sheet becomes the dominant feature of the system.

An appendix (named Appendix A) can be found at the end of the thesis. It provides a detailed explanation of the zeros and stationary points encountered in the works.

CHAPTER 2

Response of a floating ice sheet due to a moving load in the presence of a porous sea-bed

2.1 Mathematical Formulation

We consider the propagation of linear water waves over a porous sea-bed with the z-axis pointing vertically upwards, while the plane $z = 0$ is aligned with the ice-free surface of the water, and $z = -H$ represents the sea-bed. It may be noted that the porous sea-bed is considered only as a boundary of the fluid motion and the wave propagation beneath the depth $z = -H$ is not taken into account. This kind of assumption still gives rise to the observation of the effect of the porous sea-bed as observed from some earlier studies (e.g., Martha and Bora (2007), Maiti and Mandal (2014)). We assume a laterally infinite ice sheet, possessing density ρ_i and small thickness h having homogeneous property, floating on water which has density ρ. From here on, we shall refer to the thin ice sheet as a thin plate as it is expected that it adheres to the thin plate theory.

Figure 2.1 represents the schematic diagram of the problem in the framework of a sea ice sheet over a porous sea-bed. The structure of ice, particularly sea ice, is known to be complicated, and its physical attributes have considerable variation with the sea-bed property.

Including the stress term $N\nabla^2\xi$, the equation of motion is given by

$$D\nabla^4\xi + N\nabla^2\xi + \rho_i h\xi_{tt} = -\rho g\xi - \rho\Phi_t - f(x, y, t). \tag{2.1}$$

Considering periodic waves with time harmonic motions, $\Phi(x, y, z, t)$, the velocity potential, and $\xi(x, y, t)$, the ice sheet deflection, can be expressed as

$$\Phi(x, y, z, t) = \mathrm{Re}\{\phi(x, y, z)e^{-\mathrm{i}\omega t}\}, \;\; \xi(x, y, t) = \mathrm{Re}\{\xi(x, y)e^{-\mathrm{i}\omega t}\}.$$

The velocity potential Φ satisfies the Laplace's equation, kinematic and sea-bed conditions

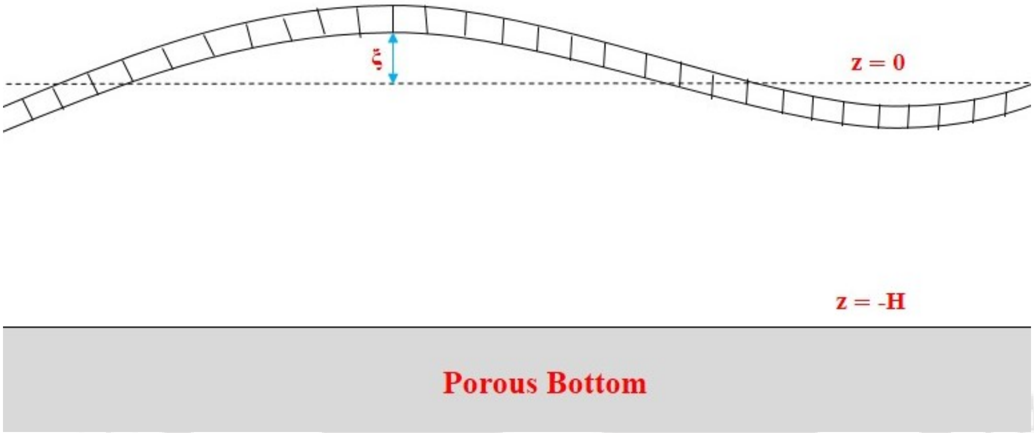

Figure 2.1: Sketch of the floating ice plate over a porous sea-bed

as follows:

$$\Phi_{xx} + \Phi_{yy} + \Phi_{zz} = 0, \tag{2.2}$$

$$\Phi_z = \xi_t \;\text{ at }\; z = 0, \tag{2.3}$$

$$\Phi_z + G\Phi = 0 \;\text{ at }\; z = -H, \tag{2.4}$$

where G is the porous-effect parameter of the sea-bed. The standard expression for the parameter G is $G = \dfrac{\gamma}{kbR} = G_r + \mathrm{i}G_i$, in which G_r and G_i are real, and $R = K - \mathrm{i}\left[1 + M_0\left(\dfrac{1-\gamma}{\gamma}\right)\right]$ is the dimensionless porous impedance parameter, with γ, K and M_0 representing the porosity, the linearized resistance coefficient and the added-mass coefficient of the porous medium, respectively (Yu (1995)). It is to be noted that the porous-effect parameter is generally complex since it typically includes both the resistance effects (the real part) and the inertial effect (the imaginary part) (Chanda and Bora (2020)). As per the approach of Maiti and Mandal (2014) and Martha and Bora (2007), the porous-effect parameter G of the sea-bed is considered as real in this work. This assumption ensures that the progressive wave propagates appropriately in the far field by excluding the inertial effects and concentrating only on the resistance effects. Further, from Eqs. (2.2) to (2.4), we can find

$$\Phi = \frac{\boldsymbol{\chi}}{k}\xi_t \;\text{ at }\; z = 0,$$

where $\boldsymbol{\chi} = \dfrac{k - G\tanh(kH)}{k\tanh(kH) - G}$ and $k = \sqrt{k_1^2 + k_2^2}$, with k_1 and k_2 representing the components of k along the x and y directions, respectively. We use $\boldsymbol{\chi}$ as a notation only for our convenience. Therefore, we rewrite Eq. (2.1) as

$$D\nabla^4\xi + N\nabla^2\xi + \rho_i h\xi_{tt} = -\rho g\xi - \frac{\rho\boldsymbol{\chi}}{k}\xi_{tt} - f(x, y, t). \tag{2.5}$$

Substitution of the sinusoidal wave $\xi = A_0 e^{\mathrm{i}(\mathbf{k}.\mathbf{x} - \omega t)}$, where $\mathbf{k} = k_1\hat{i} + k_2\hat{j}$, $\mathbf{x} = x\hat{i} + y\hat{j}$, into the homogeneous version of Eq. (2.5) gives the following dispersion relation:

$$\omega^2 = \left(\frac{Dk^4 - Nk^2}{\rho} + g\right)\left(\frac{k}{kh' + \boldsymbol{\chi}}\right), \tag{2.6}$$

where $h' = \rho_i h/\rho$ is the modified ice thickness. The dispersion relation is associated with three length scale parameters: (i) a short scale is defined by h', (ii) a long scale refers to as water depth H, (iii) an intermediate scale is defined by the inverse wavenumber k_{min}^{-1} at which the phase speed $c = \omega/k$ reaches its minimum value c_{min}, which is affected by the characteristics of both ice elasticity and the force of gravity. In this scenario, the stress N and porous-effect parameter G are also important. We shall use the following physical parameters values as used for McMurdo Sound in Antarctica in Davys et al. (1985): $E = 5 \times 10^9$ Nm^{-2}, $h = 2.5$ m, $H = 350$ m, $\nu = 1/3$, and $\rho = 1000$ kg/m^3.

In the region of short wavelengths where $kh' \geq \mathcal{O}(1)$, the elastic-dominated waves precede the source, while at longer wavelengths, the gravity waves trail behind the source. However, the applied stress N has the potential to affect the significance of intermediate wavelengths.

If the wavelength is larger compared to the ice thickness, we can ignore the ice acceleration component kh' of Eq. (2.6). Therefore, Eq. (2.6) can be approximated by

$$\omega^2 = \frac{Dk^5 - Nk^3 + \rho gk}{\rho\boldsymbol{\chi}}. \tag{2.7}$$

Additionally, the phase speed c and group speed c_g can be expressed as $c = \omega/k$, and $c_g = d\omega/dk$. Therefore, the phase speed is given by

$$c^2 = \frac{(Dk^4 - Nk^2 + \rho g)}{k\rho\boldsymbol{\chi}}. \tag{2.8}$$

We concentrate on the wavelengths that are much larger than the thickness of the plate. Thus, we use the dispersion relation given by Eq. (2.7) instead of Eq. (2.6). We consider only those values of k for which $\boldsymbol{\chi} > 0$. For waves of intermediate length, such as for $k_{\text{min}}H \gg 1$, we have $\boldsymbol{\chi} \approx 1$. The phase speed is given by

$$c = \sqrt{\frac{Dk^3 - Nk}{\rho} + \frac{g}{k}}. \tag{2.9}$$

The minimum phase speed c_{min} involves identifying the wavenumber k_{min} where the phase speed c equals the group speed c_g, which is derived from the stationary point condition of $dc/dk = 0$. Therefore, the minimum phase speed is given by

$$c_{\text{min}} = 2e^{-\frac{\alpha}{4}} \left(\frac{Dg^3}{27\rho}\right)^{\frac{1}{8}} \left(\frac{1}{2}(3 - e^{2\alpha})\right)^{\frac{1}{2}}, \quad \alpha = \sinh\left(\frac{N}{\sqrt{12\rho g D}}\right). \tag{2.10}$$

Now, $c_{\text{min}} = 0$ at $N \approx 2\sqrt{\rho g D} = N_c$(say), which corresponds to $k_{\text{min}} = (\rho g/D)^{1/4}$. The group speed c_g for wavelengths of an intermediate range can be expressed as

$$c_g = \frac{1}{2\omega}\left[\frac{5D}{\rho}\left(k^2 - \frac{3N}{10D}\right)^2 + g - \frac{9N^2}{20\rho D}\right], \tag{2.11}$$

for $N < \frac{1}{3}\sqrt{20\rho g D} = N_{cg}$(say), c_g is positive definite (provided $\omega > 0$). In theory, $c_g \leq 0$ when $N_{cg} \leq N \leq N_c$. However, the predicted behavior of waves may deviate from standard patterns when stress values are significantly large. It is unlikely that observers can observe the unusual phenomenon of wave crests moving along in one direction while the wave group stands stable or navigates in the opposite direction (Schulkes et al. (1987)). However, the typical pattern is unlikely to remain valid if the stress values are unusually large. We consider the stress values $N < N_{cg}$ for the usual behavior of waves. Furthermore, we notice that the minimum phase and group speed are not affected by the porous-effect parameter G. Here, c_{min} and $c_{g\text{min}}$ are considered the same for the porous sea-bed as well as for the rigid sea-bed.

In the case of shallow water depth, the relation $\tanh(kH) \approx kH$ is used. Therefore, the dispersion relation for shallow water depth can be obtained as

$$\omega^2\rho(1 - GH) = (Dk^4 - Nk^2 + \rho g)(k^2H - G).$$

Therefore, the phase speed becomes

$$c = \sqrt{\frac{(Dk^4 - Nk^2 + \rho g)(k^2H - G)}{\rho k^2(1 - GH)}},$$

which vanishes if $k = \pm\sqrt{G/H}$. The group speed is given by

$$c_g = \frac{k}{\omega\rho(1 - GH)}\left\{(2Dk^2 - N)(k^2H - G) + H(Dk^4 - Nk^2 + \rho g)\right\}.$$

If $k = \pm\sqrt{G/H}$, then there is a situation of no wave propagation. Further, the phase speed becomes complex for $0 < k < \sqrt{G/H}$.

In the deep water depth case, $\tanh(kH) \approx 1$ is used. Therefore, $\chi \approx 1$. Hence, the phase speed is similar to Eq. (2.9). We discuss the behavior of the phase and group speeds with the variations in N and G in the Numerical Results Section.

2.2 Method of Solution

We find the solution of the ice deflection ξ for a moving load. In this problem, we consider a concentrated line load that is imposed at $t = 0$ and then moves along the x-axis in the positive direction with a constant speed V. Therefore, the loading function has the following form: $f(x,t) = F(x - Vt)u(t) = F_0\delta(x - Vt)u(t)$, where F_0, δ and $u(t)$ are the value of force exerted perpendicular to the ice surface of a load per unit area, Dirac delta function and Heaviside unit step function, respectively. We also assume that the ice response in the other direction (the y-direction) is negligible, i.e., the stress effect is neglected in the y-direction.

We concentrate on those waves that are much longer than the ice thickness, allowing us to use Eq. (2.7) instead of Eq. (2.6). In other words, the small plate acceleration term $\rho_i h$ in Eq. (2.5) may be ignored. In order to find the ice-plate deflection, we use the Fourier transform technique by taking Fourier transform of Eq. (2.5) with respect to x. Thus, we have

$$Dk^4\hat{\xi} - Nk^2\hat{\xi} + \rho g\hat{\xi} + \frac{\rho\boldsymbol{\chi}}{k}\hat{\xi}_{tt} = -\frac{F_0}{\sqrt{2\pi}}e^{-ikVt}, \tag{2.12}$$

where the Fourier transform of $\xi(x,t)$ is

$$\hat{\xi}(k,t) = \frac{1}{\sqrt{2\pi}}\int_{-\infty}^{\infty}\xi(x,t)e^{-ikx}dx.$$

The general solution of Eq. (2.12) is given by

$$\hat{\xi}(k,t) = Ae^{ikct} + Be^{-ikct} - \frac{F_0}{\sqrt{2\pi}}\frac{e^{-ikVt}}{(Dk^4 - Nk^2 + \rho g - \rho\boldsymbol{\chi}kV^2)}, \tag{2.13}$$

where A and B are arbitrary constants. These constants can be determined by the initial conditions given by

$$\hat{\xi} = 0, \quad \hat{\xi}_t = 0 \quad \text{at} \quad t = 0. \tag{2.14}$$

Therefore, we get

$$\hat{\xi} = \frac{F_0}{\sqrt{2\pi}}\frac{e^{-ikVt}}{2\rho c\boldsymbol{\chi}}\left(\frac{e^{-ik(c-V)t} - 1}{k(c-V)} + \frac{e^{ik(c+V)t} - 1}{k(c+V)}\right). \tag{2.15}$$

For finding the expression of ξ, we use the inverse Fourier transform to obtain

$$\xi(x,t) = \frac{1}{\sqrt{2\pi}}\int_{-\infty}^{\infty}\hat{\xi}(k,t)e^{ikx}dk. \tag{2.16}$$

From Eqs. (2.15) and (2.16), we get

$$\xi(x,t) = \frac{F_0}{4\pi\rho}\int_{-\infty}^{\infty}\frac{e^{-ikVt}}{c\boldsymbol{\chi}}\left(\frac{e^{-ik(c-V)t} - 1}{k(c-V)} + \frac{e^{ik(c+V)t} - 1}{k(c+V)}\right)e^{ikx}dk. \tag{2.17}$$

For practical application, we define the non-dimensional parameters as follows:

$$\tilde{x} = \frac{x}{H},\ \tilde{k} = kH,\ \tilde{G} = GH,\ \tilde{V} = \frac{V}{\sqrt{gH}},\ \tilde{c} = \frac{c}{\sqrt{gH}},\ \tilde{\omega} = \omega\sqrt{\frac{H}{g}},$$
$$\tilde{t} = t\sqrt{\frac{g}{H}},\ \tilde{\xi}(\tilde{x},\tilde{t}) = \frac{\xi(x,t)}{H},\ \tilde{N} = \frac{N}{\rho g H^2},\ \tilde{D} = \frac{D}{\rho g H^4},\ \tilde{F}_0 = \frac{F_0}{\rho g H}.$$

Considering the non-dimensional quantities, Eq. (2.17) gets simplified to the following expression:

$$\tilde{\xi} = \frac{\tilde{F}_0}{4\pi}\int_{-\infty}^{\infty}\frac{e^{\mathrm{i}\tilde{k}(\tilde{x}-\tilde{V}\tilde{t})}}{\tilde{c}\tilde{\boldsymbol{\chi}}}\left(\frac{(e^{-\mathrm{i}\tilde{\Psi}_1\tilde{t}}-1)}{\tilde{\Psi}_1}+\frac{(e^{\mathrm{i}\tilde{\Psi}_2\tilde{t}}-1)}{\tilde{\Psi}_2}\right)d\tilde{k}, \tag{2.18}$$

where $\tilde{\boldsymbol{\chi}} = \dfrac{\tilde{G}\tanh(\tilde{k})-\tilde{k}}{\tilde{G}-\tilde{k}\tanh(\tilde{k})}$, $\tilde{\Psi}_1 = \tilde{k}(\tilde{c}-\tilde{V})$, $\tilde{\Psi}_2 = \tilde{k}(\tilde{c}+\tilde{V})$, and $\tilde{c} = \sqrt{\dfrac{\tilde{D}\tilde{k}^4-\tilde{N}\tilde{k}^2+1}{\tilde{k}\tilde{\boldsymbol{\chi}}}}$. These are non-dimensional quantities for the terms present in the equation.

Beyond this, we shall utilise the notations without the tilde for convenience. Therefore, we rewrite Eq. (2.18) as follows:

$$\xi(x,t) = \frac{F_0}{4\pi}\int_{-\infty}^{\infty}\frac{e^{\mathrm{i}k(x-Vt)}}{c\boldsymbol{\chi}}\left(\frac{e^{-\mathrm{i}\Psi_1 t}-1}{\Psi_1}+\frac{e^{\mathrm{i}\Psi_2 t}-1}{\Psi_2}\right)dk, \tag{2.19}$$

where Ψ_1 and Ψ_2 are the phase functions. We introduce reference frame coordinates $X = x - Vt$ moving with the load. Therefore, Eq. (2.19) becomes

$$\xi(X) = \frac{F_0}{4\pi}\int_{-\infty}^{\infty}\frac{e^{\mathrm{i}kX}}{c\boldsymbol{\chi}}\left(\frac{e^{-\mathrm{i}\Psi_1 t}-1}{\Psi_1}+\frac{e^{\mathrm{i}\Psi_2 t}-1}{\Psi_2}\right)dk. \tag{2.20}$$

For simplicity in calculation, we express Eq. (2.20) in the following form:

$$\xi = \frac{F_0}{4\pi}(I_1+I_2+I_3), \tag{2.21}$$

where

$$I_1 = -\int_{-\infty}^{\infty}\frac{2ke^{\mathrm{i}kX}}{\boldsymbol{\chi}\Psi_1\Psi_2}dk, \tag{2.22}$$
$$I_2 = \int_{-\infty}^{\infty}\frac{e^{\mathrm{i}(kX-\Psi_1 t)}}{c\boldsymbol{\chi}\Psi_1}dk, \tag{2.23}$$
$$I_3 = \int_{-\infty}^{\infty}\frac{e^{\mathrm{i}(kX+\Psi_2 t)}}{c\boldsymbol{\chi}\Psi_2}dk. \tag{2.24}$$

It is important to note that the integrals I_2 and I_3 are time-dependent while I_1 is not. Let us denote the integrand of the integrals by $N_i(k)$, $i = 1, 2, 3$. In this problem, we analyze the deflection behavior with time, i.e., we want to compute the integrals asymptotically for large time ($t \to \infty$). We investigate the asymptotic contribution to the integral in Eq. (2.21) around the stationary points for various load speeds V, in an approach similar to the analysis accomplished by Schulkes and Sneyd (1988).

We consider only the integrals involving the phase function Ψ_1, since Ψ_2 is a monotonically increasing function with a non-negative derivative. Consequently, Ψ_2 lacks stationary points, leading to the rapid disappearance of the integral I_3 as $t \to \infty$. We discard I_3 and only consider terms that decline algebraically with time. We determine the contribution of the integral I_1 with the help of Cauchy's Residue Theorem. For the contribution of the stationary points for $t \to \infty$, we use the **Result 1** of Chapter 1 (pages 12–13).

We denote the zeros of Ψ_1 by k_x, k_y and k_z, where $0 < k_x < k_y < k_z$, and the stationary points by k_a, k_b, where $0 < k_a < k_b$. The phase function has real roots when $V \geq c_{\text{min}}$ corresponds to the wavenumbers at which the load and phase speeds are equal (see Fig. 2.2). We consider the zero k_x only when $V > c_{\text{min}}$, not for $V \leq c_{\text{min}}$, because, for this wavenumber, the group speed does not show an appropriate behavior. Our analysis asymptotically determines the deflection under various phase function behaviors affected by the speed of the load. Here, we discuss the solution for different speed regimes.

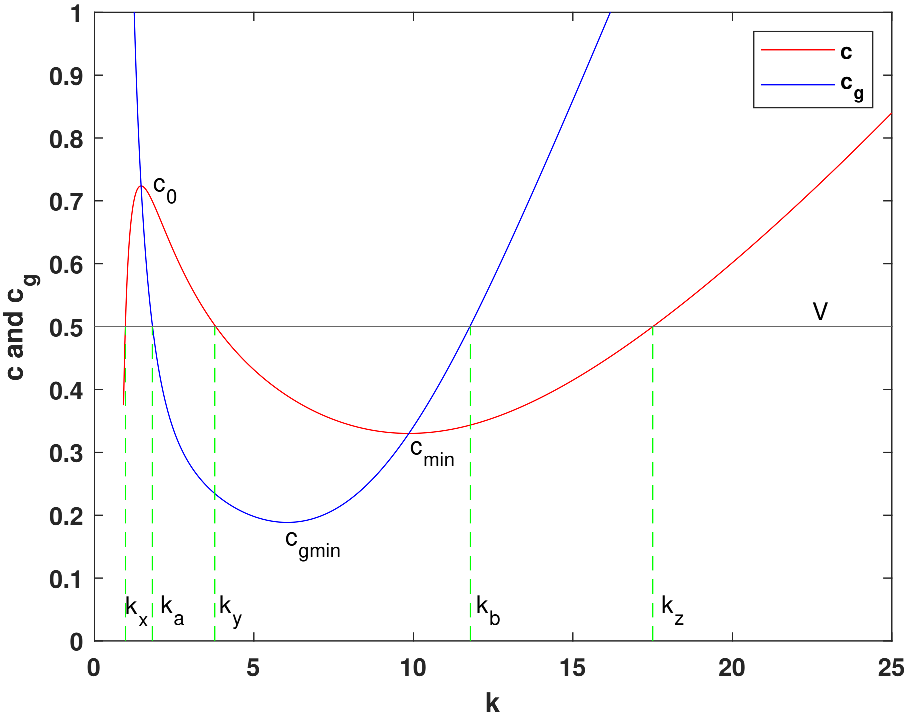

Figure 2.2: Phase and group speeds vs wavenumber k, concerning load speed V for fixed values $N = 0.004$ and $G = 0.6$.

Case 1:- $V \leq c_{\text{gmin}}$ (Subcritical source speed)
In this case, the integrands N_1 and N_2 are analytic in some neighborhood of real k. Therefore, the integral $I_2 \to 0$ as $t \to \infty$ by the Riemann-Lebesgue lemma. Thus, the plate

deflection can be written as

$$\xi_s(X,V) = -\frac{F_0}{4\pi} I_1. \tag{2.25}$$

Equation (2.25) presents the steady part of the solution. We can compute ξ_s numerically using numerical integration techniques or a Fast Fourier Transform (FFT).

Case 1a:- $\boldsymbol{V < c_{\text{gmin}}}$

The load moves with a constant speed V which is less than the minimum group speed of the waves. In this case, the phase function does not have any stationary points as well as zeros. It means that I_2 decays exponentially with time and so, the steady state is reached very rapidly.

Case 1b:- $\boldsymbol{V = c_{\text{gmin}}}$

The load moves with the minimum group speed of the waves, i.e., $V = c_{\text{gmin}}$. Then, the phase function has only one stationary point, namely, the inflexion point. Therefore, we use **Result 1** of Chapter 1 (pages 12–13) to get

$$I_2 = \left(\frac{\Gamma(1/3)}{3}\right) \frac{\cos\left(k_a X - \Psi_{1a} t + \frac{\pi}{6}\right)}{c_a \boldsymbol{\chi}_a \Psi_a} \left(\frac{6}{|c''_{ga}|}\right)^{1/3} t^{-1/3}. \tag{2.26}$$

Therefore, the deflection ξ is given by

$$\xi = \xi_s + \frac{F_0}{4\pi} \left(\frac{\Gamma(1/3)}{3}\right) \frac{\cos\left(k_a X - \Psi_{1a} t + \frac{\pi}{6}\right)}{c_a \boldsymbol{\chi}_a \Psi_a} \left(\frac{6}{|c''_{ga}|}\right)^{1/3} t^{-1/3}. \tag{2.27}$$

The transients resulting from a concentrated line load disappear as $t^{-1/3}$, as demonstrated by Eq. (2.27).

Case 2:- $\boldsymbol{c_{\text{gmin}} < V < c_{\text{min}}}$ (Subcritical source speed)

The load moves with a speed satisfying $c_{\text{gmin}} < V < c_{\text{min}}$. In this speed regime, the phase function has two different stationary points. Therefore, we use **Result 1** of Chapter 1 (pages 12–13) to get

$$I_2 = \left(\frac{\cos\left(k_a X - \Psi_{1a} t + \frac{\pi}{4}\right)}{c_a \boldsymbol{\chi}_a \Psi_{1a}} \left(\frac{\pi}{2|c'_{ga}|}\right)^{1/2} + \frac{\cos\left(k_b X - \Psi_{1b} t - \frac{\pi}{4}\right)}{c_b \boldsymbol{\chi}_b \Psi_{1b}} \left(\frac{\pi}{2|c'_{gb}|}\right)^{1/2} \right) t^{-1/2}. \tag{2.28}$$

The deflection is given by

$$\begin{aligned} \xi = \xi_s + \frac{F_0 t^{-1/2}}{4\pi} \Bigg[& \frac{\cos\left(k_a X - \Psi_{1a} t + \frac{\pi}{4}\right)}{c_a \boldsymbol{\chi}_a \Psi_{1a}} \left(\frac{\pi}{2|c'_{ga}|}\right)^{1/2} \\ & + \frac{\cos\left(k_b X - \Psi_{1b} t - \frac{\pi}{4}\right)}{c_b \boldsymbol{\chi}_b \Psi_{1b}} \left(\frac{\pi}{2|c'_{gb}|}\right)^{1/2} \Bigg]. \end{aligned} \tag{2.29}$$

In this case, the transients decay as $t^{-1/2}$. Here, ξ_s is the same as in Eq. (2.25) because, for $V < c_{\text{min}}$, Ψ_1 does not possess any zeros.

Case 3:- V $> \mathbf{c}_{\text{min}}$

When the load moves with supercritical speed, i.e., $V > c_{\text{min}}$, the phase function has three zeros (k_x, k_y and k_z) and two stationary points (k_a and k_b). We use the method of the steepest descents for solving the integrals asymptotically. Since the integrand is analytic in some neighborhood of the zeros, the integration contour can be deformed from the real k-axis in the complex k-plane. The contour of integration can be deformed to a contour on which the modulus of $e^{\mathrm{i}\Psi_1(k)t}$ has the reduced value $e^{-\delta t}$. But at the stationary points, this new contour deformation fails and the disjoint curves of the deformed contour must be connected by a straight line path of the steepest descent that passes through the stationary points (Schulkes and Sneyd (1988), Lighthill (2001)). Therefore, we may write

$$\xi = \frac{F_0}{4\pi}[I_{1C} + I_{2C}]. \tag{2.30}$$

In this integration, the path of the integration is the contour which replaces the real k-axis, and the integrals are as defined before.

When the source speed exceeds c_{min}, waves are generated. The displacement of the ice sheet is made up of two plane waves, one appears ahead of the load and the other appears behind. For the front waves, i.e., for $X > 0$, the contour of integration in the upper half plane is closed by a semi-circle. Therefore, by Jordan's lemma, the integration on the contour tends to zero. Thus, the Residue Theorem gives

$$\xi_s = \frac{\mathrm{i}F_0}{2}\sum \mathrm{Res}(N_1). \tag{2.31}$$

Therefore, we get

$$\xi_s = \frac{F_0}{V\boldsymbol{\chi}_z(c_{gz} - V)}\sin(k_z X) + \mathrm{Res}(X), \quad X > 0, \tag{2.32}$$

where $\mathrm{Res}(X)$ is the contribution due to the imaginary poles $\{\pm \mathrm{i}s_n,\ n\pi < s_n < (n+1)\pi\}$. In a similar manner, for the trailing wave, i.e., for $X < 0$, the contour of integration in the lower half plane is closed by a semi-circle. Therefore, by Jordan's lemma, the integration on the contour tends to zero. Thus, the Residue Theorem gives

$$\xi_s = \frac{F_0}{V}\left(\frac{\sin(k_x X)}{\boldsymbol{\chi}_x(V - c_{gx})} + \frac{\sin(k_y X)}{\boldsymbol{\chi}_y(V - c_{gy})}\right) + \mathrm{Res}(-X), \quad X < 0. \tag{2.33}$$

The integrand N_2 has four stationary points at $\pm k_a$, $\pm k_b$. Therefore, with the help of **Result 1** of Chapter 1 (pages 12–13), we conclude that I_2 provides the dominant contribution $t^{-1/2}$ as $t \to \infty$. Consequently, we can write

$$\xi = \begin{cases} \frac{F_0}{V\boldsymbol{\chi}_z(c_{gz}-V)}\sin(k_z X) + \left(\frac{\cos\left(k_a X - \Psi_{1a}t + \frac{\pi}{4}\right)}{c_a\boldsymbol{\chi}_a\Psi_{1a}}\left(\frac{\pi}{2|c'_{ga}|}\right)^{1/2} \right. \\ \left. + \frac{\cos\left(k_b X - \Psi_{1b}t - \frac{\pi}{4}\right)}{c_b\boldsymbol{\chi}_b\Psi_{1b}}\left(\frac{\pi}{2|c'_{gb}|}\right)^{1/2}\right) t^{-1/2} + \mathrm{Res}(X), \quad X > 0, \\ \\ \frac{F_0}{V}\left(\frac{\sin(k_x X)}{\boldsymbol{\chi}_x(V-c_{gx})} + \frac{\sin(k_y X)}{\boldsymbol{\chi}_y(V-c_{gy})}\right) + \left(\frac{\cos\left(k_a X - \Psi_{1a}t + \frac{\pi}{4}\right)}{c_a\boldsymbol{\chi}_a\Psi_{1a}}\left(\frac{\pi}{2|c'_{ga}|}\right)^{1/2} \right. \\ \left. + \frac{\cos\left(k_b X - \Psi_{1b}t - \frac{\pi}{4}\right)}{c_b\boldsymbol{\chi}_b\Psi_{1b}}\left(\frac{\pi}{2|c'_{gb}|}\right)^{1/2}\right) t^{-1/2} + \mathrm{Res}(-X), \quad X < 0. \end{cases} \tag{2.34}$$

The contribution of Res(X) of ξ_s will be significant only for the first few terms and in the vicinity of the load. Consequently, due to the discontinuity at the origin, we disregard Res(X) in the numerical computations (Schulkes and Sneyd (1988), Squire et al. (1996)).

Case 4:- V $= \mathbf{c}_{\min}$

The load moves with the minimum phase speed of waves, i.e., $V = c_{\min}$. In this case, the stationary point and the zero of the phase function coincide at a point k_m(say), which is a double zero of $\Psi_1(k)$. We have

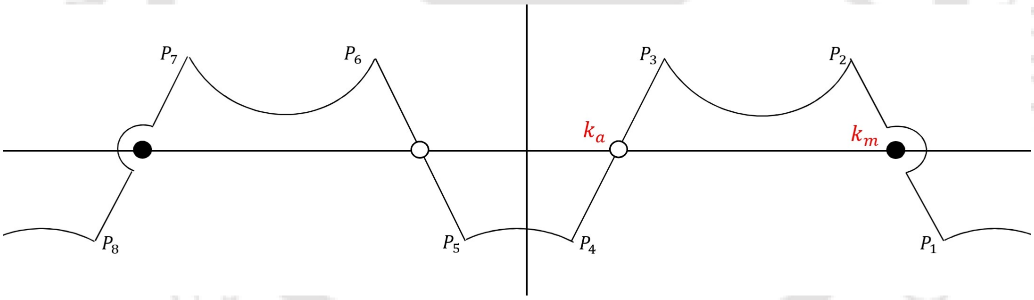

Figure 2.3: Integration contour for $V = c_{\min}$ in the complex k-plane.

$$\xi_s = \begin{cases} \mathrm{Res}(X), & X > 0, \\ -\frac{F_0}{V}\left(X\mu_m\cos(k_m X) + \mu'_m\sin(k_m X)\right) + \mathrm{Res}(-X), & X < 0, \end{cases} \tag{2.35}$$

where $\mu_m = \lim_{k \to k_m} \mu(k) = \lim_{k \to k_m}\left(\frac{(k-k_m)^2}{\boldsymbol{\chi}\Psi_1}\right)$. The integrand N_2 is exponentially smaller on C. In addition to the straight lines P_3P_4 and P_5P_6, it has indented paths P_1P_2 and P_7P_8 (Fig. 2.3). Thus, for finding the contribution of P_1P_2, we rotate the contour with the use of $k = (k_m - \mathrm{i}z)$. This substitution gives

$$\int_{P_1P_2} N_2 dk = \mathrm{i}\int_{C'} \frac{e^{\mathrm{i}(k_m - \mathrm{i}z)X}\mu(k_m - \mathrm{i}z)}{c(k_m - \mathrm{i}z)}\left(\frac{e^{\mathrm{i}z^2\tau}}{z^2}\right) dz + \mathcal{O}(e^{-at}), \tag{2.36}$$

where a is a positive constant and $\tau = \frac{1}{2}\Psi_1''(k_m)t$. We evaluate the integral with the help of Schulkes and Sneyd (1988) (Appendix formula (A8)) to get

$$\int_{P_1P_2} N_2(k)dk = \frac{-2\mathrm{i}\mu_m}{V}\left(\frac{\pi}{2}c'_{gm}t\right)^{1/2} e^{\mathrm{i}\left(k_mX+\frac{\pi}{4}\right)} + \frac{\pi e^{\mathrm{i}k_mX}}{V}(X\mu_m - \mathrm{i}\mu'_m). \tag{2.37}$$

We evaluate the contribution of the indented segment P_7P_8 in a similar fashion and combine them. Therefore, we get

$$\begin{aligned}\int_{P_1P_2+P_7P_8} N_2dk = &-\frac{4\mu_m}{V}\sin\left(k_mX+\frac{\pi}{4}\right)\left(\frac{\pi c'_{gm}t}{2}\right)^{1/2}\\ &+\frac{\pi X\mu_m}{V}\cos(k_mX)+\frac{\pi\mu'_m}{V}\sin(k_mX).\end{aligned} \tag{2.38}$$

We combine Eqs. (2.35) and (2.38) to get

$$\begin{aligned}\xi =&\frac{F_0\mu_m}{2Vk_m}\left(2\left(\frac{t}{t_m}\right)^{1/2}\sin\left(k_m|X|+\frac{\pi}{4}\right)+|k_mX|\cos(k_m|X|)+\alpha_m\sin(k_m|X|)\right)\\ &+\mathrm{Res}(|X|)+\mathcal{O}(t^{-1/2}),\end{aligned} \tag{2.39}$$

where $t_m = \dfrac{2\pi}{k_m^2 c'_{gm}}$ and $\alpha_m = \dfrac{k_m\mu'_m}{\mu_m}$. In Eq. (2.39), $\mathcal{O}(t^{-1/2})$ is the usual stationary phase contribution and the other term is dominant for large time with $\mathcal{O}(t^{1/2})$. Equation (2.39) gives the displacement growth with time as $t^{1/2}$ (Kheisin (1971), Schulkes and Sneyd (1988)).

Case 5:- $\mathbf{V = c_0}$

The load moves with a phase speed c_0 (say). When $V = c_0$, the zeros k_x, k_y and the stationary point k_a coincide at a point k_0 (say), which is a zero of order two. Apart from this, the phase function also has zero k_z and stationary point k_b. With the contribution of I_1, we get the static response given by

$$\xi_s = \begin{cases} \dfrac{F_0}{V\boldsymbol{\chi}_z(c_{gz}-V)}\sin(k_zX)+\mathrm{Res}(X), & X>0,\\ -\dfrac{F_0}{V}(X\mu_0\cos(k_0X)+\mu'_0\sin(k_0X))+\mathrm{Res}(-X), & X<0,\end{cases} \tag{2.40}$$

where $\mu_0 = \lim\limits_{k\to k_0}\left(\dfrac{(k-k_0)^2}{\boldsymbol{\chi}\Psi_1}\right)$. The integral's I_2 dominant contribution is similar to **Case 4**, except that the subscript m replaces 0. For this speed $V = c_0$, the displacement also grows with time as $\mathcal{O}(t^{1/2})$. The speed c_0 is entirely contingent upon the value of the porous-effect parameter G of the sea-bed. The variations in G cause comparable changes in the speed c_0. Further, the speed c_0 and G are inversely correlated; that is, when we increase G, c_0 falls, and when we reduce G, c_0 rises accordingly. In addition, there is no such speed in the absence of the porous effect of the sea-bed. This speed exists only if one takes into account the porous sea-bed. In the absence of a porous sea-bed, this case does not appear (Kheisin (1971), Schulkes and Sneyd (1988)).

Case 6:- $V > c_0$

When $V > c_0$, the phase function has two stationary points (k_a and k_b) and only one zero (k_z). Therefore, the expression for ξ can be obtained from Eq. (2.34) by simply putting $k_x = k_y = 0$. This case also appears only when the sea-bed is porous.

2.3 Numerical Results

2.3.1 Validation

We examine the current problem within the context of an impermeable sea-bed instead of a porous sea-bed. We find that the phase speed c and group speed c_g derived by Eq. (2.7) match with those phase and group speeds described in Schulkes et al. (1987). We provide a graphical depiction in Fig. 2.4 that plots c and c_g versus k using the same parameter values described in Schulkes et al. (1987) to validate the accuracy of our findings. Recall that non-dimensional parameters are used. Therefore, we transform the corresponding dispersion relation of Schulkes et al. (1987) into a non-dimensional form before creating these plots. Our analysis shows a consistent match with the outcomes of Schulkes et al. (1987).

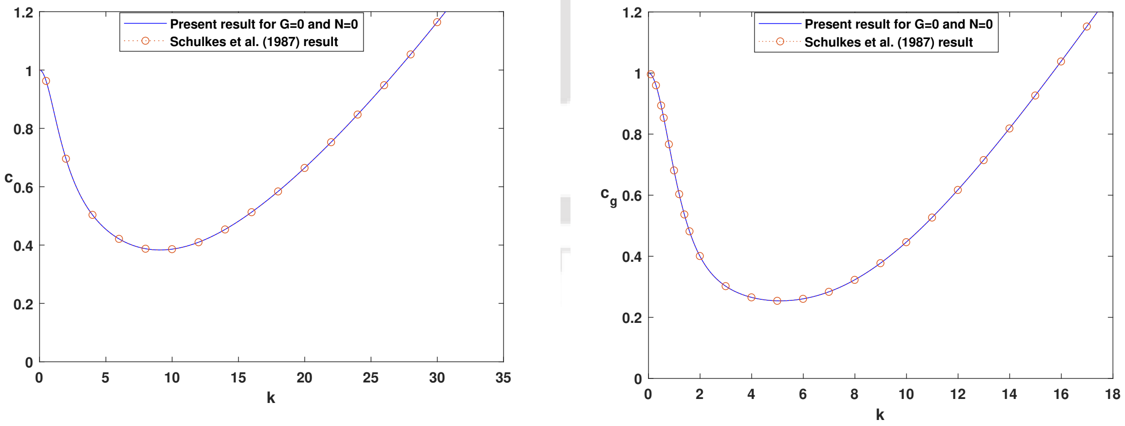

(a)

(b)

Figure 2.4: Validation against the work of Schulkes et al. (1987): (a) phase speed c; (b) group speed c_g against wavenumber k.

In the absence of stress ($N = 0$), when analyzing the problem for an impermeable sea-bed, the expression for ice deflection ξ derived in Eq. (2.21) coincides precisely with

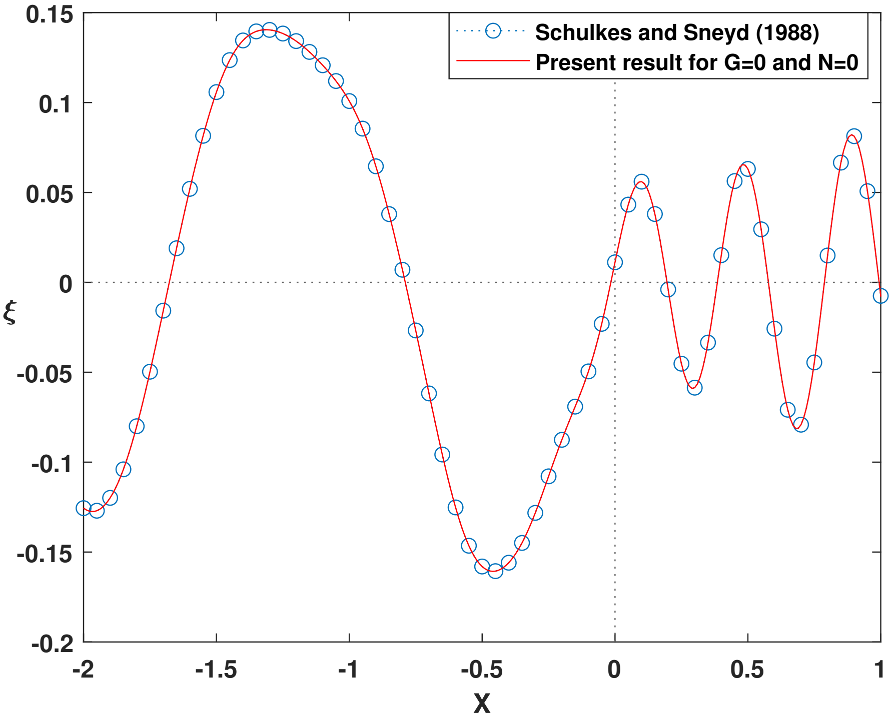

Figure 2.5: The ice displacement ξ for a supercritical non-dimensional speed $V = 0.51$ for $t = 10$.

the ice deflection form described by Schulkes and Sneyd (1988) for the supercritical speed regime where $V = 0.51 > c_{\text{min}}$. A graphical representation is provided in Fig. 2.5 to verify the accuracy of the current results.

The above validations point toward the efficiency of the present model and consequently, it allows us to proceed with the investigation.

2.3.2 Main Results

It will be useful to compute the development of the ice deflection numerically from the complete time-dependent calculations, namely Eq. (2.21), for the line load to support the asymptotic outcomes derived in the previous Section. The deflection shown in this subsection is in the frame of the motion of the load. It is preferable to exclude the constant factor $F_0/4\pi$ in Eq. (2.21) since the relative amplitude of the deflections, rather than their actual magnitudes, and the variations of the porous-effect parameter G and stress N are of utmost relevance.

In Fig. 2.6, we discuss the impact of different physical parameters, such as the porosity of the sea-bed and the stress on the phase speed. The phase speed decreases for an impermeable sea-bed, whereas it gradually increases in the presence of a porous seabed for a set of wavenumbers close to zero. Furthermore, the phase speeds coincide for impermeable and porous sea-beds beyond a certain value of the wavenumber. The effect of the stress on phase speeds is studied. It is observed that the phase speed is influenced by stress N. When $N = N_c$, c_{min} becomes zero at k_{min} (see Eq. (2.10)).

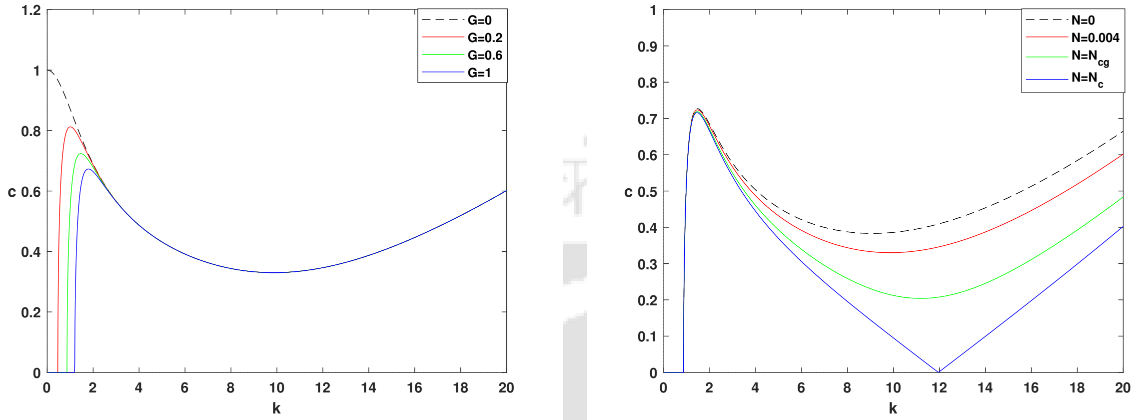

(a) (b)

Figure 2.6: Phase speed curves showing variations with respect to wavenumber: (a) for different values of the porous-effect parameter G and fixed $N = 0.004$; (b) for different values of stress N and fixed $G = 0.6$.

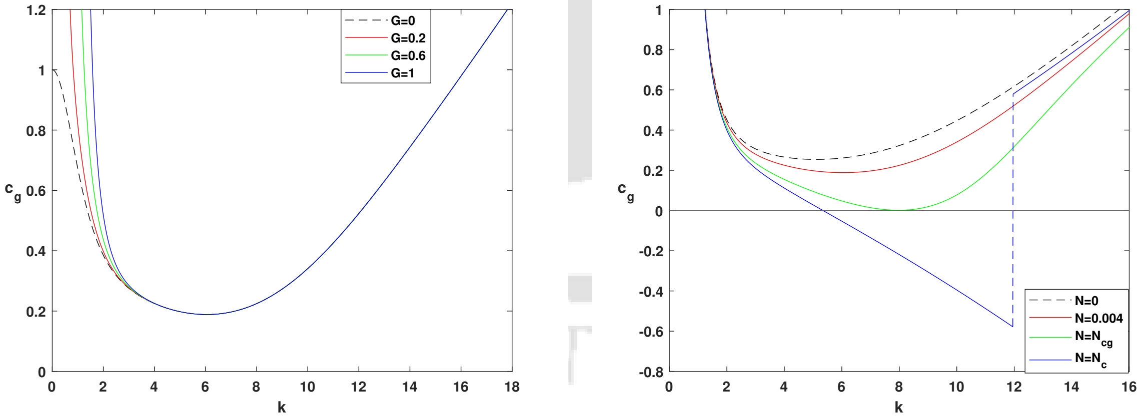

(a) (b)

Figure 2.7: Group speed curves showing variations with respect to wavenumber: (a) for different values of the porous-effect parameter G and fixed $N = 0.004$; (b) for different values of the stress N and fixed $G = 0.6$.

In Fig. 2.7, the plotted curves represent group speeds versus wavenumber for different values of the porous-effect parameter G and stress N. It is observed that a change in the group speed is evident within a certain range of wavenumbers while the remaining are equal within others. Furthermore, it is observed that the minimum group speed remains the same over various values of G, while it is affected by variations in N.

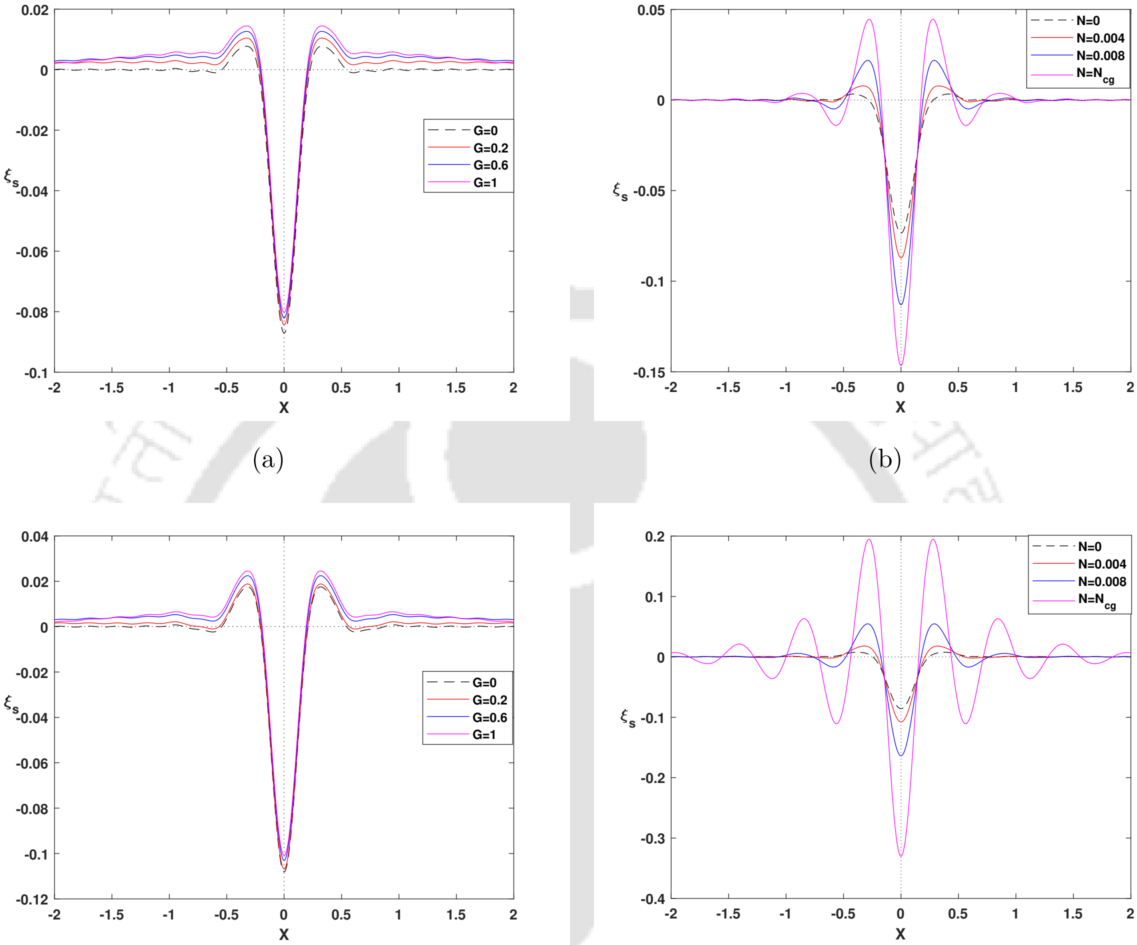

(a) (b)

(c) (d)

Figure 2.8: The steady ice displacement for various sub-critical non-dimensional source speeds: (a, b) $V = 0$; (c, d) $V = 0.18$.

Figure 2.8 represents the static deflection of the ice plate ξ_s versus $X = x - Vt$. The position of the load is at $X = 0$. The response of the ice plate is similar to the stationary load response. Here, we show the variation of the deflection with G and N. Figures 2.8(a, c) correspond to the variation in G for a fixed value $N = 0.004$ for two speeds $V = 0$ and $V = 0.18$, respectively. We notice that the deflection beneath the load decreases as the effect of the porous sea-bed increases. Also, there is no wave generated; the response is like a stationary load response. Figures 2.8(b, d) correspond to the variation in N for a fixed value of $G = 0.6$ for two load speeds $V = 0$ and $V = 0.18$, respectively. Here, the response is similar to the stationary load response for some value of N, because the minimum phase speed is influenced by the stress N (see Eq. (2.10)). When the load speed approaches c_{min}, a wave is generated (Takizawa (1985), Squire et al. (1996)). Therefore, for $N = N_c$, waves are generated because the minimum phase speed is zero for this stress value. Further, the deflection beneath the load is affected by N, i.e., the deflection increases as the stress increases.

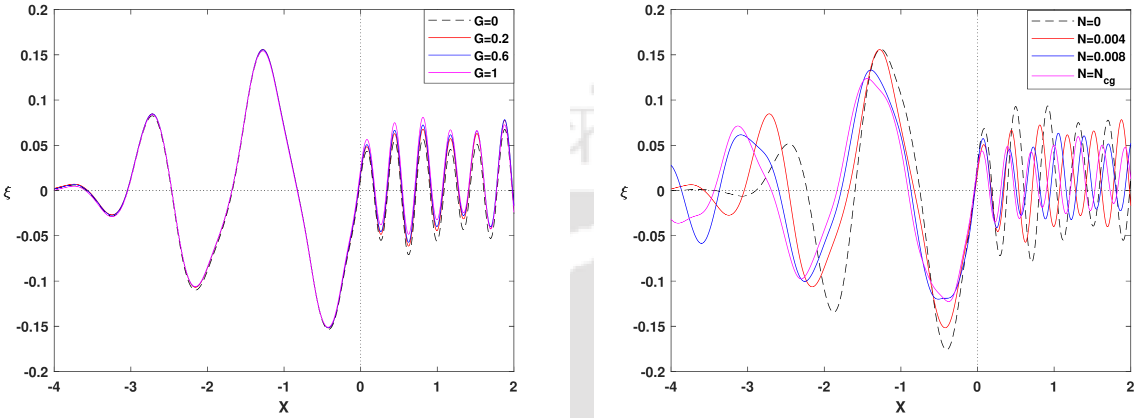

(a) (b)

Figure 2.9: The transformation of the ice displacement for the movement of the load at supercritical non-dimensional source speed $V = 0.50 > c_{\mathrm{min}}$ at $t = 10$: (a) for different values of the porous-effect parameter G and fixed $N = 0.004$; (b) for different values of the stress N and fixed $G = 0.6$.

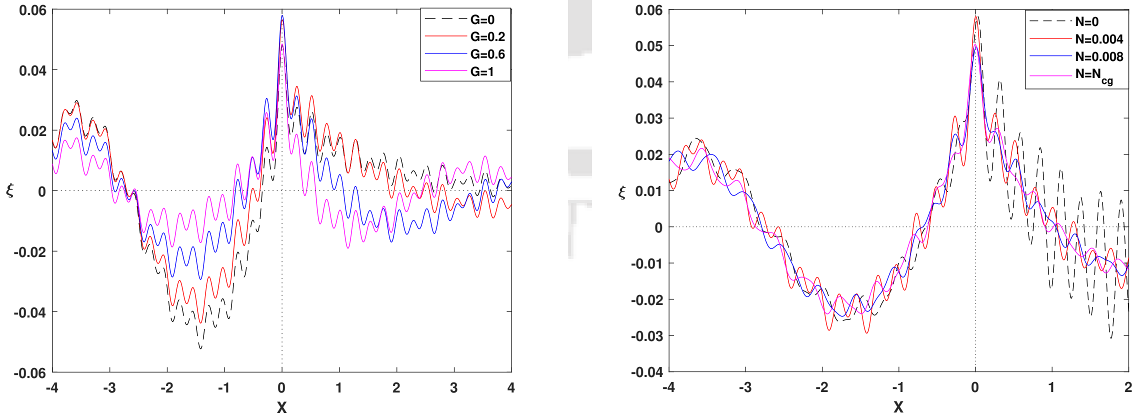

(a) (b)

Figure 2.10: The transformation of the ice displacement for the movement of the load at higher supercritical non-dimensional source speed $V = 0.84 > c_0$ at $t = 10$: (a) for different values of the porous-effect parameter G and fixed $N = 0.004$; (b) for different values of the stress N and fixed $G = 0.6$.

Figures 2.9 and 2.10 show the deflection ξ plotted against $X = x - Vt$. In Fig. 2.9, waves of the same wavelength are generated for different effects of the porous sea-bed. Large waves get generated behind the load while flexural-gravity waves get generated in front of the load. When the load moves at a higher supercritical source speed ($V > c_0$), only the short wave train travels ahead of the load whereas the long waves appear behind the load. It is noticed that, for the trailing wave, the amplitude of the waves decreases when the porosity is increased but the wavelength is the same. When we increase time, only the shadow zone appears behind the load as in Hosking and Milinazzo (2022). As the load speed increases, the rear side waves exhibit longer wavelengths, leading to a wider depression around the load position. Correspondingly, the variation of the displacement with porous-effect parameter and stress coefficient is shown in Figs. 2.10 (a, b), respectively.

2.4 Conclusion

We construct a mathematical model to explain the waves generated in a floating ice sheet due to a moving concentrated line load over a porous sea-bed. The analysis looks at the impact of the porous-effect parameter of the sea-bed and stress on both phase and group speeds. A significant change is observed in the phase speed for smaller wavenumbers in the case of the porous sea-bed. However, it is observed that the minimum phase speed and minimum group speed show the same behavior for the impermeable as well as porous sea-bed, but the variation in the stress coefficient N shows the changes in the phase as well as group speed. The impact of the stress and porous-effect parameters on the phase and group speeds is investigated for both shallow and deep water cases, taking into account the limiting cases for the present system. It is found that the stress and the porous sea-bed have significant impacts on the wave generation in a floating plate caused by a moving load. The porous sea-bed influences the plate deflection at a steadily moving load on a floating ice sheet, but it does not affect the wavelength of the generated waves. The amplitude of the generated waves decreases as the stress and porous-effect parameter increase. There are two critical speeds in the porous sea-bed scenario where the displacement grows as $t^{1/2}$. With the source, the displacement approaches a stable state with transients that decay as $t^{-1/2}$ or $t^{-1/3}$, which is consistent with the behavior observed in the impermeable sea-bed case. However, there are two critical speeds $V = c_{\text{min}}$ and $V = c_0$ in the porous sea-bed scenario where the displacement grows as $t^{1/2}$. The findings of this work is expected to show the way for solving problems in connection with ice sheet deflection related to a porous sea-bed.

CHAPTER 3

Response of a floating ice sheet due to a moving load in the presence of an undulating sea bottom

3.1 Problem Formulation

Linear water waves are assumed to propagate from the negative x-direction over an undulating sea-bed with the free surface covered by a laterally infinite homogeneous ice sheet having density ρ_i and a small constant thickness h. We consider a Cartesian coordinate system with the z-axis pointing vertically upward and $z = 0$ as the upper surface. The constant density of water is taken as ρ. The depth of the sea, except for the undulating portion, is considered at $z = -H$, where H is constant; the undulating portion of the sea-bed is considered between $x = L_1$ and $x = L_2$. The model is depicted in Fig. 3.1. Now onward, the thin ice sheet will be considered as a thin plate following the thin plate theory. Linear water wave theory and irrotational motion of the fluid allow the velocity potential $\Phi(x, z, t)$ to satisfy the Laplace's equation

$$\Phi_{xx} + \Phi_{zz} = 0 \quad \text{in} \quad -\infty < x < \infty,\ -H + \varepsilon b(x) \le z \le 0, \tag{3.1}$$

where $z = -H + \varepsilon b(x)$ denotes the undulating sea-bed. In this context, $b(x)$ is a continuous, bounded function describing the undulating nature of the bottom with $b(x) \to 0$ as $|x| \to \infty$, which ensures that the ocean maintains a uniform finite depth H away from the undulation on both sides. The parameter $\varepsilon(\ll 1)$ represents a small quantity that indicates the smallness of the undulation. The condition on the undulating bottom is

$$\Phi_{\mathbf{n}} = 0 \ \text{ on } \ z = -H + \varepsilon b(x), \tag{3.2}$$

where subscript **n** denotes the normal at a point (x, z) on the bottom. The conditions on the upper surface $z = 0$ are given by (Davys et al. (1985))

$$\Phi_z - \xi_t = 0, \tag{3.3}$$

$$D\nabla^4\xi + \rho g\xi + \rho\Phi_t + f(x, t) = 0. \tag{3.4}$$

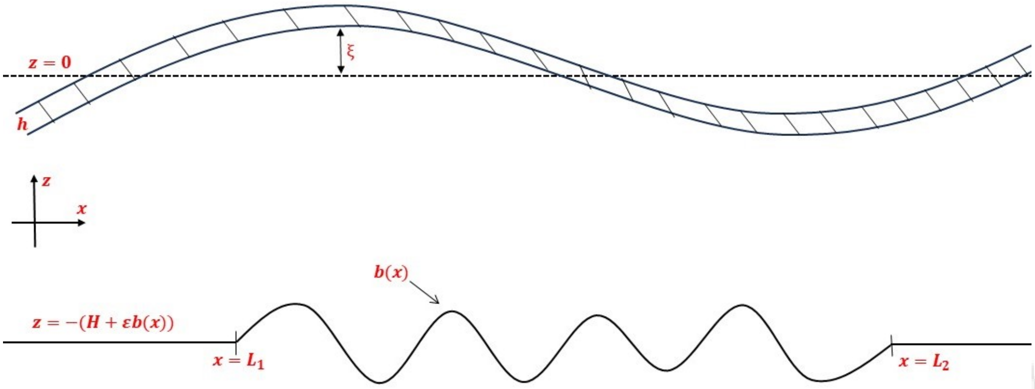

Figure 3.1: Schematic representation of an ice sheet over an undulating sea-bed

The bottom condition (3.2) can be approximated up to the first order of the small parameter ε, as in Martha and Bora (2007), as

$$\Phi_z + \varepsilon\left[\partial_x\{b(x)\Phi_x\}\right] = 0, \text{ on } z = -H. \tag{3.5}$$

For convenience, we use the perturbation series expansions for Φ and ξ in terms of the same dimensionless parameter ε used in the undulating sea-bed expression. Thus, Φ and ξ can written in the following perturbation series:

$$\Phi = \Phi_0 + \varepsilon\Phi_1 + \mathcal{O}(\varepsilon^2), \tag{3.6}$$

$$\xi = \xi_0 + \varepsilon\xi_1 + \mathcal{O}(\varepsilon^2), \tag{3.7}$$

where Φ_0 and ξ_0, respectively, represent the solutions for Φ and ξ before the wave interaction with the undulating sea-bed takes place.

In order that the component of the fluid velocity normal to the sea-bed be zero at the boundary, the interaction between the unperturbed flow (which would occur in the absence of the boundary disturbances) and the perturbed one is considered as a new source of fluid motion. This new first-order source is located on the plane surface. Combining all the equations and conditions, we may consider the complete BVP as

$$\Phi_{xx} + \Phi_{zz} = 0 \quad \text{in} \quad -\infty < x < \infty, \ -H + \varepsilon b(x) \le z \le 0, \tag{3.8}$$

$$\Phi_z - \xi_t = 0 \quad \text{at} \quad z = 0, \tag{3.9}$$

$$D\nabla^4\xi + \rho g\xi + \rho\Phi_t + f(x,t) = 0 \quad \text{at} \quad z = 0, \tag{3.10}$$

$$\Phi_z + \varepsilon\mathcal{Q}(x,t) = 0 \quad \text{at} \quad z = -H, \tag{3.11}$$

where $\mathcal{Q}(x,t) = [\partial_x\{b(x)\Phi_x\}]$. The governing equation and boundary conditions, correct to order ε^0, are

$$\Phi_{0xx} + \Phi_{0zz} = 0 \quad \text{in} \quad -\infty < x < \infty, \; -H + \varepsilon b(x) \le z \le 0, \tag{3.12}$$

$$\Phi_{0z} - \xi_{0t} = 0 \quad \text{at} \quad z = 0, \tag{3.13}$$

$$D\nabla^4\xi_0 + \rho g\xi_0 + \rho\Phi_{0t} + f(x,t) = 0 \quad \text{at} \quad z = 0, \tag{3.14}$$

$$\Phi_{0z} = 0 \quad \text{at} \quad z = -H. \tag{3.15}$$

The governing equation and boundary conditions, correct to order ε, can be written as follows:

$$\Phi_{1xx} + \Phi_{1zz} = 0 \quad \text{in} \quad -\infty < x < \infty, \; -H + \varepsilon b(x) \le z \le 0, \tag{3.16}$$

$$\Phi_{1z} - \xi_{1t} = 0 \quad \text{at} \quad z = 0, \tag{3.17}$$

$$D\nabla^4\xi_1 + \rho g\xi_1 + \rho\Phi_{1t} + f(x,t) = 0 \quad \text{at} \quad z = 0, \tag{3.18}$$

$$\Phi_{1z} + \mathcal{Q}_0(x,t) = 0 \quad \text{at} \quad z = -H, \tag{3.19}$$

where $\mathcal{Q}_0(x,t) = [\partial_x\{b(x)\Phi_{0x}\}]$.

At the order ε^0, the BVP indicates that the sea bottom ripples have no influence on Φ_0. Initially, we assume that ξ_0 in the solution, to the order of ε^0, is provided by $\xi_0 = A_0 e^{\mathrm{i}(kx-\omega t)}$. Hence, in order to satisfy Eqs. (3.12)-(3.15), the corresponding potential function Φ_0 without the external force effect is given by

$$\Phi_0 = \frac{A_0}{\mathrm{i}\omega}\left(\frac{Dk^4}{\rho} + g\right)\frac{\cosh(k(z+H))}{\cosh(kH)}e^{\mathrm{i}(kx-\omega t)}, \tag{3.20}$$

where the dispersion relation connects ω to H and k. The dispersion relation is given by

$$\omega^2 = \left(\frac{Dk^4}{\rho} + g\right)k\tanh(kH). \tag{3.21}$$

It is pertinent to point out that the dispersion relation holds in the solution for ε up to first order (Davies and Heathershaw (1984)). Moreover, the expressions for the phase speed c and group speed c_g are given by $c = \omega/k$, and $c_g = d\omega/dk$, respectively.

We consider Φ_1 to be a bounded function. Moreover, we suppose that, as $|x| \to \infty$, all of Φ_1 and its first and second-order derivatives approach zero. The above criterion allows the use of Fourier transform of Φ_1 with respect to x. We take the Fourier transform of Eqs. (3.16) to (3.19) with respect to x to get the transformed BVP as

$$\hat{\Phi}_{1zz} - m^2\hat{\Phi}_1 = 0 \quad \text{in} \quad -\infty < m < \infty, \; -H + \varepsilon\hat{b}(m) \le z \le 0, \tag{3.22}$$

$$\hat{\Phi}_{1z} - \hat{\xi}_{1t} = 0 \quad \text{at} \quad z = 0, \tag{3.23}$$

$$Dk^4\hat{\xi}_1 + \rho g\hat{\xi}_1 + \rho\hat{\Phi}_{1t} + \hat{f}(m,t) = 0 \quad \text{at} \quad z = 0, \tag{3.24}$$

$$\hat{\Phi}_{1z} + \hat{\mathfrak{Q}}_0(m,t) = 0 \quad \text{at} \quad z = -H, \tag{3.25}$$

where m is the transformed variable, $\hat{\Phi}_1(m,z,t)$ is the Fourier transform of $\Phi_1(x,z,t)$, $\hat{\xi}_1(m,t)$ is the Fourier transform of $\xi_1(x,t)$, $\hat{b}(m)$ is the Fourier transform of $b(x)$ and

$$\hat{\mathfrak{Q}}_0(m,t) = \int_{L_1}^{L_2} \mathfrak{Q}_0(x,t)e^{-\mathrm{i}mx}dx = \Lambda(m)e^{\mathrm{i}\omega t}.$$

Solving Eq. (3.22) subject to the conditions (3.24) to (3.25), we get the following:

$$\begin{aligned}\hat{\Phi}_1 = &\left(\frac{Dm^4}{\rho} + g\right)\frac{\cosh(m(z+H))}{\cosh(mH)}\frac{\hat{\xi}_1}{\mathrm{i}\omega} + \frac{\hat{f}(m,t)\cosh(m(z+H))}{\mathrm{i}\rho\omega\cosh(mH)}\\ &+\frac{\Lambda(m)e^{\mathrm{i}\omega t}}{m\sinh(mH)}\left(\frac{\cosh(m(z+H))}{\cosh(mH)} + \cosh(mz)\right).\end{aligned} \tag{3.26}$$

Therefore, from Eq. (3.23), we get the ordinary differential equation

$$\frac{d\hat{\xi}_1}{dt} + \mathrm{i}\omega\hat{\xi}_1 = \frac{\hat{f}(m,t)}{\mathrm{i}\rho\omega}m\tanh(mH) + \frac{\Lambda(m)e^{\mathrm{i}\omega t}}{\cosh(mH)}. \tag{3.27}$$

Moving ahead, a concentrated line load is imposed at initial time $t = 0$ which moves in the positive x-direction with a constant velocity V. The loading function $f(x,t)$ is considered in the form $f(x,t) = F(x - Vt)u(t) = F_0\delta(x - Vt)u(t)$, where F_0 is the force applied perpendicular to the ice surface per unit area, $\delta(.)$ is the Dirac delta function and $u(t)$ is the Heaviside unit step function. Consequently, the Fourier transform of the loading function takes the form

$$\hat{f}(m,t) = \frac{F_0}{\sqrt{2\pi}}e^{-\mathrm{imVt}}.$$

Therefore, using the initial condition $\hat{\xi}_1(m,0) = 0$, we solve Eq. (3.27) to obtain $\hat{\xi}_1$ as

$$\hat{\xi}_1 = \frac{F_0}{\sqrt{2\pi}}\frac{m\tanh(mH)}{\rho\omega(\omega - mV)}\left(e^{-\mathrm{i}\omega t} - e^{-\mathrm{i}mVt}\right) + \frac{\Lambda(m)}{2\mathrm{i}\omega\cosh(mH)}\left(e^{\mathrm{i}\omega t} - e^{-\mathrm{i}\omega t}\right). \tag{3.28}$$

Invoking inverse Fourier transform, ξ_1 can be evaluated as

$$\xi_1(x,t) = \frac{1}{\sqrt{2\pi}}\int_{-\infty}^{\infty}\hat{\xi}_1(m,t)e^{\mathrm{i}mx}dm. \tag{3.29}$$

From Eqs. (3.28) and (3.29), we get

$$\begin{aligned}\xi_1(x,t) =&\frac{F_0}{2\pi\rho}\int_{-\infty}^{\infty}\frac{m\tanh(mH)}{\omega(\omega - mV)}\left(e^{-\mathrm{i}\omega t} - e^{-\mathrm{i}mVt}\right)e^{\mathrm{i}mx}dm\\ &+\frac{1}{\sqrt{2\pi}}\int_{-\infty}^{\infty}\frac{\Lambda(m)}{2\mathrm{i}\omega\cosh(mH)}\left(e^{\mathrm{i}\omega t} - e^{-\mathrm{i}\omega t}\right)e^{\mathrm{i}mx}dm,\end{aligned} \tag{3.30}$$

which can be rewritten as

$$\begin{aligned}\xi_1(x,t) =& \frac{F_0}{2\pi\rho}\int_{-\infty}^{\infty}\frac{m\tanh(mH)}{\omega(\omega-mV)}\left(e^{-\mathrm{i}(\omega-mV)t}-1\right)e^{\mathrm{i}m(x-Vt)}dm \\ &+\frac{1}{\sqrt{2\pi}}\int_{-\infty}^{\infty}\frac{\Lambda(m)}{2\mathrm{i}\omega\cosh(mH)}\left(e^{\mathrm{i}\omega t}-e^{-\mathrm{i}\omega t}\right)e^{\mathrm{i}mx}dm. \qquad (3.31)\end{aligned}$$

3.2 Particular Bedform

The characteristics of the bedform $b(x)$ and the unperturbed zeroth-order potential Φ_0 determine the particular form of $\Lambda(m)$. To use sinusoidal ripples as a specific bedform, the following function can be used to describe $b(x)$:

$$b(x) = b_0\sin(lx+\alpha), \qquad (3.32)$$

where b_0 is the amplitude of the ripple, l the ripple wavenumber, and α any phase angle. We express the bed elevation as follows so that there is continuity at the uneven zone boundaries. For the purpose of retaining the bed elevation at the ends of the roughness, we take

$$L_1 = -L,\ L_2 = L,\ \alpha = 0, \qquad (3.33)$$

where $L = n\pi/l$ and n is a positive integer. Using the above bedform $b(x)$ along with (3.33), we get the expression for $\Lambda(m)$ as

$$\Lambda(m) = (-1)^{n+1}\mathcal{A}\frac{(2m/l)\sin((k-m)L)}{((k-m)/l)^2-1}, \qquad (3.34)$$

where

$$\mathcal{A} = \frac{A_0 b_0 k}{\omega\cosh(kH)}\left(\frac{Dk^4}{\rho}+g\right).$$

Introducing the reference frame coordinates $X = x - Vt$ moving with the load, Eq. (3.31) takes the following form:

$$\xi_1(X) = \sum_{i=1}^{4} I_i, \qquad (3.35)$$

where

$$I_1 = -\frac{F_0}{2\pi\rho}\int_{-\infty}^{\infty}\frac{m\tanh(mH)}{\omega\Psi_1}e^{\mathrm{i}mX}dm, \qquad (3.36)$$

$$I_2 = \frac{F_0}{2\pi\rho}\int_{-\infty}^{\infty}\frac{m\tanh(mH)}{\omega\Psi_1}e^{\mathrm{i}(mX-\Psi_1 t)}dm, \qquad (3.37)$$

$$I_3 = -\frac{(-1)^n\mathcal{A}}{2\mathrm{i}\sqrt{2\pi}}\int_{-\infty}^{\infty}\frac{2ml\sin((k-m)L)}{((k-m)^2-l^2)\omega\cosh(mH)}e^{\mathrm{i}(mX+\Psi_2 t)}dm, \qquad (3.38)$$

$$I_4 = \frac{(-1)^n \mathscr{A}}{2\mathrm{i}\sqrt{2\pi}} \int_{-\infty}^{\infty} \frac{2ml\sin((k-m)L)}{((k-m)^2-l^2)\omega\cosh(mH)} e^{\mathrm{i}(mX-\Psi_1 t)} dm, \tag{3.39}$$

with $\Psi_1 = \omega - mV$ and $\Psi_2 = \omega + mV$.

Denoting the integrands of the above integrals by $N_i(k)$, $i = 1, 2, 3, 4$, the asymptotic contribution to the integral associated with the stationary points for various load speeds can be determined, using a similar approach as in Schulkes and Sneyd (1988). Since Ψ_2 is a strictly increasing function, it does not have any stationary points. Therefore, the integral associated with Ψ_2 has no contribution from the method of stationary phase. On the other hand, Ψ_1 has stationary points and zeros, contributing significantly to the asymptotic behavior of the integral. Let us denote the zeros of Ψ_1 by m_y, m_z $(0 < m_y < m_z)$ and the stationary points by m_a, m_b $(0 < m_a < m_b)$.

We now find the stationary points and determine the pole contributions. We notice that the integrals I_3 and I_4 have poles, which are associated with the bottom ripples. As a result, we proceeed to determine the poles of both integrands and the contributions they make.

We evaluate the pole contribution of the integrals I_3 and I_4 with the help of the Residue Theorem. There are two simple poles: $m = k \pm l$. The pole $m = k - l$ approaches the pole $m = -k$ as a particular case when $l \to 2k$, which is the situation of Bragg resonance (Davies and Heathershaw (1984)). Therefore, the pole contribution of the integrals is obtained using an approach similar to the one in Davies (1980) and Davies (1982a). We calculate the pole contributions of the integrals I_3 and I_4 and merge them to get the final expression as

$$\sqrt{\frac{\pi}{2}} \frac{(-1)^n \mathscr{A}}{\omega\cosh(kH)} \frac{(2k/l)\sin(2kL)}{((2k/l)^2-1)} \times \left(e^{\mathrm{i}(-kX+(\omega-kV)t)} - e^{-\mathrm{i}(kX+(\omega+kV)t)}\right) = \mathscr{I}_p(\text{say}). \tag{3.40}$$

A Bragg resonance between the surface waves and the bed forms is indicated by the equation when the wavenumber of the bedform is twice the wavenumber component of the wave along the x-axis $(2k = l)$. This phenomenon was explained by Davies (1982b), Heathershaw (1982) and Mei (1985). The Bragg scattering condition results in the reflected wave being perfectly reinforced by the reflections from the preceding waves (Dalrymple and Kirby (1986)).

With regard to the evaluation of the contribution of the stationary points, **Result 1** of Chapter 1 (pages 12–13) is used. Now, we discuss the behavior of ξ_1 for different speed regimes.

Case 1a:- $V < c_{\text{gmin}}$

The function Ψ_1 increases monotonically if the load speed V is less than the minimum group speed c_{gmin}, demonstrating the absence of stationary points. As an outcome, the transient deflection approaches the steady state rapidly as it decreases exponentially with time.

Case 1b:- $V = c_{\text{gmin}}$
For this case, the function Ψ_1 has a stationary point, namely an inflection point, which is denoted by $m = m_a$, i.e., $\Psi_1'(m_a) = \Psi_1''(m_a) = 0,\ \Psi_1'''(m_a) \neq 0$. Therefore, we can write

$$\xi_1 = \xi_s + \mathscr{G}_p + \frac{\Gamma(1/3)}{3}\left(\frac{3!}{t|\Psi'''_{1a}|}\right)^{1/3}\left(\frac{F_0\alpha_a}{2\pi\rho} - (-1)^n\mathscr{B}_a\frac{\sin((k-m)L)}{((k-m_a)^2-l^2)}\right)e^{\mathrm{i}(m_aX - t\Psi_{1a} + \pi/6)}, \tag{3.41}$$

where ξ_s represents the steady deflection corresponding to the integral I_1, and

$$\alpha_a = \frac{m_a\tanh(m_aH)}{\omega_a\Psi_{1a}},\quad \mathscr{B}_a = \frac{\mathrm{i}\mathscr{A}m_al}{\sqrt{2\pi}\omega_a\cosh(m_aH)}.$$

The subscript 'a' indicates the value of a variable at $m = m_a$. A prime ($'$) indicates differentiation with respect to m. The stationary points dominate the overall behavior of ξ_1 and the transients decay as $t^{-1/3}$.

Case 2:- $c_{\text{gmin}} < V < c_{\text{min}}$
In this speed regime, Ψ_1 has two stationary points $(m_a,\ m_b)$, i.e., $\Psi_1'(m_a) = \Psi_1'(m_b) = 0,\ \Psi_1''(m_a) \neq 0,\ \Psi_1''(m_b) \neq 0$. Therefore, we have the expression of ξ_1 as

$$\begin{aligned}\xi_1 = &\left(\frac{F_0\alpha_a}{2\pi\rho} - (-1)^n\mathscr{B}_a\frac{\sin((k-m_a)L)}{((k-m_a)^2-l^2)}\right)\left(\frac{\pi}{2t|\Psi''_{1a}|}\right)^{1/2} e^{\mathrm{i}(m_aX - t\Psi_{1a} + \pi/4)} \\ &+ \left(\frac{F_0\alpha_b}{2\pi\rho} - (-1)^n\mathscr{B}_b\frac{\sin((k-m_b)L)}{((k-m_b)^2-l^2)}\right)\left(\frac{\pi}{2t|\Psi''_{1b}|}\right)^{1/2} e^{\mathrm{i}(m_bX - t\Psi_{1b} - \pi/4)} + \xi_s + \mathscr{G}_p, \end{aligned} \tag{3.42}$$

where α_a, $\mathscr{B}_a$ are the same as earlier and α_b, $\mathscr{B}_b$ are the values at $m = m_b$. For this case, the observation is that the transients decay as $t^{-1/2}$.

Case 3:- $c_{\text{min}} < V < \sqrt{gH}$
In this speed regime, Ψ_1 has two stationary points $(m_a,\ m_b)$ and two zeros $(m_y,\ m_z)$, i.e., $\Psi_1(m_y) = \Psi_1(m_z) = 0$ and $\Psi_1'(m_a) = \Psi_1'(m_b) = 0,\ \Psi_1''(m_a) \neq 0,\ \Psi_1''(m_b) \neq 0$. Since the integral is analytic in some neighborhood of the zeros, the contour is deformed in the complex m-plane. We use the steepest descent method and solve in a similar manner as in Schulkes and Sneyd (1988) and Lighthill (2001). We obtain the pole contribution by the Residue Theorem to have

$$\xi_s = \begin{cases} \frac{F_0\sin(m_zX)}{\rho V(c_{gz}-V)}\tanh(m_zH) + \mathrm{Res}(X), & X > 0, \\ -\frac{F_0\sin(m_yX)}{\rho V(c_{gy}-V)}\tanh(m_yH) + \mathrm{Res}(-X), & X < 0. \end{cases} \tag{3.43}$$

In above, $\mathrm{Res}(X)$ indicates the contribution due to the imaginary poles of ξ_s which is significant only for the first few terms and in the vicinity of the load. As a result, due to the discontinuity at the origin, $\mathrm{Res}(X)$ is discarded in the numerical calculations (Schulkes and Sneyd (1988)).

The displacement is mainly made up of two plane waves with phase speeds identical to the speed of the load, resulting in wave crests that appear stationary to the source. The shorter wavelength is situated in front of the load because its group speed exceeds the source speed ($c_{gz} > V$), whereas the longer wavelength appears behind the source (Schulkes and Sneyd (1988)). The time-dependent integrals give the dominant contribution of $\mathcal{O}(t^{-1/2})$ as $t \to \infty$. The expression of ξ_1 is given by

$$\begin{aligned}\xi_1 = &\left(\frac{F_0\alpha_a}{2\pi\rho} - (-1)^n\mathcal{B}_a\frac{\sin((k-m_a)L)}{((k-m_a)^2-l^2)}\right)\left(\frac{\pi}{2t|\Psi''_{1a}|}\right)^{1/2} e^{\mathrm{i}(m_aX - t\Psi_{1a}+\pi/4)}\\ &+\left(\frac{F_0\alpha_b}{2\pi\rho} - (-1)^n\mathcal{B}_b\frac{\sin((k-m_b)L)}{((k-m_b)^2-l^2)}\right)\left(\frac{\pi}{2t|\Psi''_{1b}|}\right)^{1/2} e^{\mathrm{i}(m_bX - t\Psi_{1b}-\pi/4)}\\ &+\frac{F_0\sin(m_zX)}{\rho V(c_{gz}-V)}\tanh(m_zH) + \mathcal{I}_p + \mathrm{Res}(X), \quad X > 0. \end{aligned} \tag{3.44}$$

The above expression for ξ_1 is equivalent to the case $X < 0$, using y in place of z. In addition, the coefficient of $\sin(m_yX)$ has the opposite sign.

Case 4:- $V > \sqrt{gH}$

Ψ_1 has a single zero (m_z) and a single stationary point (m_b) if the load moves at a higher speed ($V > \sqrt{gH}$). The expression for ξ_1 can be derived from the previous case by setting m_y and m_a to zero.

Case 5:- $V = c_{\min}$

If the load speed V equals $c_{\min}$, then Ψ_1 has a double zero at m_0 (say). This happens because the points m_a, m_y, and m_z coincide at m_0.

The integral can be evaluated with the help of the residue theorem as

$$I_1 = \begin{cases} \mathrm{Res}(X), & X > 0,\\ \\ -\frac{F_0}{\rho V}\left(X\mu_0\cos(m_0X) + \mu_0'\sin(m_0X)\right) + \mathrm{Res}(-X), & X < 0, \end{cases} \tag{3.45}$$

where $\mu = \dfrac{(m-m_0)^2\tanh(mH)}{\Psi_1}$. Here, the integrand N_2 is exponentially smaller on $\mathbf{C}$, and in addition to the straight-line paths P_6P_5 and P_4P_3, it has indented paths P_8P_7 and P_2P_1 (Fig. 3.2). For determining the contribution from P_2P_1, we rotate the contour with the substitution $m = m_0 - \mathrm{i}z$. This substitution gives

$$\int_{P_2P_1} N_2(m)dm = \mathrm{i}\int_{C'} e^{\mathrm{i}(m_0-\mathrm{i}z)X}\left(\frac{\mu(m_0-\mathrm{i}z)}{c(m_0-\mathrm{i}z)}\right)\frac{e^{\frac{1}{2}\mathrm{i}z^2\Psi_1''t}}{z^2}dz + \mathcal{O}(e^{-\beta t}), \tag{3.46}$$

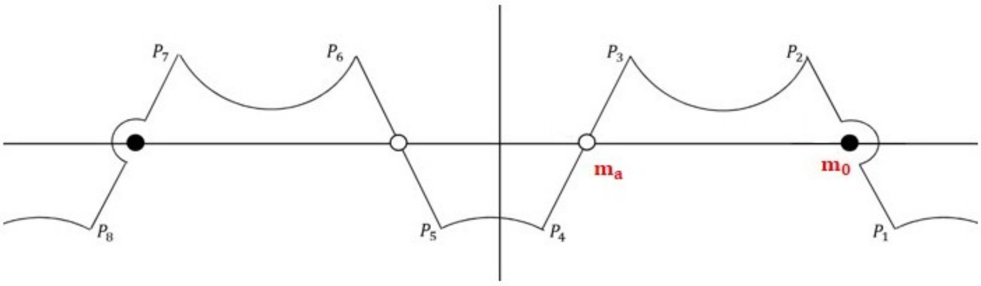

Figure 3.2: Integration contour for I_2 for $V = c_{min}$.

where β is a positive constant.

The approach described by Schulkes and Sneyd (1988) is used to directly evaluate the integral in Eq. (3.46), yielding the following result:

$$\int_{P_2P_1} N_2(m)dm = -\frac{2\mathrm{i}\mu_0}{V}\left(\frac{\pi}{2}\Psi_1''(m_0)\right)^{1/2} e^{\mathrm{i}(m_0X+\pi/4)} + \frac{\pi(X\mu_0 - \mathrm{i}\mu_0')}{V}e^{\mathrm{i}m_0X}. \tag{3.47}$$

In a similar manner, we evaluate the contribution of the indented segment P_8P_7 and merge both of them. Consequently, we have

$$\begin{aligned}\int_{P_2P_1+P_8P_7} N_2(m)dm = &-\frac{4\mu_0}{V}\sin(m_0X+\pi/4)\left(\frac{\pi c_{g0}' t}{2}\right)^{1/2} + \frac{\pi X\mu_0}{V}\cos(m_0X)\\ &+\frac{\pi\mu_0'}{V}\sin(m_0X).\end{aligned} \tag{3.48}$$

Thus, the final expression of ξ_1 is obtained as

$$\begin{aligned}\xi_1 = &\frac{F_0\mu_0}{\rho m_0 V}\left[\left(\frac{t}{t_0}\right)^{1/2}\sin(m_0X+\pi/4) + \frac{|m_0X|}{2}\cos(m_0X) + \alpha_j\sin(|m_0X|)\right]\\ &+\mathcal{J}_p + \mathrm{Res}(|X|) + \mathcal{O}(t^{-1/2}),\end{aligned} \tag{3.49}$$

where $t_0 = 2/\pi c_{g0}'$ and $\mathcal{O}(t^{-1/2})$ is the usual stationary phase contribution while the other term is dominant for large time with $\mathcal{O}(t^{1/2})$.

Case 5:- $V = \sqrt{gH}$

If the load speed V is equal to $\sqrt{gH}$, then Ψ_1 is likely to have a triple zero at the origin because the points m_a and m_y merge. The contour **C** must be indented around the origin, as Fig. 3.3 indicates. Therefore, with the help of the Residue Theorem, we evaluate the integral I_1 as

$$\xi_s = \begin{cases} \frac{F_0\tanh(m_zH)}{\rho V(c_{gz}-V)}\sin(m_zX) + \mathrm{Res}(X), & X > 0,\\ \\ \frac{3F_0X}{\rho V^2H} + \mathrm{Res}(-X), & X < 0.\end{cases} \tag{3.50}$$

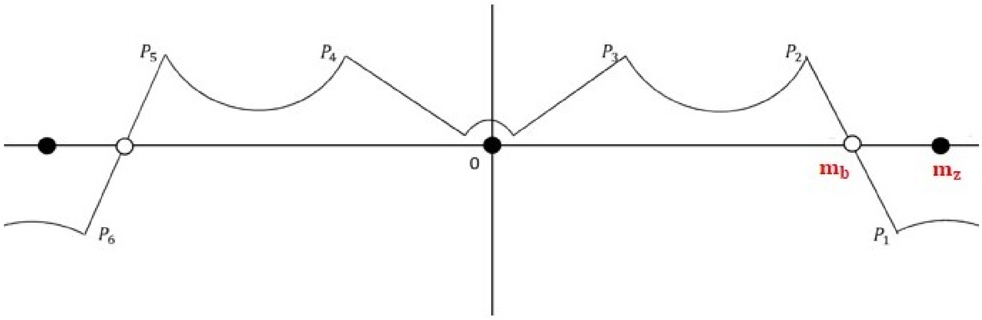

Figure 3.3: Integration contour for I_2 for $V = \sqrt{gH}$

The contribution of the integrand N_2 is given by

$$\int_{P_3P_4} N_2(m)dm = \frac{6\sqrt{3}\Gamma(2/3)}{V^2 t_1^{1/3}} t^{1/3} - \frac{4\pi X}{V^2 H}. \tag{3.51}$$

Therefore, the final expression of ξ_1 is given by

$$\xi_1 = \begin{cases} \frac{F_0 \tanh(m_z H)}{\rho V(c_{gz} - V)} \sin(m_z X) + \frac{F_0}{\rho V^2}\left[\Upsilon(t/t_1)^{1/3} - \frac{X}{H}\right] \\ + \mathcal{I}_p + \text{Res}(X), & X > 0, \\ \\ \frac{F_0}{\rho V^2}\left[\Upsilon(t/t_1)^{1/3} + \frac{2X}{H}\right] + \mathcal{I}_p + \text{Res}(-X), & X < 0, \end{cases} \tag{3.52}$$

where $t_1 = \dfrac{6}{V^2}$, and $\Upsilon = \dfrac{3\sqrt{3}\Gamma(2/3)}{2\pi}$. In Eq. (3.52), the deflection grows with time as $\mathcal{O}(t^{1/3})$.

3.3 Numerical Results

The deflection ξ_1 of the ice sheet, given by Eq. (3.35), is calculated numerically and presented for various values of different parameters. We consider the physical parameters given by Takizawa (1985): Young'smodulus $E = 5.1 \times 10^8 \text{N/m}^2$, Poisson's ratio $\nu = 1/3$, plate thickness $h = 0.17\text{m}$, water density $\rho = 1026\text{kg/m}^3$, ice-density $\rho_i = 947\text{kg/m}^3$, water depth $H = 6.8\text{m}$, $g = 9.8\text{m/s}^2$. The parameters for the undulating sea-bed are set as follows: $L = 100\text{m}$ and $A_0 = 0.5\text{m}$, which are kept constant throughout the study unless otherwise mentioned. The ripple wavelength is $\lambda_r = 2\pi/l$, where $l = n\pi/L$.

There are some limitations in the solution due to the linearization of the boundary conditions, as well as the general requirement of the method. These limitations have been discussed in detail by Davies (1980) and Davies (1982a) and can be expressed as a set of simple conditions on various length scales like as A_0k, A_0/H, b_0/H, b_0l, etc. Additionally, the restriction on the sea-bed ripple amplitude b_0 suggests that the ratio b_0/H must be small in practice. For larger values of b_0/H, the present model is likely to fail. Based on this restriction, we consider the maximum value of the ratio b_0/H to be approximately 0.32.

The response of the ice sheet is plotted for various ripple numbers and amplitude of the undulating sea-bed for each speed; ξ_1 is plotted against $X = x - Vt$ in the figures and the load is positioned at $X = 0$ for these figures.

3.3.1 Validation

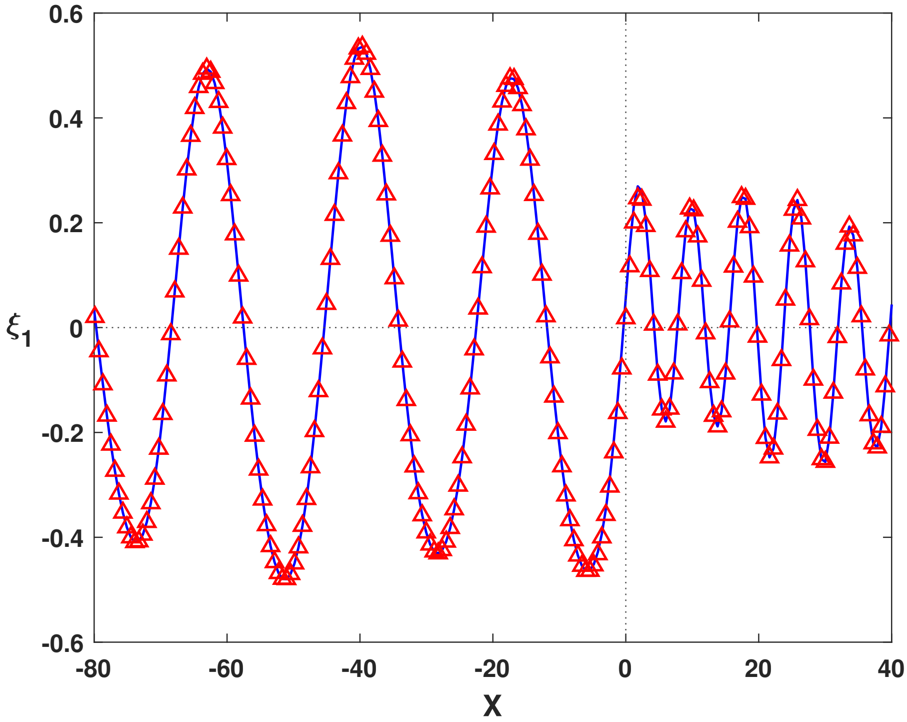

Figure 3.4: Comparison of the present study: the solid line shows the present study, while the triangle markers △ correspond to the study of Hosking and Milinazzo (2022).

In order to validate our results against some available work, we consider our problem for the case of an impermeable flat sea-bed rather than an undulating sea-bed so that it can be compared with the result of Hosking and Milinazzo (2022). In the absence of the sea-bed undulation, for $b_0 = 0$, the ice deflection ξ_1 calculated in Eq. (3.35) closely fits the ice deflection form given in Hosking and Milinazzo (2022) with a speed $V = 5.9$m/s at $t = 80$s. The values $E = 1.79 \times 10^8 \mathrm{N/m}^2$ and $h = 0.14$m are set to be consistent with the values considered by them, while all other parameters are kept unchanged. A graphical comparison is presented in Fig. 3.4 for ξ_1 against $X = x - Vt$, with the triangle markers denoting the results in Hosking and Milinazzo (2022) and the solid line representing the outcome of the current study. This makes it clear that our findings match closely with those presented by Hosking and Milinazzo (2022), confirming the precision of our analysis.

This validation enables us to move ahead with certainty for further studies to discuss various issues related to the problem.

3.3.2 Main Results

Figure 3.5 represents a phase speed and group speed graph. It indicates that, for waves with higher wavenumbers, or shorter wavelengths, both phase speed and group speed are higher.

For the case of an undulating bed, the ripple number and ripple wavenumber are interrelated ($l = n\pi/L$). Resonance occurs due to the interaction between the waves of the surface and the sea-bed. The peak resonance takes place when the wavenumber of the bottom undulation approaches twice that of the surface, as predicted by Davies and Heathershaw (1984). In our study, we evaluate our results around the peak resonance zone, which is for $2k \approx l$.

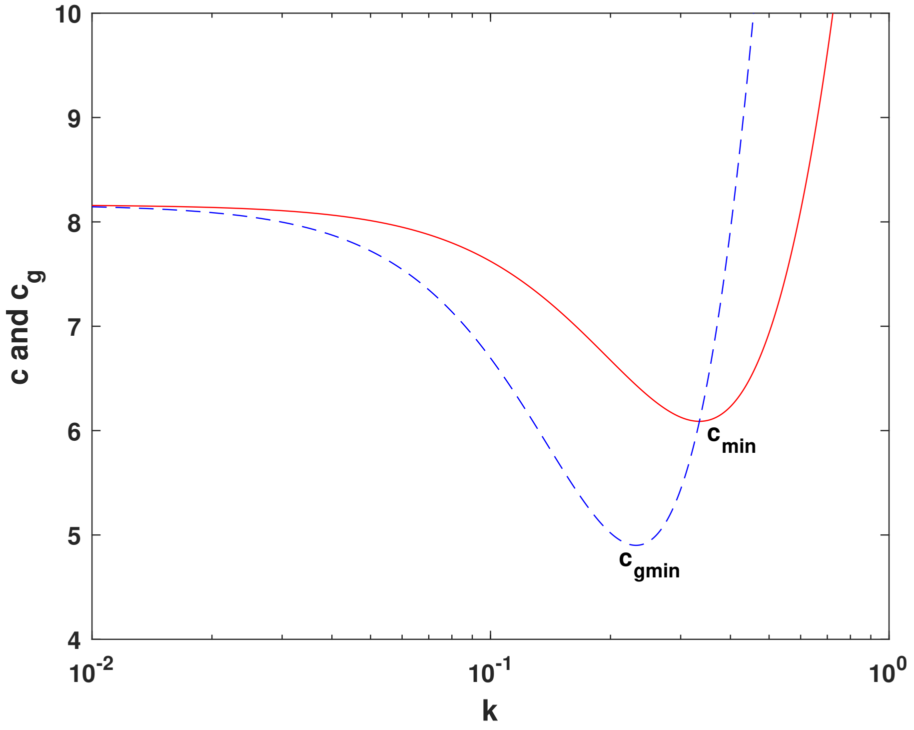

Figure 3.5: The phase speed c and group speed c_g curves, which are symmetric about the origin, are shown for Takizawa (1985) data. The wavenumber k scale is logarithmic.

Three different speed regimes are taken into consideration: $V < c_{\min}$, $c_{\min} < V < \sqrt{gH}$, and $V > \sqrt{gH}$. Figures 3.6 and 3.7 correspond to the speed regime $V = 5.5\text{m/s} < c_{\min}$, Figs. 3.8 and 3.9 correspond to $c_{\min} < V = 7.1\text{m/s} < \sqrt{gH}$, while Figs. 3.10 and 3.11 correspond to $V = 9.2\text{m/s} > \sqrt{gH}$. These figures present ξ_1 against $X = x - Vt$. The minimum phase speed $c_{\min} \approx 6.01\text{m/s}$ and $\sqrt{gH} = 8.16\text{m/s}$ are considered.

The floating ice sheet responds similarly to a stationary load when a load travels at a speed $V < c_{\min}$. However, when the vehicle speed reaches or exceeds the minimum phase speed $c_{\min}$, waves are generated. As described by Takizawa (1985), the ice deflection pattern can be classified into the symmetric/asymmetric transition mode when $V < c_{\min}$.

At low speeds, the wave pattern in the ice sheet closely matches that of a stationary load. This indicates that, at low speeds, the load remains at the center of the depression, resulting in a symmetrical deflection profile about the load position. This type of wave pattern is observed in Figs. 3.6 and 3.7, when $V = 5.5\text{m/s} < c_{\min}$. Furthermore, for a given speed, the ice deflection just beneath the load is always high, indicating that the depression surrounding the load stays high. When the load accelerates, this depression seems to move slightly backward (Takizawa (1988)).

Figures 3.6 and 3.7, respectively, represent the behavior of the floating ice sheet due to a moving load with a speed $V = 5.5\text{m/s}$, with varying sea-bed ripple number n and ripple amplitude b_0. The effect of the increasing number of sea-bed ripples with a constant ripple amplitude $b_0 = 1.5\text{m}$ is shown in Fig. 3.6. As n increases, the waves in the front zone ($X > 0$) become more oscillatory due to higher frequency interactions with the sea-bed, whereas the rear waves ($X < 0$) stay relatively smooth. With an increment in the number of ripples n, the wavenumber l of the ripples increases, causing the wavelength λ_r to decrease. In other words, a higher number of ripples n corresponds to a shorter wavelength. From the relationship between frequency and wavelength, a decrease in wavelength leads to an increase in frequency, resulting in higher-frequency interactions, which contribute to the oscillatory behavior observed in the pattern. Furthermore, the deflection beneath the load is determined to be the lowest for 2 ripples and maximum for 10 ripples, i.e., for an increase in the number of ripples.

When the wave amplitudes decrease, the energy in the rear waves decays more quickly; the wave patterns are influenced by b_0 (Fig. 3.7). Furthermore, as the amplitude of the ripple increases, the depression reduces. In other words, a flat bed shows the maximum depression, whereas the maximum ripple amplitude demonstrates the least. We may say that, as the depth decreases (measured from the crest), the depression also decreases. This pattern of behavior is consistent across all speed regimes. The waves oscillate and gradually decrease in amplitude as we move far away from the load position, showing the disappearance of the disturbance with distance. When it becomes distant, the front waves decay more quickly than the rear waves; this persists for all values of b_0. The wavelength of the front waves is shorter than that of the rear waves. All three speed regimes exhibit this phenomenon.

Figures 3.8 and 3.9 represent the behavior of the generated waves due to a high critical load speed $V = 7.1\text{m/s}$ for various values of n and b_0, respectively, while Figs. 3.10 and 3.11 represent the same corresponding to a high critical load speed $V = 9.2\text{m/s}$.

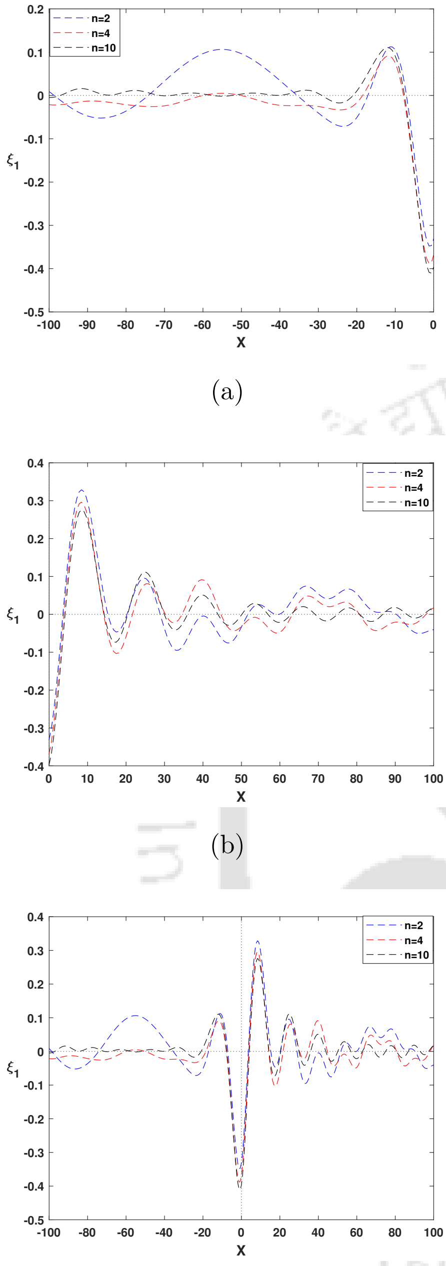

(a)

(b)

(c)

Figure 3.6: Ice plate deflection for movement of a load with a speed $V = 5.5\text{m/s}$ at $t = 10\text{s}$ for various number of ripples (n) with fixed ripple amplitude $b_0 = 1.5\text{m}$, showing the generated wave patterns: (a) Wave pattern in front of the load; (b) Wave pattern behind the load; (c) Combined representation of front and rear waves.

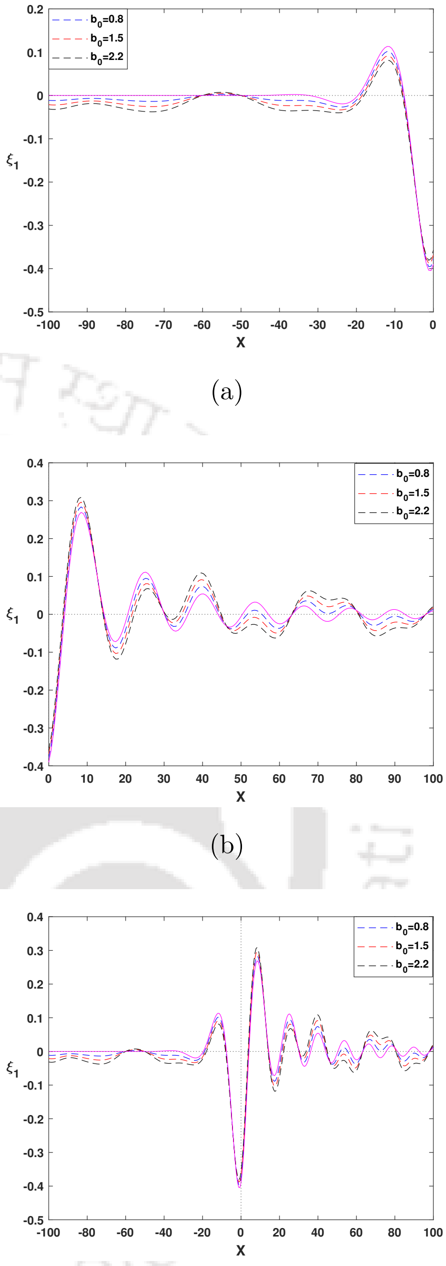

(a)

(b)

(c)

Figure 3.7: Ice plate deflection for movement of a load with a speed $V = 5.5\text{m/s}$ at $t = 10\text{s}$ for various ripple amplitude (b_0) with a fixed $n = 4$, showing the generated wave patterns. The solid line represents the flat bed: (a) Wave pattern in front of the load; (b) Wave pattern behind the load; (c) Combined representation of front and rear waves.

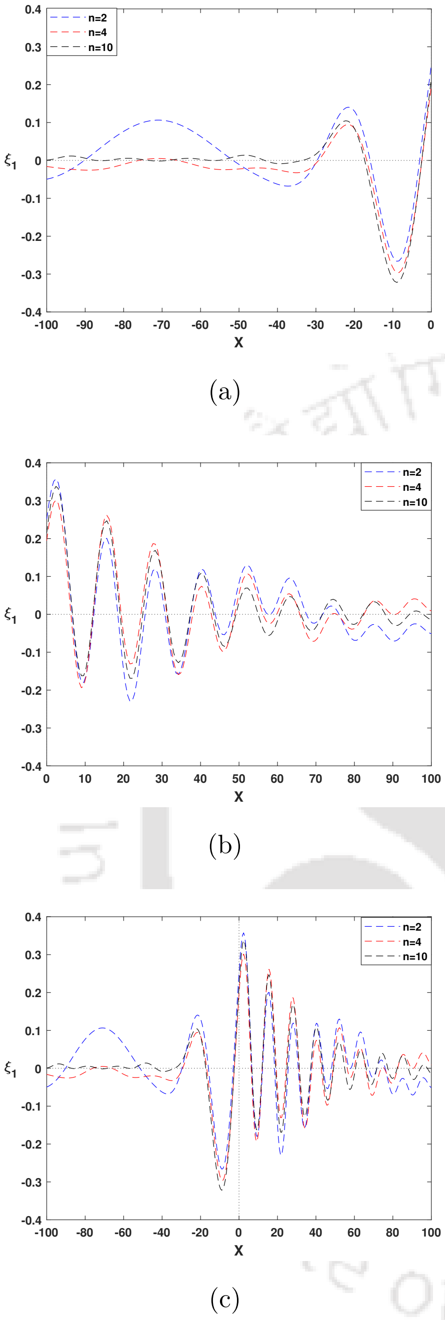

Figure 3.8: Ice plate deflection for movement of a load with a speed $V = 7.1\text{m/s}$ at $t = 10\text{s}$ for various number of ripples (n) with fixed ripple amplitude $b_0 = 1.5\text{m}$, showing the generated wave patterns: (a) Wave pattern in front of the load; (b) Wave pattern behind the load; (c) Combined representation of front and rear waves.

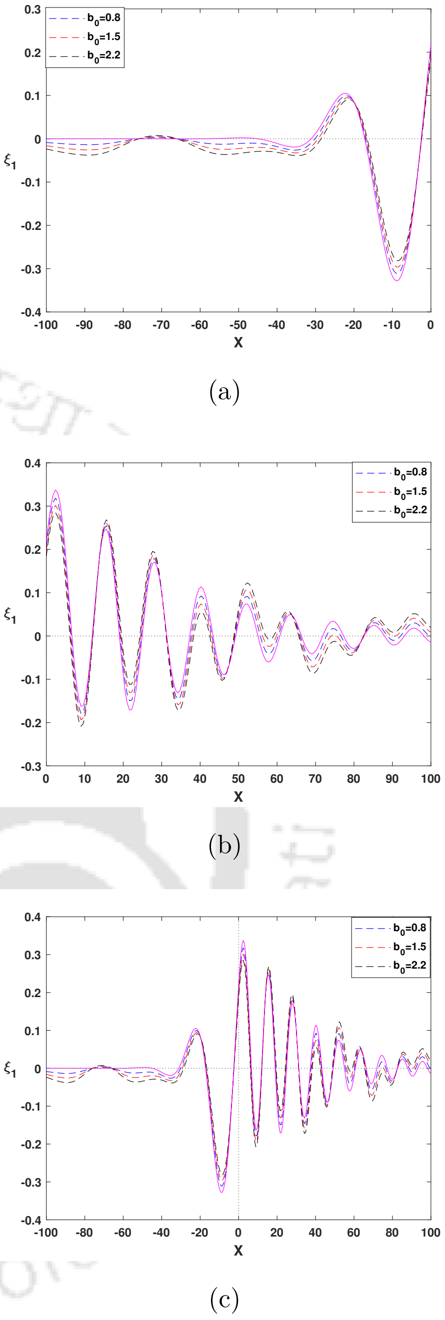

Figure 3.9: Ice plate deflection for movement of a load with a speed $V = 7.1\text{m/s}$ at $t = 10\text{s}$ for various ripple amplitude (b_0) with fixed $n = 4$, showing the generated wave patterns. The solid line represents the flat bed: (a) Wave pattern in front of the load; (b) Wave pattern behind the load; (c) Combined representation of front and rear waves.

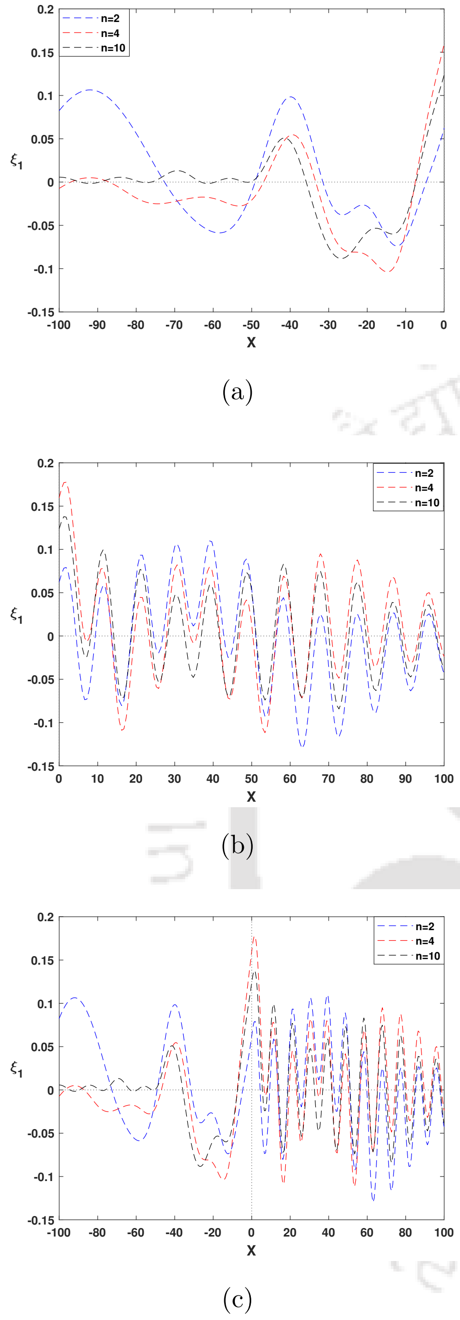

(a)

(b)

(c)

Figure 3.10: Ice plate deflection for movement of a load with a speed $V = 9.2$m/s at $t = 10$s for various number of ripples (n) with fixed ripple amplitude $b_0 = 1.5$m, showing the generated wave patterns: (a) Wave pattern in front of the load; (b) Wave pattern behind the load; (c) Combined representation of front and rear waves.

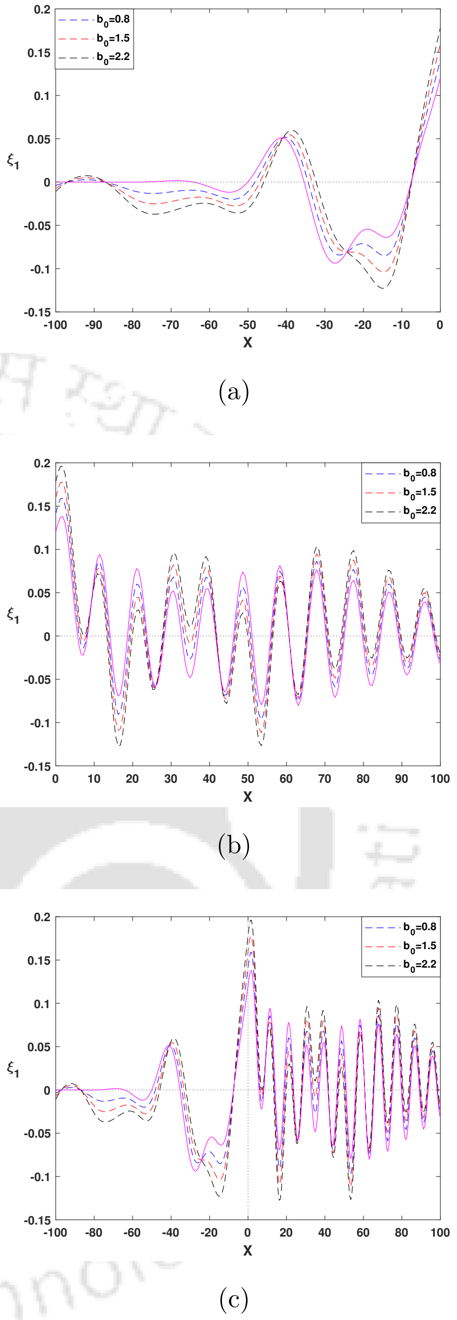

(a)

(b)

(c)

Figure 3.11: Ice plate deflection for movement of a load with a speed $V = 9.2$m/s at $t = 10$s for various ripple amplitude (b_0) with a fixed $n = 4$, showing the generated wave patterns. The solid line represents the flat bed: (a) Wave pattern in front of the load; (b) Wave pattern behind the load; (c) Combined representation of front and rear waves.

For the speed case $V > \sqrt{gH}$, only short waves appear ahead of the load and a shadow zone appears behind the load. The flexural waves predominate because the wavelength of the waves ahead of the load shortens as the load speed increases. This occurs, because at high speed $V > \sqrt{gH}$, the load crosses the curve of phase speed in higher wavenumber zone. However, there is no noticeable interaction with the smaller wavenumber region ($k \to 0$). That is why the wavelength gets longer. Subsequently, longer following transients are seen behind the load, slowly disappearing. These longer-wavelength waves create a “shadow zone”, which expands with time as the trailing transients progressively separate from the load as in Hosking and Milinazzo (2022). We may say that the depression around the load expands when $V > \sqrt{gH}$ (Figs. 3.10 and 3.11). As a consequence, under this speed regime, the gravity waves are mostly obstructed on the rear side of the load and the flexural waves are more likely to propagate ahead. Figures 3.12(a) and 3.12(b) show the behavior for ripple numbers $n = 10$ and $n = 100$, respectively. We observe that, when the number of ripples increases, the ice behavior approaches that for a sea-bed without undulation. This happens because the wavelength of the sea-bed ripples decreases as the ripple number increases (for a certain domain length). The individual impact on the ice response may become minimal if the ripples become much smaller in comparison with the dominant wave components in the system.

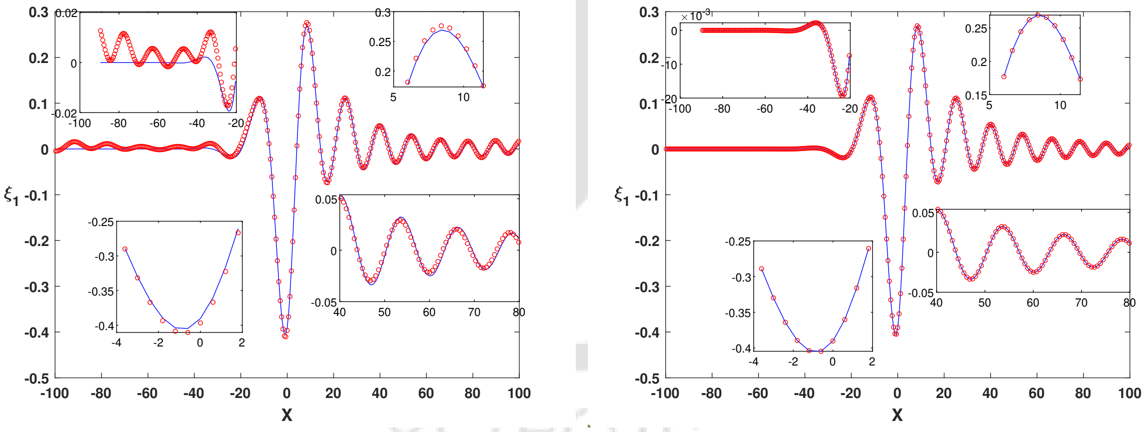

(a)

(b)

Figure 3.12: A comparison of ice deflection between various ripple numbers (n) with $b_0 = 1.5$m and a flat bottom (Solid line): (a) $n = 10$, (b) $n = 100$.

3.4 Conclusions

We propose a mathematical model for analyzing the deflection of a floating ice sheet under a moving load with the sea bottom having an undulating topography. The study demonstrates the importance of the bottom topography in determining the behavior of a floating ice sheet under a moving load. Considering the sea-bed in the form of a sinusoidal ripple bed and expressing the moving load in the form of Dirac delta function and Heaviside unit step function, the ice sheet deflection is obtained through an integral for which the asymptotic contribution associated with stationary points for various load speed regimes is obtained. The analysis and results show the interaction between the ice sheet and the sea-bed ripples with an increasing sea-bed ripple amplitude causing more disturbances in the sheet. For all results, the phenomenon of Bragg resonance is taken into account. It is observed that the deflection of the portion of the ice sheet just below the moving load shows a reduction when the amplitude of the sea-bed ripple takes larger values. Various load speeds are found to be responsible in altering the deflection of the ice sheet. The sea-bed ripples, the ice sheet, and the moving load interact dynamically, demonstrating how wave properties are influenced by the load speed, the ripple amplitude, and the ripple number. We find that the wavelength of the waves in front of the load decreases with an increasing load speed, whereas the wavelength of the waves behind the load grows. The waves with significantly longer wavelengths develop behind the load at very high speeds, creating a “shadow zone”. As the frequency of the undulation increases, the ice deflection approaches that obtained for the flat sea-bed scenario.

CHAPTER 4

Deflection of a floating ice sheet under a moving load: influence of uniform current and elastic bottom

4.1 Mathematical Formulation

We consider an infinitely long homogeneous ice sheet with thickness h and density ρ_i in the presence of a uniform current, with the sea bottom possessing elastic properties. Assuming that ρ is the constant density of water, the depth of fluid domain is considered from the ice-covered surface to the elastic bottom at $z = -H$, with the z-axis vertically upward. Additionally, the fluid is assumed to be incompressible, inviscid, and the motion irrotational, which simplifies the governing equations and allows the use of potential flow theory. The time harmonic velocity potential is denoted by $\Phi(x, z, t) = \mathrm{Re}\{\phi(x, z)e^{-\mathrm{i}\omega t}\}$. According to Davys et al. (1985), the equation governing the motion of the ice sheet is

$$D\nabla^4\xi + \rho_i h\xi_{tt} = p - f(x, t). \tag{4.1}$$

We utilize the assumption that the current flows uniformly at a constant speed u_0 in the positive x-direction, i.e., $\mathbf{U} = u_0\hat{i}$ beneath the ice sheet, with $u_0 > 0$. Therefore, during the wave motion, the perturbed velocity can be considered as $\bigoplus = \mathbf{U} + \nabla\Phi$. Thus, at $z = 0$, the pressure governed by the linearized form of the Bernoulli's equation is

$$p = -\rho(\Phi_t + \mathbf{U}.\nabla\Phi) - \rho g\xi. \tag{4.2}$$

From Eqs. (4.1) and (4.2), the dynamic equation of the ice plate gets modified by the presence of current as follows:

$$D\nabla^4\xi + \rho_i h\xi_{tt} + \rho g\xi = -\rho(\Phi_t + \mathbf{U}.\nabla\Phi) - f(x, t). \tag{4.3}$$

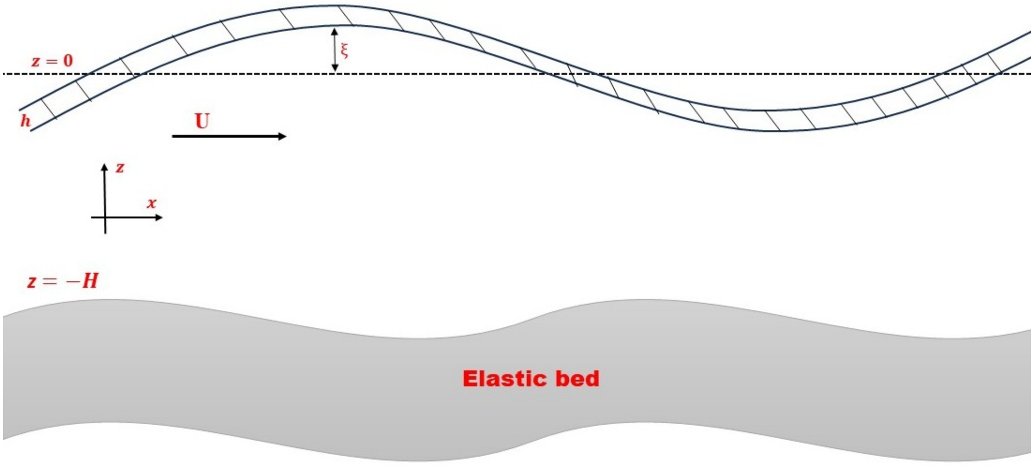

Figure 4.1: Schematic diagram of a floating ice sheet over an elastic sea-bed in the presence of current.

The velocity potential Φ satisfies the Laplace's equation and kinematic condition as follows:

$$\Phi_{xx} + \Phi_{zz} = 0, \quad -\infty < x < \infty, \; -H < z < 0, \tag{4.4}$$

$$\Phi_z = \xi_t + \mathbf{U}.\nabla\xi \quad \text{at} \quad z = 0. \tag{4.5}$$

The linearized bottom boundary condition for the elastic sea-bed is given by

$$D_1\Phi_{xxxxz} + \rho_e h_1 \Phi_{tt} + \rho g \Phi_z = \rho\Phi_{tt} \quad \text{at} \quad z = -H, \tag{4.6}$$

where $D_1 = \frac{E_1 h_1^3}{12(1-\nu^2)}$ is the flexural rigidity of the bed, E_1 is the corresponding Young's modulus and h_1 is the thickness of the elastic bed with ρ_e as the density. The elastic bottom model presented by Mohapatra and Sahoo (2011) provides the basis for the formulation of the bottom boundary condition (4.6). The deflection ξ and the velocity potential Φ vanish as the horizontal distance coordinate $x \to \pm\infty$.

We focus on the wave motion with wavelengths that are much larger than the thickness of the plates (for both the ice sheet and the elastic bed). The fluid is penetrated by the wave motion to a depth determined by the wavelength, which is associated with the hybrid waves of interest and is commonly much greater than the thickness of the plate, but may be similar to the fluid depth. Because of this, unless the waves are very short, the inertia of the flowing fluid layer is much larger compared to the inertia of the thin plate. Thus, the plate inertial term ($\rho_i h\xi_{tt}$ for the ice sheet and $\rho_e h_1 \Phi_{tt}$ for the elastic bed) can be considered negligible. Therefore, the inertial factor is not accounted for in Eqs. (4.3) and (4.6). Consequently, the governing equations get simplified to the following forms:

$$D\nabla^4\xi + \rho g\xi = -\rho(\Phi_t + \mathbf{U}.\nabla\Phi) - f(x,t) \quad \text{at} \quad z = 0, \tag{4.7}$$

$$D_1\Phi_{xxxxz} + \rho g\Phi_z = \rho\Phi_{tt} \quad \text{at} \quad z = -H. \tag{4.8}$$

Furthermore, from Eqs. (4.4), (4.5) and (4.8), we find

$$\Phi = \frac{\mathscr{A}_2}{k\mathscr{A}_1}(\xi_t + \mathbf{U}.\nabla\xi) \quad \text{at} \quad z = 0, \tag{4.9}$$

where $\mathscr{A}_1 = (D_1k^5 + \rho gk)\tanh(kH) - \rho\omega^2$, $\mathscr{A}_2 = (D_1k^5 + \rho gk) - \rho\omega^2\tanh(kH)$ and k is the wavenumber. From Eqs. (4.7) and (4.9), we subsequently have

$$D\nabla^4\xi + \rho g\xi = -\frac{\rho\mathscr{A}_2}{k\mathscr{A}_1}\left(\xi_{tt} + 2u_0\xi_{xt} + u_0^2\xi_{xx}\right) - f(x,t) \quad \text{at} \quad z = 0. \tag{4.10}$$

Dispersion Relation

We incorporate a sinusoidal wave solution $\xi = A_0e^{\mathrm{i}(kx-\omega t)}$, where A_0 is the small wave amplitude, into the homogeneous version of Eq. (4.10) in order to obtain the dispersion relation, which arises from the substitution as follows:

$$\omega_D^2 = \left(\frac{Dk^4}{\rho} + g\right)\frac{k\mathscr{A}_1}{\mathscr{A}_2}, \tag{4.11}$$

where $\omega_D = \omega - ku_0$. The formulation of the dispersion relation is validated, and the various impacts of the current and sea-bed elasticity are highlighted by the obtained dispersion relation, which shows consistency with conventional results under a variety of limiting circumstances. The simplified form of Eq. (4.11) is given by

$$q_1\omega^4 + q_2\omega^3 + q_3\omega^2 + q_4\omega + q_5 = 0, \tag{4.12}$$

where

$$\begin{aligned}
q_1 &= \tanh(kH),\\
q_2 &= -2ku_0\tanh(kH),\\
q_3 &= -\left[\left(\frac{D+D_1}{\rho}\right)k^5 + 2gk - k^2u_0^2\tanh(kH)\right],\\
q_4 &= 2ku_0\left(\frac{D_1k^5}{\rho} + gk\right),\\
q_5 &= \left(\frac{Dk^5}{\rho} + gk\right)\left(\frac{D_1k^5}{\rho} + gk\right)\tanh(kH) - k^2u_0^2\left(\frac{D_1k^5}{\rho} + gk\right).
\end{aligned}$$

A quartic (fourth-degree) polynomial in ω is represented by Eq. (4.12). To solve this polynomial equation, we refer to a number of research articles (Chávez-Pichardo et al. (2022), Chávez-Pichardo et al. (2023) and Uspensky (2005)) that extensively describe Ferrari's method. Using the theorems and analytical approaches presented in these works, we obtain

$$\omega_{1,2} = \frac{\sqrt{s_0} \pm \sqrt{q_s - 2q_6 - s_0}}{2} - \frac{q_2}{4q_1} \tag{4.13}$$

and

$$\omega_{3,4} = \frac{-\sqrt{s_0} \pm \sqrt{-q_s - 2q_7 - s_0}}{2} - \frac{q_2}{4q_1}, \tag{4.14}$$

where

$$q_6 = -\frac{k^2u_0^2\tanh(kH) + 4gk + 2\left(\frac{D_1+D}{\rho}\right)k^5}{2\tanh(kH)},$$

$$q_7 = \frac{k^6u_0}{\tanh(kH)}\left(\frac{D_1 - D}{\rho}\right),$$

$$q_8 = \frac{-4k^2u_0^2\left[\left(\frac{D+D_1}{\rho}\right)k^5 + 2gk\right] + k^4u_0^4\tanh(kH) + 16\tanh(kH)\left(\frac{Dk^5}{\rho} + gk\right)\left(\frac{D_1k^5}{\rho} + gk\right)}{16\tanh(kH)},$$

$$\beta_1 = \sqrt[3]{(q_7/2)^2 + \sqrt{(-q_7/2)^2 + ((q_6^2 - 4q_8)/3)^3}},$$

$$\beta_2 = \sqrt[3]{(q_7/2)^2 - \sqrt{(-q_7/2)^2 + ((q_6^2 - 4q_8)/3)^3}},$$

$$s_0 = \beta_1 + \beta_2, \quad \text{and} \quad q_s = -2q_7/\sqrt{s_0}.$$

If the uniform current and elastic properties of the sea-bed are not considered, the dispersion relation reverts to the classical form for the flexural-gravity waves in still water over a rigid bottom, which is given by

$$\omega^2 = \left(\frac{Dk^4}{\rho} + g\right)k\tanh(kH). \tag{4.15}$$

When there is no current and the sea-bed is elastic, the relationship depicts how the floating ice sheet interacts with the deformable sea-bed. It is provided by

$$\omega^2 = \left(\frac{Dk^4}{\rho} + g\right)\frac{k\mathscr{A}_1}{\mathscr{A}_2}. \tag{4.16}$$

The dispersion relation takes into account the Doppler-shifted frequency ω_D if the sea-bed is considered to be rigid and there is a uniform current present. This eliminates the sea-bed deformation and reflects the impact of the wave-current interaction. This is given by

$$\omega_D^2 = \left(\frac{Dk^4}{\rho} + g\right)k\tanh(kH). \tag{4.17}$$

Equation (4.17) yields the same dispersion relation as Schulkes et al. (1987) for uniform current. The phase and group speeds are, respectively, given by $c = \omega/k$ and $c_g = d\omega/dk$. The stationary condition $dc/dk = 0$ yields the smallest value of the phase speed, which is called the minimum phase speed $c_{\min}$ of the waves. This condition determines the wavenumber at which the group speed and phase speed are equal. For finding out the influence of the elastic-bed parameter D_1 on the minimum phase speed $c_{\min}$, relation (4.16) is used. The simplified form of Eq. (4.16) is

$$
\begin{aligned}
\omega^2(k^2c^2) =& \frac{\left(\frac{D_1k^5}{\rho}+\frac{Dk^5}{\rho}+2gk\right)}{2\tanh(kH)} \\
&\pm \frac{\sqrt{\left(\frac{D_1k^5}{\rho}+\frac{Dk^5}{\rho}+2gk\right)^2-4\left(\frac{D_1k^5}{\rho}+gk\right)\left(\frac{Dk^5}{\rho}+gk\right)\tanh^2(kH)}}{2\tanh(kH)}.
\end{aligned}
\tag{4.18}
$$

For waves of intermediate length, such as for $kH \gg 1$, i.e., $\tanh(kH) \approx 1$, we have

$$
c^2 = \left(\frac{Dk^3}{\rho}+\frac{g}{k}\right) \quad \text{or} \quad \left(\frac{D_1k^3}{\rho}+\frac{g}{k}\right). \tag{4.19}
$$

The minimum phase speed is

$$
c_{\min} = 2\left(\frac{Dg^3}{27\rho}\right)^{1/8} \quad \text{at} \quad k=\left(\frac{\rho g}{3D}\right)^{1/4} \quad \text{or} \quad 2\left(\frac{D_1g^3}{27\rho}\right)^{1/8} \quad \text{at} \quad k=\left(\frac{\rho g}{3D_1}\right)^{1/4}. \tag{4.20}
$$

The minimum phase speed $c_{\min}$ of the wave depends on both the elastic-bed parameter D_1 and the ice sheet parameter D.

4.2 Method of Solution

We first define the loading function before proceeding to solve Eq. (4.10). We address a concentrated line load moving in the positive x-direction at a constant speed V. In this case, the loading function gives the external forcing term $f(x,t) = F_0\delta(x-Vt)u(t)$. Here, F_0 denotes the magnitude of the force applied perpendicular to the ice surface of a load per unit area, $\delta(.)$ is the Dirac delta function, and $u(t)$ is the Heaviside unit step function, ensuring that the load acts exclusively for $t > 0$.

We use the Fourier transform approach to calculate the ice-plate deflection. Fourier transform is applied to Eq. (4.10) with respect to x. Thus, it provides us the transformed equation as follows:

$$
Dk^4\hat{\xi} + \frac{\rho\mathscr{A}_2}{k\mathscr{A}_1}\left[\frac{d^2\hat{\xi}}{dt^2} - k^2u_0^2\hat{\xi} + 2\mathrm{i}ku_0\frac{d\hat{\xi}}{dt}\right] + \rho g\hat{\xi} = -\frac{F_0}{\sqrt{2\pi}}e^{-\mathrm{i}kVt}, \tag{4.21}
$$

where the Fourier transform of $\xi(x,t)$ with respect to x is

$$
\mathscr{F}\{\xi(x,t)\} = \hat{\xi}(k,t) = \frac{1}{\sqrt{2\pi}}\int_{-\infty}^{\infty}\xi(x,t)e^{-\mathrm{i}kx}dx.
$$

The simplified form of Eq. (4.21) is

$$
\frac{d^2\hat{\xi}}{dt^2} + 2\mathrm{i}ku_0\frac{d\hat{\xi}}{dt} + \left[\left(\frac{Dk^4}{\rho}+g\right)\frac{k\mathscr{A}_1}{\mathscr{A}_2} - k^2u_0^2\right]\hat{\xi} = -\frac{k\mathscr{A}_1F_0}{\sqrt{2\pi}\rho\mathscr{A}_2}e^{-\mathrm{i}kVt}. \tag{4.22}
$$

We use the standard methods for linear ODEs to solve Eq. (4.22). The general solution of Eq. (4.22) is as follows:

$$\hat{\xi}(k,t) = A_1 e^{\mathrm{i}(\omega_D - ku_0)t} + A_2 e^{-\mathrm{i}(\omega_D + ku_0)t} - \frac{kF_0\mathscr{A}_1}{\sqrt{2\pi}\rho\mathscr{A}_2}\left(\frac{e^{-\mathrm{i}kVt}}{\omega_D^2 - k^2(u_0 - V)^2}\right). \tag{4.23}$$

The initial conditions ($\hat{\xi}(k,0) = 0$ and $\hat{\xi}_t(k,0) = 0$) are used to determine the arbitrary constants A_1 and A_2. Application of these conditions gives the final form of the solution of Eq. (4.22) as

$$\hat{\xi}(k,t) = \frac{k\mathscr{A}_1 F_0}{2\sqrt{2\pi}\rho\mathscr{A}_2\omega_D}\left[\frac{1}{\Psi_1}\left(e^{-\mathrm{i}\Psi_1 t} - 1\right) + \frac{1}{\Psi_2}\left(e^{\mathrm{i}\Psi_2 t} - 1\right)\right]e^{-\mathrm{i}kVt}, \tag{4.24}$$

where $\Psi_1 = \omega_D + k(u_0 - V)$ and $\Psi_2 = \omega_D - k(u_0 - V)$. To evaluate $\xi(x,t)$, we apply inverse Fourier transform to $\hat{\xi}(k,t)$. The inverse Fourier transform is provided by

$$\mathscr{F}^{-1}\{\hat{\xi}(k,t)\} = \xi(x,t) = \frac{1}{\sqrt{2\pi}}\int_{-\infty}^{\infty}\hat{\xi}(k,t)e^{\mathrm{i}kx}dk.$$

Substituting the expression of $\hat{\xi}(k,t)$ into the inverse Fourier transform formula yields the expression

$$\xi(x,t) = \frac{F_0}{4\pi\rho}\int_{-\infty}^{\infty}\frac{k\mathscr{A}_1}{\omega_D\mathscr{A}_2}\left[\frac{1}{\Psi_1}\left(e^{-\mathrm{i}\Psi_1 t} - 1\right) + \frac{1}{\Psi_2}\left(e^{\mathrm{i}\Psi_2 t} - 1\right)\right]e^{\mathrm{i}(kx - kVt)}dk. \tag{4.25}$$

Defining $X = x - Vt$, a new coordinate system that moves with the load is introduced. The ice-plate deflection in this moving coordinate system is represented as follows:

$$\xi(X) = \frac{F_0}{4\pi\rho}\left(I_1 + I_2 + I_3\right), \tag{4.26}$$

where

$$I_1 = -\int_{-\infty}^{\infty}\frac{2k\mathscr{A}_1}{\mathscr{A}_2\Psi_1\Psi_2}e^{\mathrm{i}kX}dk, \tag{4.27}$$

$$I_2 = \int_{-\infty}^{\infty}\frac{k\mathscr{A}_1}{\omega_D\mathscr{A}_2\Psi_1}e^{\mathrm{i}(kX - \Psi_1 t)}dk, \tag{4.28}$$

$$I_3 = \int_{-\infty}^{\infty}\frac{k\mathscr{A}_1}{\omega_D\mathscr{A}_2\Psi_2}e^{\mathrm{i}(kX + \Psi_2 t)}dk. \tag{4.29}$$

The ice deflection ξ must satisfy the outgoing radiation (Sommerfeld-type) condition $\lim_{|X|\to\infty}\left(\frac{d\xi}{dX} - \mathrm{i}k\,\mathrm{sgn}(X)\xi\right) = 0$, where "sgn$(X)$" is the sign function indicating the direction of outgoing waves. This condition physically enforces that the deflection field represents only outgoing waves propagating away from the moving load. Non-dimensional quantities are defined for convenience and to make the mathematical expressions simpler. These are described as follows:

$$\tilde{X} = \frac{X}{H}, \quad \tilde{k} = kH, \quad \tilde{V} = \frac{V}{\sqrt{gH}}, \quad \tilde{u}_0 = \frac{u_0}{\sqrt{gH}}, \quad \tilde{D} = \frac{D}{\rho g H^4}, \quad \tilde{D}_1 = \frac{D_1}{\rho g H^4},$$

$$\tilde{\xi}=\frac{\xi}{H},\quad \tilde{c}=\frac{c}{\sqrt{gH}},\quad \tilde{\omega}=\omega\sqrt{\frac{H}{g}},\quad \tilde{\omega}_D=\omega_D\sqrt{\frac{H}{g}},\quad \tilde{t}=t\sqrt{\frac{g}{H}},\quad \tilde{F}_0=\frac{F_0}{\rho g H}.$$

In the non-dimension form, the expressions of the notations become

$$\tilde{\mathscr{A}}_1=(\tilde{D}_1\tilde{k}^4+1)\tilde{k}\tanh(\tilde{k})-\tilde{\omega}^2,\quad \tilde{\mathscr{A}}_2=(\tilde{D}_1\tilde{k}^4+1)\tilde{k}-\tilde{\omega}^2\tanh(\tilde{k}),$$
$$\tilde{\Psi}_1=\tilde{\omega}_D+\tilde{k}(\tilde{u}_0-\tilde{V}),\quad \tilde{\Psi}_2=\tilde{\omega}_D-\tilde{k}(\tilde{u}_0-\tilde{V}),\quad \tilde{\omega}_D^2=(\tilde{D}\tilde{k}^4+1)\tilde{k}\frac{\tilde{\mathscr{A}}_1}{\tilde{\mathscr{A}}_2}.$$

The non-dimensional form of the expression for ξ is as follows:

$$\tilde{\xi}=\frac{\tilde{F}_0}{4\pi}(\tilde{I}_1+\tilde{I}_2+\tilde{I}_3), \tag{4.30}$$

where

$$\tilde{I}_1=-\int_{-\infty}^{\infty}\frac{2\tilde{k}\tilde{\mathscr{A}}_1}{\tilde{\mathscr{A}}_2\tilde{\Psi}_1\tilde{\Psi}_2}e^{\mathrm{i}\tilde{k}\tilde{X}}d\tilde{k}, \tag{4.31}$$
$$\tilde{I}_2=\int_{-\infty}^{\infty}\frac{\tilde{k}\tilde{\mathscr{A}}_1}{\tilde{\omega}_D\tilde{\mathscr{A}}_2\tilde{\Psi}_1}e^{\mathrm{i}(\tilde{k}\tilde{X}-\tilde{\Psi}_1 t)}d\tilde{k}, \tag{4.32}$$
$$\tilde{I}_3=\int_{-\infty}^{\infty}\frac{\tilde{k}\tilde{\mathscr{A}}_1}{\tilde{\omega}_D\tilde{\mathscr{A}}_2\tilde{\Psi}_2}e^{\mathrm{i}(\tilde{k}\tilde{X}+\tilde{\Psi}_2\tilde{t})}d\tilde{k}. \tag{4.33}$$

Beyond this point, for simplicity, the notations are going to be used without the tilde. It is noticeable from Eqs. (4.31)-(4.33) that integral I_1 is time-independent, while the integrals I_2 and I_3 are time-dependent. We denote the integrands of the integrals by $N_i,\ i=1,2,3$. Using the stationary phase method approach, the expression for ξ is analytically investigated.

The stationary phase approach is going to be used to study the plate deflection behavior for long time-frames. For this reason, the behavior of the integrals will be investigated at the stationary points, since these regions make the dominant contribution to the solution at large times. Importantly, the function Ψ_2 has no stationary points because it is strictly increasing, which means that it never vanishes. As such, the integral I_3 decays exponentially as $t\to\infty$. Because of its rapid exponential decay, the transition to the steady state approaches very quickly. Therefore, the contribution from I_3 can be ignored in the calculations, and we only take into account those terms that decay algebraically with time. The zeros and the stationary points related to Ψ_1 both impact the behavior of the integrals. **Appendix A** provides a detailed explanation of these zeros and stationary points. Let k_y and k_z represent the zeros, and k_a and k_b represent the stationary points of Ψ_1. We use a solution approach that is comparable to the kind used by Schulkes and Sneyd (1988) in their analyses.

The deflection response that corresponds to numerous phase function Ψ_1 characteristics that are influenced by variations in load speed V is methodically represented by the asymptotic analysis. In order to show the impact of the dynamic variables on the ice-plate displacement, the solution is categorized and examined under various load velocity regimes.

Case 1:- $\mathbf{V} \leq \mathbf{c_{gmin}}$ (Subcritical Source speed)
The integrands N_1 and N_2 are analytic in the vicinity of the real axis of k in this case. As a consequence, the Riemann-Lebesgue lemma implies that the integral I_2 tends to zero as $t \to \infty$. Therefore, the plate deflection can be expressed in the following form:

$$\xi_s = -\frac{F_0}{4\pi} I_1, \tag{4.34}$$

with ξ_s denoting the steady part of the solution. A Fast Fourier Transform (FFT) or some numerical integration technique can be used to numerically calculate the value of ξ_s.

Case 1a:- $\mathbf{V} < \mathbf{c_{gmin}}$
The ice deflection behavior is similar to the response of a stationary load when the load moves at very low speed, i.e., below the minimum group speed of the waves. This happens because the phase function in this particular scenario does not have any stationary points and zeros. Consequently, the integral I_1 decays exponentially with time, resulting in a deflection response similar to a stationary load.

Case 1b:- $\mathbf{V} = \mathbf{c_{gmin}}$
When the load speed equals the minimum group speed, the phase function has an inflection point, denoted by k_a, i.e., $\Psi_1''(k_a) = 0$ and $\Psi_1'''(k_a) \neq 0$. Using **Result 1** of Chapter 1 (pages 12–13), the deflection can be expressed in the following form:

$$\xi = \xi_s + \frac{\Gamma(1/3)}{12\pi} \frac{k_a \mathcal{A}_{1a} F_0}{\omega_{Da} \mathcal{A}_{2a} \Psi_{1a}} \left(\frac{3!}{|\Psi_{1a}'''|} \right)^{1/3} \cos(k_a X - t\Psi_{1a} + \pi/6) t^{-1/3}. \tag{4.35}$$

For this case, the deflection decays algebraically with time as $t^{-1/3}$.

Case 2:- $\mathbf{c_{gmin}} < \mathbf{V} < \mathbf{c_{min}}$
For this case, the phase function $\Psi_1(k)$ has two distinct stationary points, i.e., $\Psi_1'(k_a) = \Psi_1'(k_b) = 0$. Using **Result 1** of Chapter 1 (pages 12–13), the deflection can be expressed in the following form:

$$\begin{aligned} \xi = &\xi_s + \frac{F_0}{4\pi} \left[\frac{k_a \mathcal{A}_{1a}}{\omega_{Da} \mathcal{A}_{2a} \Psi_{1a}} \sqrt{\frac{2}{\Psi_{1a}''}} \cos(k_a X - t\Psi_{1a} + \pi/4) \right. \\ &\left. + \frac{k_b \mathcal{A}_{1b}}{\omega_{Db} \mathcal{A}_{2b} \Psi_{1b}} \sqrt{\frac{2}{\Psi_{1b}''}} \cos(k_b X - t\Psi_{1b} - \pi/4) \right] t^{-1/2}. \end{aligned} \tag{4.36}$$

For this case, the deflection decays algebraically with time as $t^{-1/2}$.

Case 3:- $\mathbf{c_{min} < V < \sqrt{gH}}$ (Supercritical source speed)
When the load moves with a supercritical speed, that is, $V > c_{\min}$, the phase function Ψ_1 has two different zeros (k_y and k_z), along with two stationary points (k_a and k_b). To evaluate the integrals asymptotically in this regime, the method of steepest descents is used. The integrand remains analytic around the zeros, transforming the integration contour from the real k-axis into the complex k-plane. Along this modified path, the oscillatory exponential term $e^{\mathrm{i}\Psi_1 t}$ exhibits rapid exponential decay, optimizing the convergence of the integral. However, near k_a and k_b, such contour deformation is not possible. Therefore, a straight line path with the steepest descent that passes through k_a and k_b must connect the disjoint curves of the deformed contour. This method is consistent with the approaches described by Lighthill (2001) and Schulkes and Sneyd (1988). Therefore, we may write

$$\xi = \frac{F_0}{4\pi}[I_{1C} + I_{2C}]. \tag{4.37}$$

The integrals in Eqs. (4.31) and (4.32) maintain their original definitions, but the direction of integration is altered by replacing a contour in the complex k-plane with the real k-axis.

When the load speed reaches the minimum phase speed, wave generation occurs, resulting in two distinct waves: one propagating ahead of the load and the other trailing behind it. Here, $X > 0$ corresponds to the region in front of the load (leading wave), while $X < 0$ represents the region behind the load (trailing wave). For $X > 0$, the contour of integration is closed in the upper half of the complex plane using a semicircular arc. By Jordan's lemma, the contribution from the arc vanishes. Similarly, for $X < 0$, the contribution of the arc vanishes for the contour in the lower half plane. Therefore, by the Residue Theorem, the integral gives

$$\xi_s = \begin{cases} \frac{F_0\mathscr{A}_{1z}}{\mathscr{A}_{2z}(V-u_0)(c_{gz}-V)}\sin(k_z X) + \mathrm{Res}(X), & X > 0, \\ \\ \frac{F_0\mathscr{A}_{1y}}{\mathscr{A}_{2y}(V-u_0)(V-c_{gy})}\sin(k_y X) + \mathrm{Res}(-X), & X < 0. \end{cases} \tag{4.38}$$

Here, $\mathrm{Res}(X) = \{\pm \mathrm{i}s_n;\ n\pi < s_n < (n+1)\pi\}$ represents the small contribution arising from the purely imaginary poles. These are negligible everywhere except quite close to the load at the origin, i.e., these poles influence ξ_s through the first few terms, mainly near the location of the load. Due to the discontinuity at the origin, and following the approach of Schulkes and Sneyd (1988) and Squire et al. (1996), the term $\mathrm{Res}(X)$ is neglected in the numerical computations. This approximation still retains the dominant wave behavior and deflection characteristics away from the load while avoiding numerical artifacts associated with the singularity (Hosking et al. (1988)). The transient response is primarily governed by the real poles, which are related to the load speed, and by the stationary points. Among these, the contributions from the real poles associated with the load speed are the most significant.

The contributions from the stationary points are evaluated using **Result 1** of Chapter 1 (pages 12–13), and thus, the final expression for ξ is obtained as

$$\xi = \begin{cases} \frac{F_0 \mathcal{A}_{1z}}{\mathcal{A}_{2z}(V-u_0)(c_{gz}-V)} \sin(k_z X) + \frac{F_0}{4\pi} \left[\frac{k_a \mathcal{A}_{1a}}{\omega_{Da} \mathcal{A}_{2a} \Psi_{1a}} \sqrt{\frac{2}{\Psi''_{1a}}} \cos(k_a X - t\Psi_{1a} + \pi/4) \right. \\ \left. + \frac{k_b \mathcal{A}_{1b}}{\omega_{Db} \mathcal{A}_{2b} \Psi_{1b}} \sqrt{\frac{2}{\Psi''_{1b}}} \cos(k_b X - t\Psi_{1b} - \pi/4) \right] t^{-1/2} + \mathrm{Res}(X), \quad X > 0, \\ \\ \frac{F_0 \mathcal{A}_{1y}}{\mathcal{A}_{2y}(V-u_0)(V-c_{gy})} \sin(k_y X) + \frac{F_0}{4\pi} \left[\frac{k_a \mathcal{A}_{1a}}{\omega_{Da} \mathcal{A}_{2a} \Psi_{1a}} \sqrt{\frac{2}{\Psi''_{1a}}} \cos(k_a X - t\Psi_{1a} + \pi/4) \right. \\ \left. + \frac{k_b \mathcal{A}_{1b}}{\omega_{Db} \mathcal{A}_{2b} \Psi_{1b}} \sqrt{\frac{2}{\Psi''_{1b}}} \cos(k_b X - t\Psi_{1b} - \pi/4) \right] t^{-1/2} + \mathrm{Res}(-X), \quad X < 0. \end{cases} \tag{4.39}$$

In the supercritical speed case, the deflection decays algebraically with time as $t^{-1/2}$.

Case 4:- $V > \sqrt{\mathbf{gH}}$

In this case, the phase function $\Psi_1(k)$ has a single zero k_z and a stationary point k_b. Thus, by substituting $k_y = k_a = 0$ in Eq. (4.39), one may obtain ξ.

Case 5:- $\mathbf{V = c_{min}}$

A second-order zero occurs when $V = c_{\min}$ because the stationary points and zeros of $\Psi_1(k)$ coincide at a single point k_m(say), i.e., $\Psi_1(k_m) = \Psi_1'(k_m) = 0$. Therefore, we have

$$\xi_s = \begin{cases} \mathrm{Res}(X), \quad X > 0, \\ \\ -\frac{F_0}{V-u_0}[X\mu_m \cos(k_m X) + \mu'_m \sin(k_m X)] + \mathrm{Res}(-X), \quad X < 0, \end{cases} \tag{4.40}$$

where $\mu = \lim\limits_{k \to k_m} \mu(k) = \lim\limits_{k \to k_m} \dfrac{(k-k_m)^2 \mathcal{A}_1}{\Psi_1 \mathcal{A}_2}$. The integrand N_2 is exponentially smaller on the contour C. In addition to the straight-line segments P_3P_4 and P_5P_6, there are two indented paths P_1P_2 and P_7P_8 (see Fig. 4.2(a)). By rotating the contour with the substitution $k = k_m - \mathrm{i}z$, we compute the contribution from P_1P_2. This substitution yields the following expression:

$$\begin{aligned} \int_{P_1P_2} N_2 dk &= \mathrm{i} \int_{C'} \left(\frac{k_m - \mathrm{i}z}{\omega_D(k_m - \mathrm{i}z)} \right) \mu(k_m - \mathrm{i}z) e^{\mathrm{i}(k_m - \mathrm{i}z)X} \left(\frac{e^{\mathrm{i}z^2\tau}}{z^2} \right) d\tau + \mathcal{O}(e^{-at}) \\ &= \mathrm{i} \int_{C'} \left(\frac{\mu(k_m - \mathrm{i}z)}{c(k_m - \mathrm{i}z) - u_0} \right) e^{\mathrm{i}(k_m - \mathrm{i}z)X} \left(\frac{e^{\mathrm{i}z^2\tau}}{z^2} \right) d\tau + \mathcal{O}(e^{-at}), \end{aligned} \tag{4.41}$$

where $2\tau = \Psi''_{1m} t$ and $a \in \mathbb{R}^+$. With the help of Schulkes and Sneyd (1988), we find the solution to Eq. (4.41). Therefore, we have

$$\int_{P_1P_2} N_2 dk = \frac{e^{\mathrm{i}k_m X}}{V - u_0} \left[-\mathrm{i}\mu_m \sqrt{2\pi \Psi''_{1m} t} e^{-\mathrm{i}\pi/4} + \pi(X\mu_m - \mathrm{i}\mu'_m) \right] + \mathcal{O}(t^{-1/2}). \tag{4.42}$$

In a similar manner, we determine the other contribution of the indented path P_7P_8 and then combine them to get

$$\int_{P_1P_2+P_7P_8} N_2 dk = -\,2\mu_m\sqrt{2\pi\Psi''_{1m}t}\,\frac{\sin(k_mX+\pi/4)}{V-u_0} + \pi X\mu_m\frac{\cos(k_mX)}{V-u_0} + \pi\mu'_m\frac{\sin(k_mX)}{V-u_0} + \mathcal{O}(t^{-1/2}). \tag{4.43}$$

We combine Eqs. (4.40) and (4.43) to get

$$\xi = \frac{F_0}{4(V-u_0)}\left[2t^{1/2}\mu_m\sqrt{2\pi\Psi''_{1m}}\sin(k_m|X|+\pi/4) + 3|X|\cos(k_m|X|)\; + 3\mu'_m\sin(k_m|X|)\right] + \mathrm{Res}(|X|) + \mathcal{O}(t^{-1/2}). \tag{4.44}$$

In this speed regime, the deflection grows algebraically with time $t^{1/2}$. The term $\mathcal{O}(t^{-1/2})$ in the expression represents the contribution from the stationary points.

Case 6:- $\mathbf{V = \sqrt{gH}}$

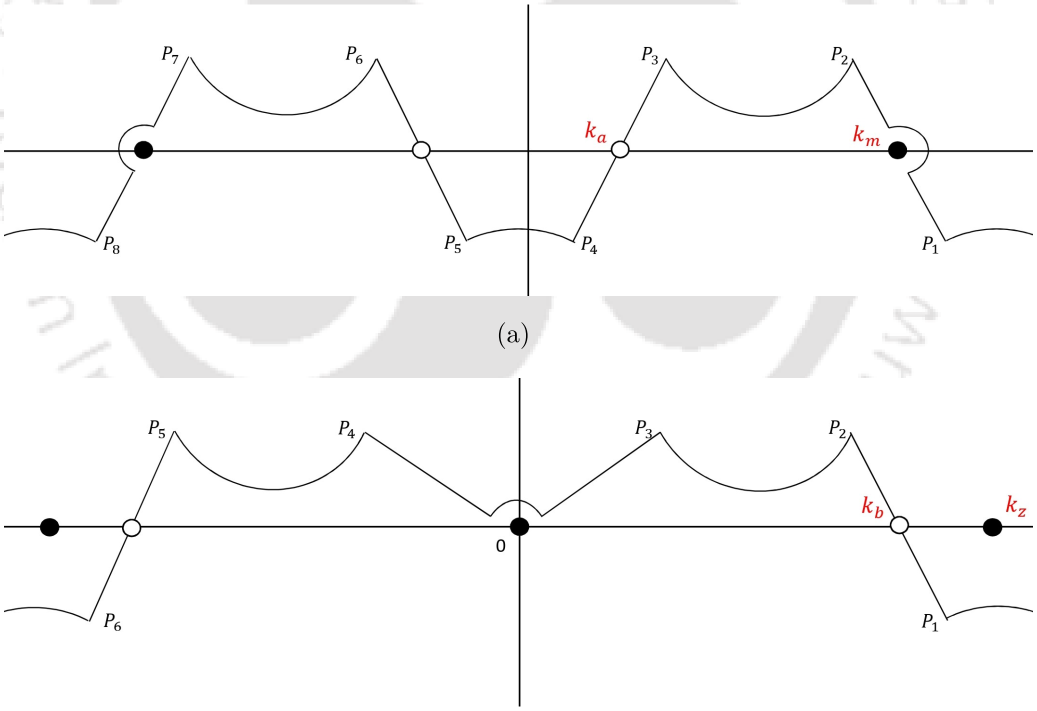

(a)

(b)

Figure 4.2: Integration contours for different cases: (a) $V = c_{\min}$, (b) $V = \sqrt{gH}$. Open circles represent stationary points, and solid circles represent zeros of Ψ_1.

In our non-dimensional formulation, we chose $\sqrt{gH}$ as the characteristic speed scale. In the particular case where the load speed V is equal to the gravity wave speed $\sqrt{gH}$, the non-dimensional load speed becomes $V = 1$.

For this case, the phase function has a triple zero at the origin since both the points k_a and k_y merge there. As a result, the contour C is deformed with an indentation around the origin (Fig. 4.2(b)). Other than those, it has one zero k_z and one stationary point k_b. The contribution of the zeros is given by the Residue Theorem as follows:

$$\xi = \begin{cases} \frac{F_0\mathscr{A}_{1z}}{\mathscr{A}_{2z}(V-u_0)(c_{gz}-V)}\sin(k_zX) + \text{Res}(X), & X > 0, \\ \\ \frac{3\mathrm{i}F_0\alpha_0}{2V(V-u_0)} + \text{Res}(-X), & X < 0, \end{cases} \tag{4.45}$$

where

$$\alpha_0 = \lim_{k\to 0}\alpha(k) = \lim_{k\to 0}\frac{d^2}{dk^2}\left(\frac{\mathscr{A}_1}{\mathscr{A}_2}e^{\mathrm{i}kX}\right).$$

The contribution of the indented path P_3P_4 gives

$$\frac{F_0}{4\pi}\int_{P_3P_4} N_2(k)dk = \frac{3F_0(1+V^2)}{2\pi V(V-u_0)}\left[\sqrt{3}\Gamma(2/3)6^{-1/3}t^{1/3} + \frac{2\mathrm{i}\pi X}{3}\right]. \tag{4.46}$$

Therefore, the final expression of ξ is

$$\xi = \begin{cases} \frac{F_0\mathscr{A}_{1z}}{\mathscr{A}_{2z}(V-u_0)(c_{gz}-V)}\sin(k_zX) + \frac{3F_0(1+V^2)}{2\pi V(V-u_0)} \\ \times\left[\sqrt{3}\Gamma(2/3)6^{-1/3}t^{1/3} + \frac{2\mathrm{i}\pi X}{3}\right] + \text{Res}(X), \quad X > 0, \\ \\ \frac{3\mathrm{i}F_0\alpha_0}{2V(V-u_0)} + \frac{3F_0(1+V^2)}{2\pi V(V-u_0)} \\ \times\left[\sqrt{3}\Gamma(2/3)6^{-1/3}t^{1/3} + \frac{2\mathrm{i}\pi X}{3}\right] + \text{Res}(-X), \quad X < 0. \end{cases} \tag{4.47}$$

The displacement grows without bound as $t \to \infty$ due to $V = c = c_g$. However, in this case, the wavelength corresponding to this triple equality becomes a limiting value, i.e., $2\pi/k \to \infty$ as $k \to 0$, indicating that the singularity is comparatively weaker. This results in a more gradual growth of the deflection over time as $t^{1/3}$.

Since our work may look similar to some other recent works, we deem it suitable to present some comparisons to highlight the differences. The hydro-elastic response of floating ice sheets over a rigid sea-bed in the presence of currents has been the subject of numerous research in the literature. While these works provide useful insights, their formulations differ from the current model in several ways, including the representation of the external loading function, the inclusion of uniform or shear currents, the consideration of elastic or viscoelastic ice sheets, and the analytical methods used.

The recent study by Boral and Ni (2025) considered a Kelvin-Voigt viscoelastic plate model incorporating internal damping, by including the effect of a lateral compressive force in the governing equations, and accounted for the presence of a uniform current. They considered time-harmonic forcing instead of a concentrated moving line load, with the main focus on damping effects and the occurrence of blocking points. In contrast, our study primarily emphasizes the interaction between the phase/group speeds of waves and the speed of the moving load.

The present study differs in several important aspects from the study of Tkacheva (2023), while at the same time retaining comparable physical foundations. The most immediate distinction lies in the representation of the applied load. While Tkacheva considered a finite rectangular pressure patch, we consider a moving load. Furthermore, the present model is developed for the case of a uniform current, which allows the perturbation field to remain irrotational and leads to a classical flexural-gravity dispersion relation modified only by a Doppler shift. In contrast, Tkacheva (2023) investigated a shear current with depth-dependent velocity, producing rotational perturbations and a substantially more intricate dispersion structure. This distinction has a strong influence on the analytical approach. In the simpler manner of a uniform current, this threshold depends only on the classical dispersion relation, while in the shear-current environment considered by Tkacheva, it is additionally shaped by the shear parameter, the direction of load motion, and the degree of in-plane compression of the ice.

4.3 Numerical Results

We define the parameter values before discussing numerical outcomes. It should be noted that since we describe the parameters in their dimensional form, we will use their corresponding expressions to compute their non-dimensional values because our problem is in non-dimensional form. For the physical parameters, the following values are considered (Davys et al. (1985)): $E = 5\times10^9\text{Nm}^{-2}$, $h = 2.5\text{m}$, $H = 350\text{m}$, $\nu = 1/3$, $\rho = 1000\text{kg/m}^3$, $\rho_i = 947\text{kg/m}^3$ and $g = 9.8\text{m/s}^2$. Similarly, the minimum phase speed $c_{\min} \approx 22.5\text{m/s}$ and gravity wave speed $\sqrt{gH} = 58.6\text{m/s}$ are also taken from Davys et al. (1985) for the case without elastic bottom and current. The impact of ice sheet characteristics on wave propagation has been examined in prior studies (Squire et al. (1996)). We concentrate on establishing the effects of the changes due to the bottom boundary conditions, i.e., the consideration of an elastic sea-bed and in the presence of a uniform current. These components may have a significant effect on the wave dynamics and ice sheet deflection patterns.

Since the present model does not incorporate any form of dissipation, the observed attenuation-like behavior arises from purely dispersive effects, rather than the energy loss. In the absence of dissipation, energy created by the moving load cannot be drained or absorbed, so it accumulates continuously underneath the load. This accumulation persists steadily when the load moves at a constant speed, leading to an expected linear growth of energy in the vicinity of the load over time. The ice sheet deflection figures are presented for the time instants $t = 5,\ 10$.

Variations in the elastic modulus E_1 (and thus flexural rigidity D_1) of the sea-bed significantly influence wave dispersion characteristics, energy transmission, and the mechanical load transfer between ice and sea-bed. Selecting $D_1(\gg D)$ in representative scenarios allows modeling of a sea-bed that acts as a strong mechanical support for the ice sheet. A stiffer bed (higher D_1) limits ice curvature and reduces bending amplitudes under loading, decreasing fracture risk, while a compliant bed (lower D_1) encourages larger deflections and greater local energy dissipation. We deliberately consider the limiting case in which the sea-bed behaves as a supporting foundation, as opposed to a compliant, energy-absorbing layer. For this purpose, dimensionless values of D_1 are selected such that they are greater than D values. This study examines the changes in the bottom elasticity using sample dimensionless values of flexural rigidity $D_1 = 0,\ 0.025,\ 0.050$ and 0.075, and considering $h_1 \leq h$. To account for the uniform current, we analyze the scenarios with dimensionless values of $u_0 = 0,\ 0.10,\ 0.20$ and 0.30. We take up four possible scenarios listed below:

- **Scenario 1:** A rigid bottom case without the effects of uniform current and bottom elasticity.
- **Scenario 2:** A uniform current is present but a rigid bottom is assumed; no bottom elasticity is taken into account.
- **Scenario 3:** Instead of a rigid bottom, an elastic bottom is considered without the presence of a uniform current.
- **Scenario 4:** Both uniform current and bottom elasticity are considered.

We discuss the outcomes of these four scenarios related to the phase speed, group speed, and ice sheet deflection. The axes of the figures are presented in non-dimensional forms, and all parameter values are used in non-dimensional form. The ice sheet deflection ξ plots are presented against $X = x - Vt$, where the load position corresponds to $X = 0$.

4.3.1 Validation

To validate our problem, we compare our results with an existing study (Schulkes and Sneyd (1988)). For this validation, we consider that the effect of uniform current is neglected, and instead of an elastic bed, a rigid bed is taken into account. First, the corresponding equation of deflection from the existing study (Schulkes and Sneyd (1988)) is converted into its non-dimensional form, after which the comparison is carried out. This comparison is illustrated in Fig. 4.3, where the ice deflection for non-dimensional load speed $V = 0.51$ at the instant $t = 10$ is plotted. The considerable match evident in this comparison demonstrates the efficacy of the current model and subsequently gives assurance to continue with the model.

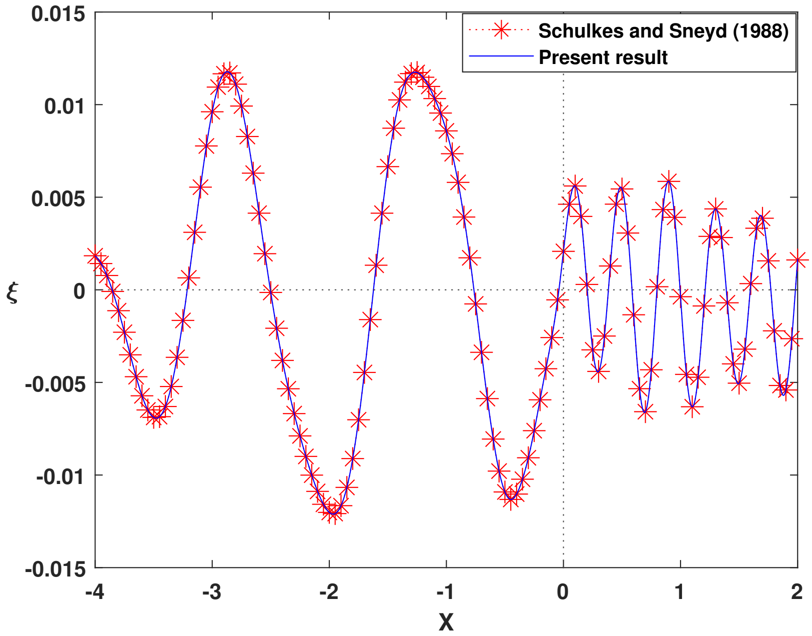

Figure 4.3: Deflection of the ice sheet (ξ) versus X for the non-dimensional load speed $V = 0.51$ at $t = 10$.

4.3.2 Dispersion Relation and Related Issues

We utilize Eq. (4.15) for Scenario 1 (S1), Eq. (4.17) for Scenario 2 (S2), Eq. (4.16) for Scenario 3 (S3), and Eq. (4.11) for Scenario 4 (S4) in order to represent the phase and group speeds graphs. The wave propagation in the positive x-direction is taken into account in our analysis.

The phase and group speeds for the scenario with a rigid bottom and no current are plotted in Fig. 4.4, which corresponds to Eq. (4.15). The phase speed and group speed exhibit a similar behavior, both approaching their minimum values ($c_{\min}$ and $c_{g\min}$) for the intermediate range of wavelengths of waves. For long waves (i.e., $k \to 0$), both phase speed and group speed approach the speed of the gravity waves.

For the scenario with a rigid bottom and a uniform current, we plot the phase and group speeds in Fig. 4.5, which is based on the Doppler-shifted frequency defined by Eq. (4.17), which takes into consideration the effect of the uniform current on the wave propagation. This changes the basic wave frequency, which influences both the phase and group speeds.

Figure 4.6(a) depicts that phase speed c varies with wavenumber k for various values of bottom elasticity parameter D_1, assuming no current is involved. The minimum value of the phase speed $c_{\min}$ increases in conjunction with an increase in D_1. For a certain value of D_1, this phenomenon is noticeable. Moreover, it is noted that, as D_1 increases, the phase speed curves shrink toward smaller wavenumber k in comparison to the rigid bottom case, when the curves extend for greater values of k. The variation in the group speed with bottom elasticity parameter D_1 is shown in Fig. 4.6(b). The group speed rapidly increases with wavenumber for $D_1 > 0$.

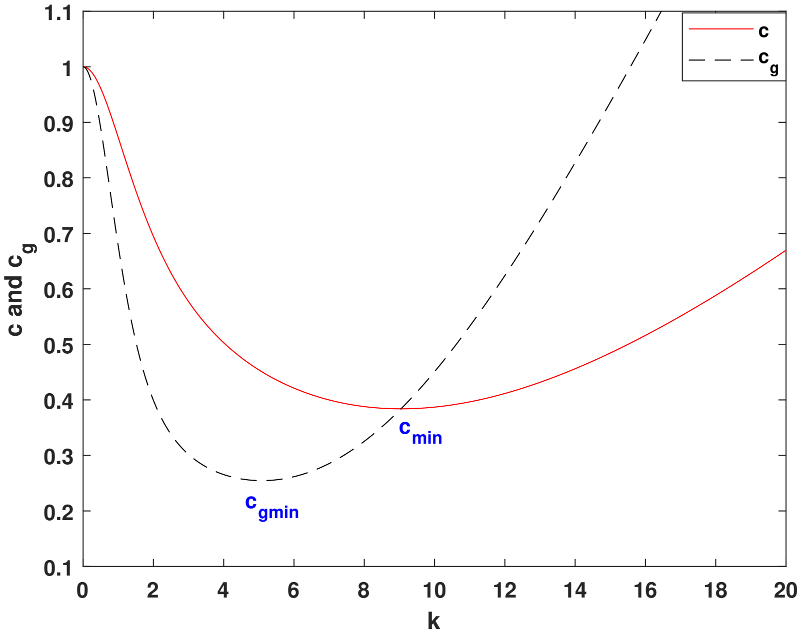

Figure 4.4: Variation of phase and group speeds against wavenumber k for the case of a rigid bottom in the absence of both uniform current and elastic sea-bed (Scenario 1): Solid line (—) represents phase speed c, and dashed line (- -) represents group speed c_{g}.

The curves demonstrate a significant increment in c_g with k, and this effect continues as D_1 increases. We notice that the wave energy spreads more quickly as D_1 increases. An elastic sea-bed with higher flexural rigidity supports faster and more effective energy transportation across the wave spectrum since higher values of D_1 correspond to higher group speeds for a given wavenumber. The flexural rigidity not only changes the phase speed, but it also additionally significantly enhances the transfer of energy (as shown in the group speed behavior). Additionally, the group speed increases rapidly for shorter wavelength, indicating that the shorter waves are more influenced by variations in D_1.

Figure 4.7 demonstrates the behavior of phase speed c against wavenumber k for various circumstances. Figure 4.7(a) shows that changing the flexural rigidity D_1 affects the phase speed while keeping the uniform current speed u_0 constant. Three distinct values of D_1 $(0.025, 0.050$ and $0.075)$ are taken into account. Across the wavenumber range, it is found that an increase in the flexural stiffness makes the phase speed increase in general. The phase speed curves show normal dispersive behavior, with an intermediate wavelength displaying the minimum phase speed. With a fixed value of flexural rigidity D_1, Fig. 4.7(b) illustrates that the variation in uniform current speed u_0 affects the phase speed. Three values of u_0 $(0.10, 0.20$ and $0.30)$ are taken into consideration.

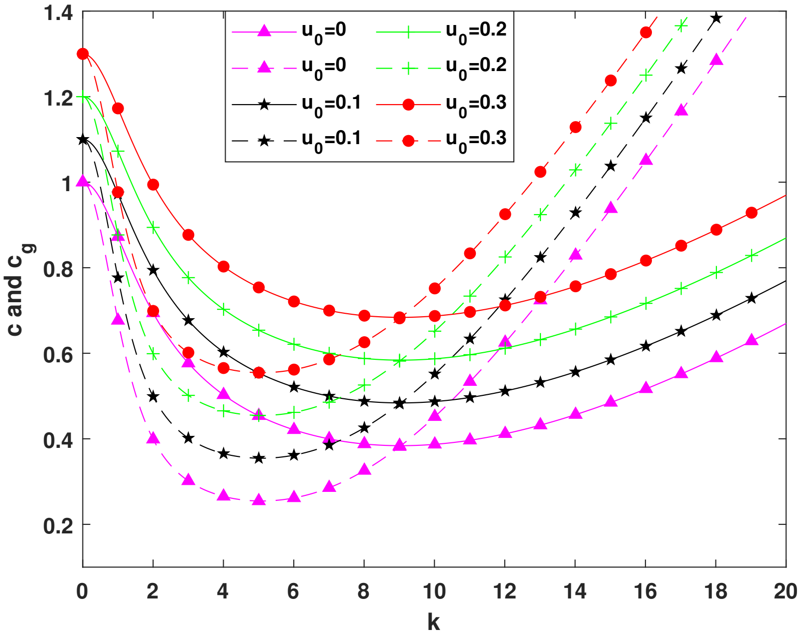

Figure 4.5: Phase speed (c) and group speed (c_g) against wavenumber k for Scenario 2. Solid lines with marker represent phase speed, and broken lines with marker represent group speed.

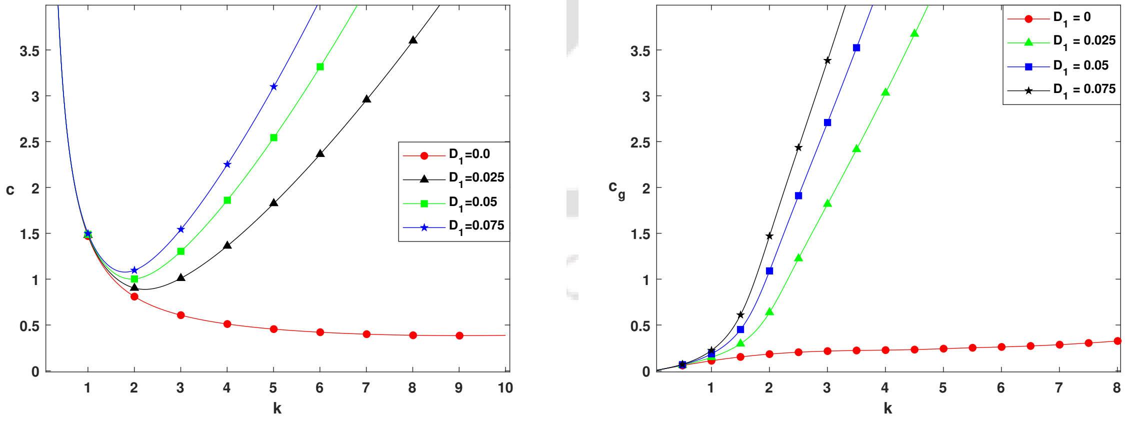

(a)

(b)

Figure 4.6: Variation in phase and group speeds with wavenumber k for Scenario 3: (a) phase speed, (b) group speed.

Increasing the uniform current also enhances the phase speed across the spectrum. As u_0 changes, the minimum of phase speed curve varies notably, illustrating that the uniform current flow and wave dispersion interact. From both figures, the phase speed shows very little changes with the variations in either u_0 or D_1 for longer wavelengths ($k \to 0$). At intermediate and shorter wavelengths, the phase speed varies significantly corresponding to changes in u_0 and D_1.

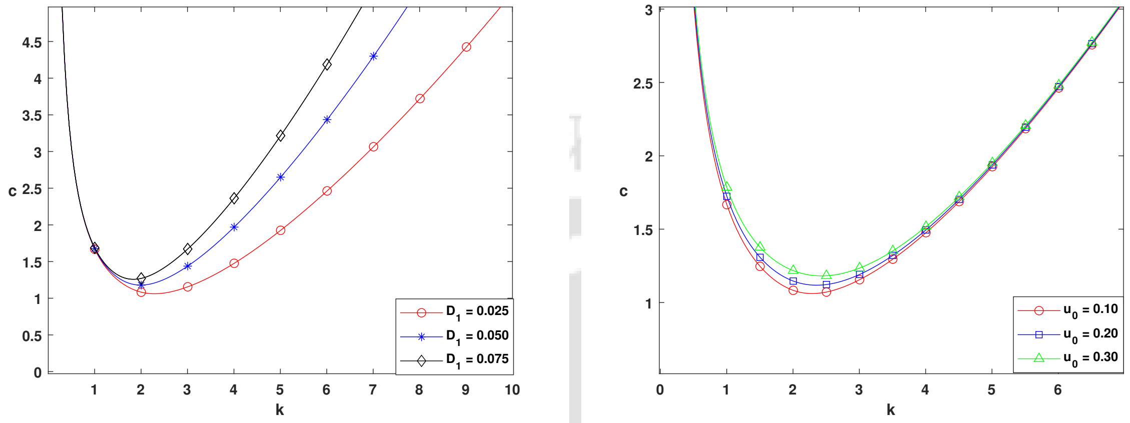

(a) (b)

Figure 4.7: Variation in phase speed c with wavenumber k for Scenario 4: (a) the impact of variation in flexural rigidity D_1 with a fixed value of $u_0 = 0.10$, (b) the impact of variation in uniform current u_0 with a fixed value of $D_1 = 0.025$.

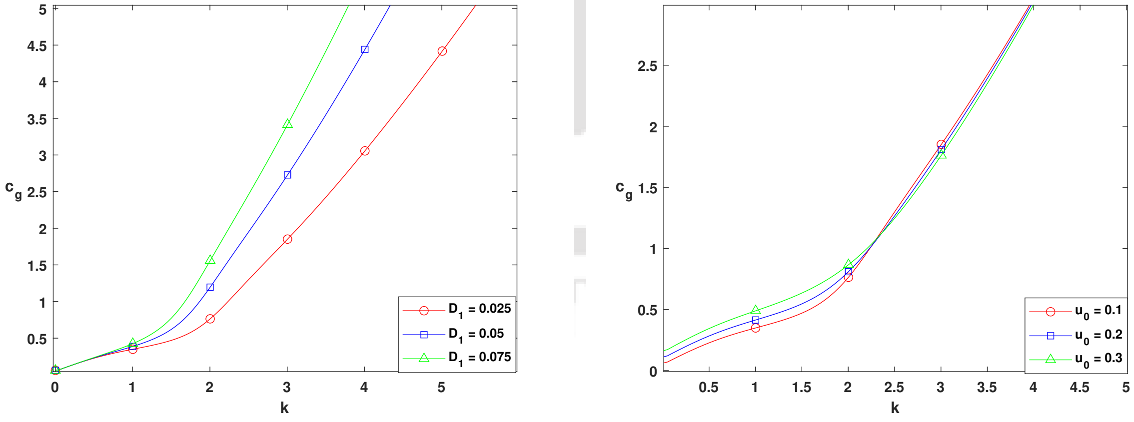

(a) (b)

Figure 4.8: Variation in group speed c_g with wavenumber k for Scenario 4: (a) the impact of variation in flexural rigidity D_1 with a fixed value of $u_0 = 0.10$, (b) the impact of variation in uniform current u_0 with a fixed value of $D_1 = 0.025$.

Figure 4.8 shows the behavior of the group speed c_g against wavenumber k for various circumstances. It is observed that the group speed c_g increases steadily throughout the whole wavenumber range when the flexural rigidity D_1 increases while maintaining a constant uniform current u_0 (Fig. 4.8(a)). This suggests that, for all ranges of wavelengths, the influence of D_1 on the group speed is appreciable. On the other hand, the group speed also increases with u_0 when D_1 is fixed, whereas this variation is only noticeable for the intermediate and long wavelengths. At shorter wavelengths, u_0 has very little effect on the group speed (Fig. 4.8(b)).

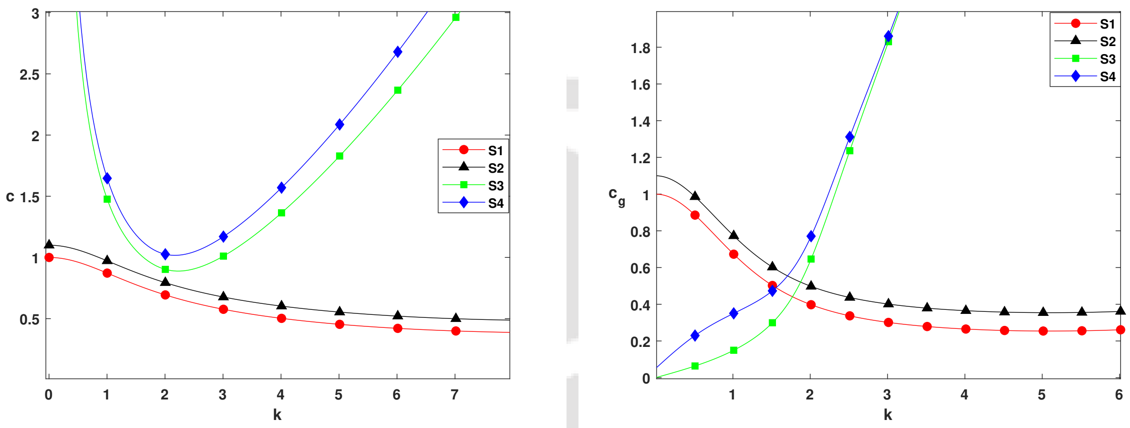

(a) (b)

Figure 4.9: Variation in phase and group speed with wavenumber k for fixed values of $D_1 = 0.025$ and $u_0 = 0.10$: (a) phase speed, (b) group speed.

Figure 4.9(a) depicts the variation of the phase speed while Fig. 4.9(b) depicts the group speed. The behavior of both phase and group speeds for four distinct scenarios is depicted by these figures. In Fig. 4.9, curves S1, S2, S3 and S4 represent the phase and group speeds corresponding to Scenarios 1, 2, 3 and 4, respectively: curve S1 represents the scenario for the rigid bottom case; curve S2 represents the impact of the uniform current with the rigid bottom support; curve S3 represents the scenario where there is the presence of the elastic bottom only; and curve S4 represents the case when both the elastic bottom and the uniform current are taken into account. The figures clearly show that both uniform current and bottom elasticity have significant effects on the wave dynamics. It is clear from Fig. 4.9(a) that the phase speed curve takes a distinct U-shape when the influence of the elasticity is taken into account. This modification demonstrates the important impact of the bottom elasticity on the wave propagation. We can observe from Fig. 4.9(b), which displays the group speed, that the elasticity causes the group speed to gradually increase as the wavenumber increases. The bottom elasticity effect not only changes the contour of the phase speed, but it also contributes to a continuous rise in the group speed.

4.3.3 Ice Sheet Deflection

We first examine a situation in which there is neither an elastic sea-bed nor a uniform current. This is equivalent to a simplified problem involving a rigid sea-bed without any current. Equation (4.15), rather than Eq. (4.16), provides an appropriate dispersion relation for this scenario. To get the wave response for this case, we use this dispersion relation for the ice deflection given by Eq. (4.30).

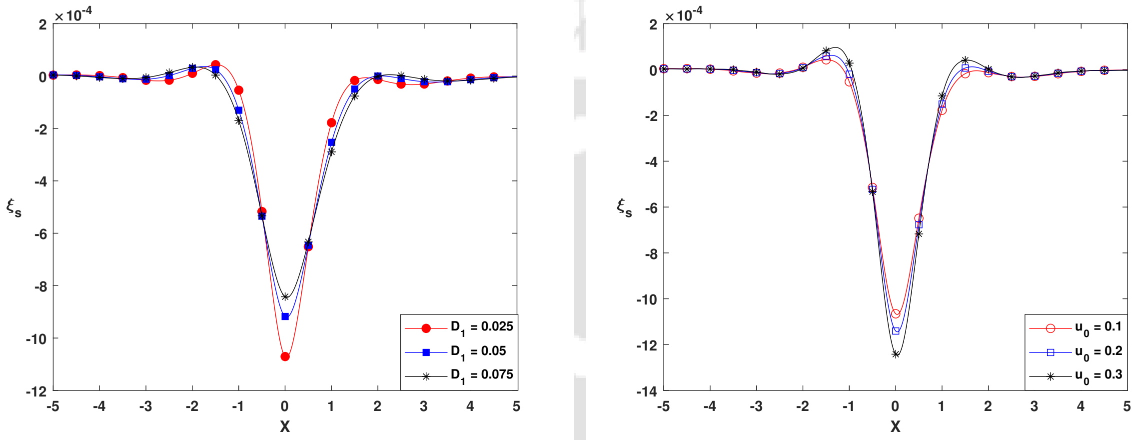

(a) (b)

Figure 4.10: Stationary deflection of ice sheet ξ_s for Scenario 4: (a) variation in D_1 while maintaining fixed $u_0 = 0.10$, (b) variation in u_0 while maintaining fixed $D_1 = 0.025$.

Figure 4.10 shows the stationary deflection profile of the ice sheet for Scenario 4. In the stationary load case, it is observed that the deflection decreases as D_1 increases. Also, the stationary deflection profile exhibits noticeable changes in response to variations in the uniform current u_0.

The ice deflection pattern for three distinct load speed regimes ($V = 0.34 < c_{\min}$, $c_{\min} < V = 0.51 < \sqrt{gH}$ and $V = 1.20 > \sqrt{gH}$) is depicted in Fig. 4.11. It is observed that the wave generation develops as the load speed gets closer to the minimum phase speed. The depression in the neighborhood of the load position expands and moves a bit behind the load as the load speed increases. Furthermore, we observe that, as the speed increases, the wavelength of the waves ahead of the load becomes shorter while the wavelength of the waves behind it increases. This type of ice behavior aligns with the outcomes that have previously been published for such cases (Takizawa (1985), Squire et al. (1996), Hosking and Milinazzo (2022), etc.).

For Scenario 4, we illustrate the ice sheet deflection for three distinct values of V: $V = 0.51 < c_{\min}$ (Fig. 4.12), $V = 1.4 > c_{\min}$ (Fig. 4.13) and $V = 2.2 > c_{\min}$ (Fig. 4.14). It is important to note that the value of $c_{\min}$ depends on D and D_1 (Eq. (4.20)). In this analysis, D is kept fixed while D_1 is varied, which implies that $c_{\min}$ changes according to the values of D_1.

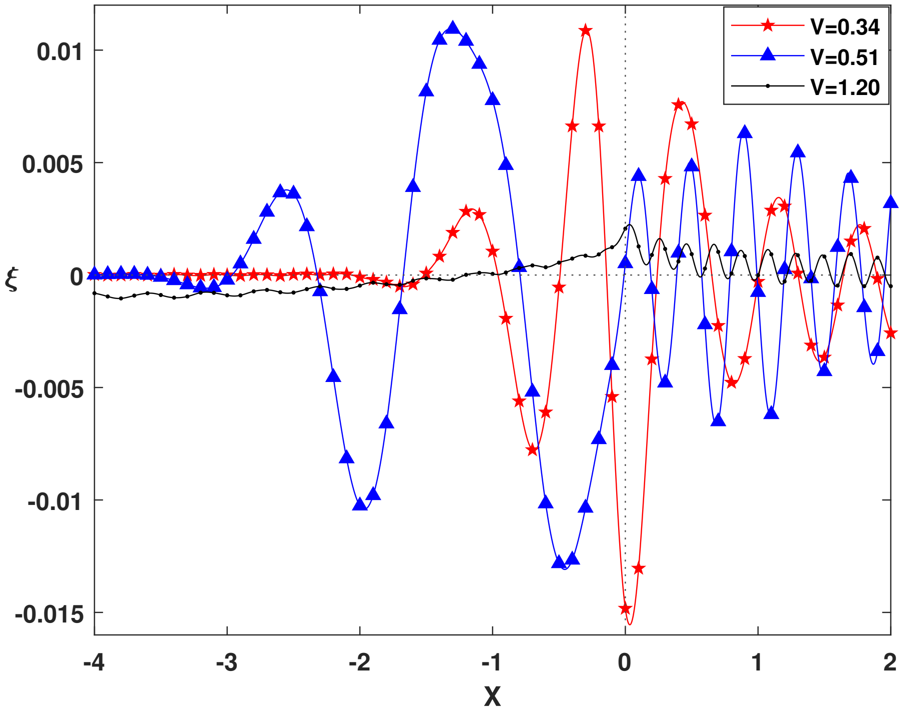

Figure 4.11: Ice sheet deflection ξ vs X for three distinct load speeds ($V = 0.34 < c_{\min}$, $c_{\min} < V = 0.51 < \sqrt{gH}$ and $V = 1.20 > \sqrt{gH}$) at $t = 10$, for Scenario 1 (i.e., without uniform current and bottom elasticity effects), caused by a moving load.

Figure 4.12 illustrates the behavior of the ice deflection for a subcritical speed ($V = 0.51$). The minimum phase speed is significantly higher for both the elastic bottom and uniform current scenarios relative to the rigid bottom scenario. Consequently, there is a significant difference in the deflection behavior in this particular scenario. The depression remains centered beneath the load, much like the response to a stationary load. However, unlike in the stationary load scenario, the wave generation takes place predominantly in front of the moving load. On the other hand, behind the load, the wave amplitude rapidly declines, which indicates asymmetric wave propagation.

The generated waves in the ice sheet for $V = 1.4$ are depicted in Fig. 4.13; long waves occur behind the load, whereas short waves appear in front of it. Furthermore, compared to the waves in front of the load, the amplitude of the trailing waves decays more quickly. The influence of the parameters D_1 and u_0 at the position beneath the load is observed. The deflection just below the load location decreases when D_1 is increased while keeping u_0 fixed. This shows that the depression beneath the load position decreases as the flexural rigidity D_1 of the bed increases. Moreover, it is observed that, when D_1 is kept constant and u_0 increases; the depression beneath the load position increases. This shows that an increase in the uniform current results in an increase in ice deflection at the point just beneath the load.

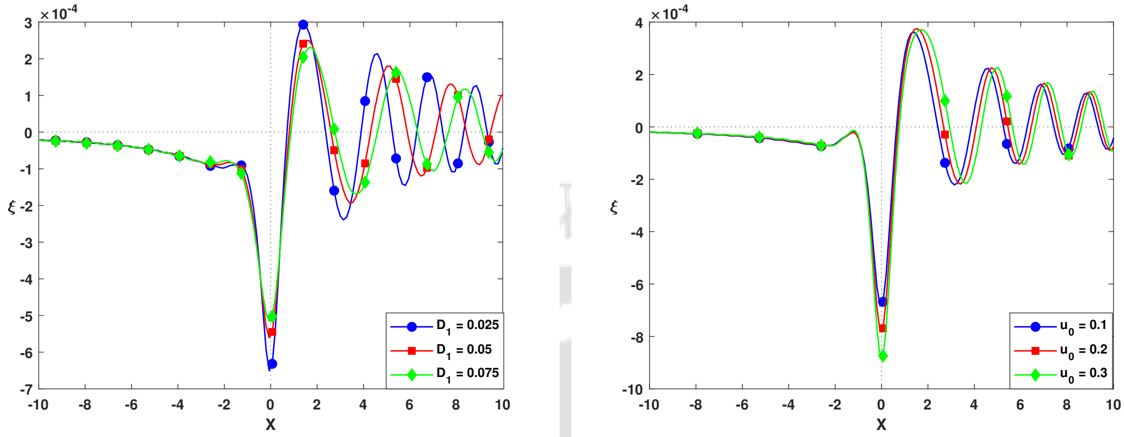

(a) (b)

Figure 4.12: Ice sheet deflection ξ for non-dimensional source speeds $V = 0.51$ at $t = 5$ corresponding to Scenario 4: (a) variation in D_1 while maintaining fixed $u_0 = 0.10$, (b) variation in u_0 while maintaining fixed $D_1 = 0.025$.

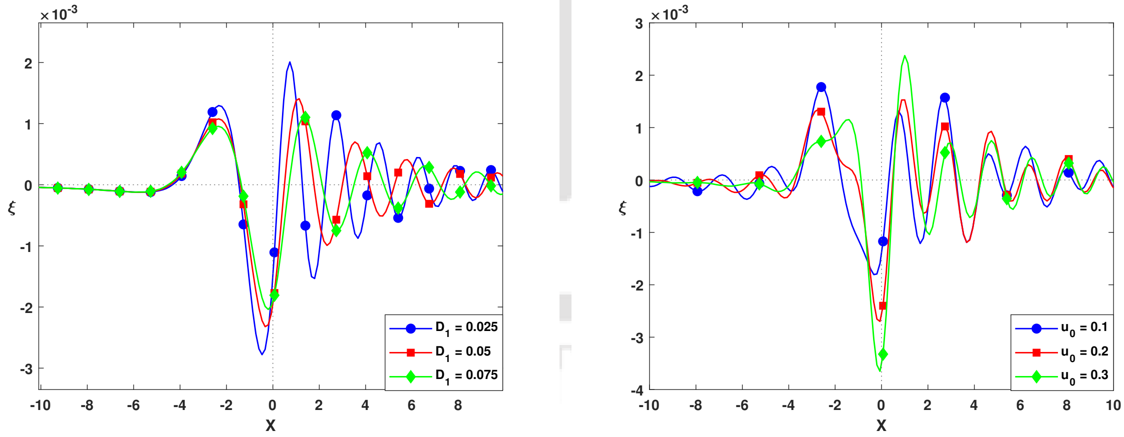

(a) (b)

Figure 4.13: Ice sheet deflection ξ for a specific speed $V = 1.4$ at $t = 5$ corresponding to Scenario 4: (a) variation in flexural rigidity D_1 while maintaining fixed $u_0 = 0.10$, (b) variation in u_0 while maintaining fixed $D_1 = 0.025$.

The key finding is that, even at a higher speed ($V = 1.4$), the trailing waves still appear in the case of an elastic bed. However, with such higher speeds, the wavelength of the trailing waves in the rigid bottom case increases significantly (Fig. 4.11), creating a shadow zone behind the load (just like in Hosking and Milinazzo (2022)). In the elastic bed case, this behavior is not noticed. Furthermore, the rigid bottom case shows very short waves on the front side of the load, but the elastic bed case shows short waves, but with observable differences. This variation is clarified by the fact that the minimum phase speed changes as the bed elasticity increases (Figs. 4.6 and 4.7). As D_1 and u_0 increase, $c_{\min}$ also increases, resulting in a behavior similar to the rigid bottom case when $V > c_{\min}$.

When the load speed is significantly greater ($V = 2.2$) than $c_{\min}$ (Fig. 4.14), the depression becomes wider and lagging behind the load position. In this case, the wavelength of the waves behind the load increases, while the waves in front of the load become much shorter. A combined plot for all the four scenarios is shown in Fig. 4.15. Curves S1, S2, S3, and S4 represent the ice deflection corresponding to the Scenarios 1, 2, 3 and 4, respectively. Curves S1 and S2 show the depression lagging behind the source, while curves S3 and S4 show the highest depression staying centered ($X = 0$). In the first two cases (curves S1 and S2), the moving source is in the supercritical regime ($V > c_{\min}$) while in the last two cases (curves S3 and S4), the speed is in the subcritical regime ($V < c_{\min}$). In the subcritical regime, the depression is more symmetric and localized around the load position, but in the supercritical regime, the wave field trails the source.

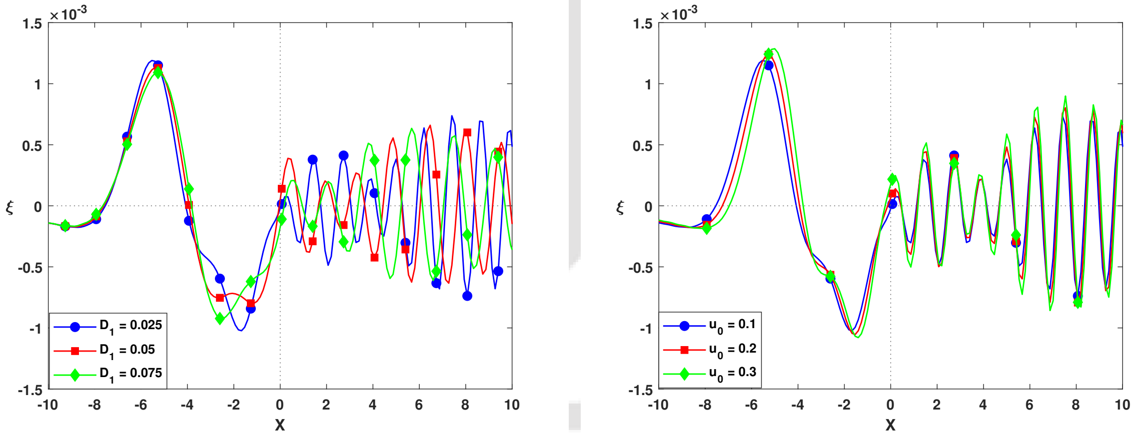

(a) (b)

Figure 4.14: Ice sheet deflection ξ for a specific speed $V = 2.2$ at $t = 5$ corresponding to scenario 4: (a) variation in flexural rigidity D_1 while maintaining fixed $u_0 = 0.10$, (b) variation in u_0 while maintaining fixed $D_1 = 0.025$.

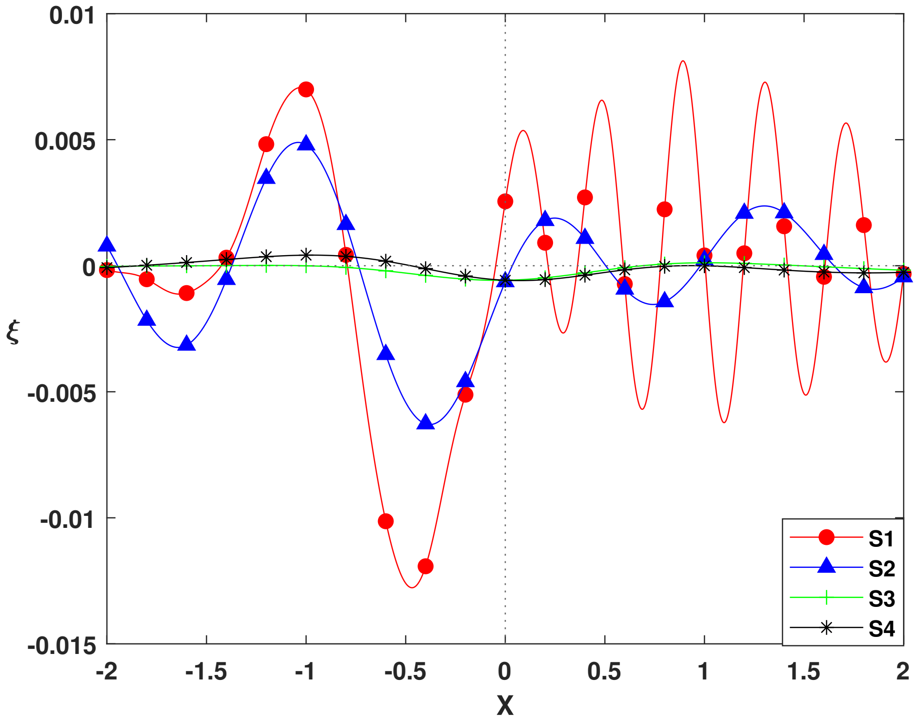

Figure 4.15: Deflection patterns of the ice sheet for $V = 0.51$ at $t = 5$ for all four scenarios.

4.4 Conclusion

We construct a mathematical model to explain the wave response of a thin floating ice sheet due to a moving load in the presence of a uniform current and a flexible sea-bottom. The flexible bottom can be assumed to be represented by an elastic plate following thin plate theory. The corresponding boundary value problem is solved using Fourier transform technique. In order to find out the analytical solution of the ice deflection, an asymptotic method is used. It may be noted that, for speed regime $V > c_{\min}$, the purely imaginary poles contribute to the ice deflection; however, these contributions can be neglected since they have slight discontinuity at the origin.

The dispersion relation expression is obtained and studied under various physical scenarios. It is used to study and discuss the phase speed (c) and group speed (c_g) under different hypotheses. Initially, we discuss the basic case, without any effect (i.e., without uniform current and bottom elasticity effects). In this particular illustration, c and c_g both approach the gravity wave speed ($\sqrt{gH}$) when the wavenumber $k \to 0$. For intermediate range of k, both c and c_g attain their minimum values, while for large k, they progressively increase. The results for c and c_g are found to be similar to the rigid bottom case; the entire set of curves is shifted by u_0 when the uniform current is introduced. However, the key difference is that the curves are adjusted proportionally to

u_0. This change is caused by the Doppler effect, which occurs when a uniform current impacts the perceived frequencies, resulting in a Doppler shift. Moreover, the group speed increases monotonically over the whole k range, whereas the phase speed reaches its minimum at an intermediate range of k when only the influence of bottom elasticity is taken into account. The value of the minimum phase velocity also changes with a change in the bottom elasticity. Further, the phase speed approaches infinity when $k \to 0$. The phase velocity for long-wavelength waves does not significantly change when the bottom elasticity and uniform current are together taken into account. However, the intermediate and short-wavelength ranges show noticeable variations. The tendency of the group speed shows a steady increase, indicating that the energy increases with shorter wavelengths. These results highlight how important the role of sea-bed flexural rigidity/elasticity is in regulating the rate and effectiveness of energy transfer in flexural-gravity wave systems.

The wave patterns generated in the ice sheet by a moving load clearly show the effects of various physical aspects, especially in the deflection just beneath the load position. As the bottom elasticity increases, the deflection decreases, whereas an increase in the uniform current leads to higher deflection just below the position of the load. This occurs as the result of the effect of changes in these parameters, affecting the minimum phase speed. When the load moves at high speeds ($V > \sqrt{gH}$) for such a rigid bottom case, extremely short waves develop in front of the load, while very long waves create a shadow zone behind it. Nevertheless, we observe that waves are generated both ahead and behind the moving load for higher speeds ($V = 1.4,\ 2.2$), accounting for the effects of uniform current and bottom elasticity. Short waves develop in front of the load, but a noticeable wave pattern also forms behind it.

The observations from this study provide important information on various aspects: (a) the behavior of a floating ice sheet under a moving line load, (b) the effect of a uniform current, and (c) the effect of sea-bed elasticity on the phase and group speeds and the deflection of the ice sheet due to a moving load.

CHAPTER 5

Deflection of a floating ice sheet caused by a distributed time-dependent moving line load in the presence of a uniform current

5.1 Mathematical Formulation

We consider an infinitely long homogeneous ice sheet with thickness h and density ρ_i in the presence of a uniform current. Assuming that ρ is the constant density of water, the depth of fluid domain is considered from the ice-covered surface to the sea bottom at $z = -H$, with the negative z-axis in the gravitational direction. Additionally, the fluid is assumed to be incompressible, inviscid, and the motion irrotational, which simplifies the governing equations and allows the use of potential flow theory. Let us consider $\Phi(x, z, t)$ to be the velocity potential and $\xi(x, t)$ the ice sheet deflection. The sketch of the problem is shown in Fig. 5.1. In this study, the ice sheet is treated as a thin plate since its behavior is considered to follow the assumptions of thin plate as also followed in Milinazzo et al. (1995) and some other works, including our earlier problems.

According to Davys et al. (1985), the equation governing the motion of the ice sheet is

$$D\nabla^4\xi + \rho_i h\xi_{tt} = p - f(x, t). \tag{5.1}$$

We utilize the assumption that the current flows uniformly at a constant speed $\mathbf{U} = u_0\hat{i}$ beneath the ice sheet, where u_0 is directed along the positive x-axis, with $u_0 > 0$. Therefore, during the wave motion, the perturbed velocity is taken as $\bigoplus = \mathbf{U} + \nabla\Phi$. Thus, at $z = 0$, the pressure governed by the linearized form of the Bernoulli's equation

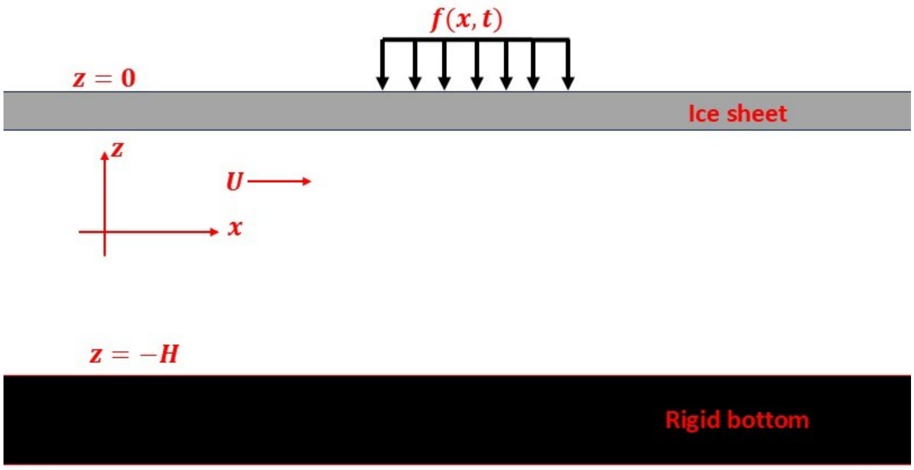

Figure 5.1: Schematic diagram of a floating ice sheet

is

$$p = -\rho(\Phi_t + \mathbf{U}.\nabla\Phi) - \rho g\xi. \tag{5.2}$$

From Eqs. (5.1) and (5.2), the dynamic equation of the ice plate gets modified in the presence of the current as follows:

$$D\nabla^4\xi + \rho g\xi = -\rho(\Phi_t + \mathbf{U}.\nabla\Phi) - f(x,t). \tag{5.3}$$

We focus on the wave motion with wavelengths much greater than the thickness of the plate. The fluid is penetrated by the wave motion to a depth determined by the wavelength, which is associated with the hybrid waves of interest and is commonly much greater than the thickness of the plate, but may be similar to the fluid depth. Because of this, unless the waves are very short, the inertia of the flowing fluid layer is much larger compared to the inertia of the thin plate. Thus, the plate inertial term ($\rho_i h\xi_{tt}$) for the ice sheet can be considered negligible. That is why we neglect $\rho_i h\xi_{tt}$ term in Eq. (5.1). Due to the adoption of potential flow, Φ satisfies the Laplace's equation, bottom boundary condition and kinematic condition along with the dynamic condition as follows:

$$\Phi_{xx} + \Phi_{zz} = 0 \quad \text{in} \quad -\infty < x < \infty, \quad -H < z < 0, \tag{5.4}$$

$$\Phi_z = \xi_t + u_0\nabla\xi \quad \text{at} \quad z = 0, \tag{5.5}$$

$$\Phi_z = 0 \quad \text{at} \quad z = -H, \tag{5.6}$$

$$D\nabla^4\xi + \rho g\xi = -\rho(\Phi_t + u_0\nabla\Phi) - f(x,t) \quad \text{at} \quad z = 0. \tag{5.7}$$

The initial conditions are considered as $\Phi(x,z,0) = 0$ and $\xi(x,0) = 0$. For finding the deflection ξ, the Laplace–Fourier transform method is employed. Let $\bar{\mathscr{R}}(x,z,s)$ be the Laplace transform of the function $\mathscr{R}(x,z,t)$ in time t, defined as

$$\bar{\mathscr{R}}(x,z,s) = \int_0^\infty \mathscr{R}(x,z,t)e^{-st}\,dt,$$

and let $\hat{\bar{\mathscr{R}}}(k,z,s)$ be the Fourier transform of $\bar{\mathscr{R}}(x,z,s)$ with respect to x, defined as

$$\hat{\bar{\mathscr{R}}}(k,z,s) = \int_{-\infty}^{\infty} \bar{\mathscr{R}}(x,z,s)e^{-\mathrm{i}kx}\,dx,$$

where s and k are the transformed variables corresponding to the Laplace and Fourier transforms, respectively, with k representing the wavenumber.

We take the Laplace–Fourier transform of Eqs. (5.4) to (5.7) to get, respectively, the following:

$$\frac{d^2\hat{\bar{\Phi}}}{dz^2} - k^2\hat{\bar{\Phi}} = 0, \tag{5.8}$$

$$\frac{d\hat{\bar{\Phi}}}{dz} = (s + \mathrm{i}ku_0)\hat{\bar{\xi}}, \tag{5.9}$$

$$\frac{d\hat{\bar{\Phi}}}{dz} = 0, \tag{5.10}$$

$$Dk^4\hat{\bar{\xi}} + \rho g\hat{\bar{\xi}} = -\rho(s + \mathrm{i}ku_0)\hat{\bar{\Phi}} - \hat{\bar{f}}(k,s). \tag{5.11}$$

The expression of $\hat{\bar{\Phi}}$ is found by solving Eqs. (5.8) to (5.10), which yields

$$\hat{\bar{\Phi}} = \frac{(s + \mathrm{i}ku_0)}{k}\frac{\cosh(k(z+H))}{\sinh(kH)}\hat{\bar{\xi}}. \tag{5.12}$$

Then, Eq. (5.12) yields its value at $z = 0$ as

$$\hat{\bar{\Phi}} = \frac{(s + \mathrm{i}ku_0)}{k}\coth(kH)\hat{\bar{\xi}}. \tag{5.13}$$

Furthermore, we substitute Eq. (5.13) in (5.11) to get

$$Dk^4\hat{\bar{\xi}} + \rho g\hat{\bar{\xi}} = -\rho\frac{(s + \mathrm{i}ku_0)^2}{k}\coth(kH)\hat{\bar{\xi}} - \hat{\bar{f}}(k,s). \tag{5.14}$$

To determine the expression of $\hat{\bar{\xi}}$, we simplify Eq. (5.14), and obtain the following form:

$$\hat{\bar{\xi}} = -\frac{k\tanh(kH)\hat{\bar{f}}(k,s)}{\rho\mathscr{B}}, \tag{5.15}$$

where $\mathscr{B} = s^2 + (2\mathrm{i}ku_0)s + (\omega^2 - 2ku_0\omega)$. The relation between ω and k is given by a transcendental equation as follows:

$$\omega_D = \sqrt{\left(\frac{Dk^4}{\rho} + g\right)k\tanh(kH)}, \tag{5.16}$$

where $\omega_D = \omega - ku_0$ is the Doppler shift frequency, with ω given by

$$\omega = ku_0 \pm \sqrt{\left(\frac{Dk^4}{\rho} + g\right)k\tanh(kH)}. \tag{5.17}$$

The phase speed c and group speed c_g of the waves are given by $c = \omega/k$ and $c_g = d\omega/dk$, respectively. The phase speed is

$$c = u_0 \pm \sqrt{\left(\frac{Dk^3}{\rho} + \frac{g}{k}\right)\tanh(kH)}. \tag{5.18}$$

For intermediate wavelengths such that $(kH \gg 1)$, we have $\tanh(kH) \approx 1$. Therefore, the phase speed c simplifies to

$$c = u_0 \pm \sqrt{\frac{Dk^3}{\rho} + \frac{g}{k}}. \tag{5.19}$$

The minimum phase speed ($c_{\min}$) occurs at a specific wavenumber $k_{\min}$ (say), where the phase speed c becomes equal to the group speed c_g. This can be located by the stationary point of Eq. (5.19), that is, by setting $dc/dk = 0$. Therefore, we have

$$c_{\min} = u_0 \pm 2\sqrt[8]{\frac{Dg^3}{27\rho}} \tag{5.20}$$

corresponding to $k_{\min} = \sqrt[4]{\rho g/3D}$. It is noticeable that the minimum phase speed $c_{\min}$ is directly influenced by the presence of the uniform current u_0. However, the wavenumber $k_{\min}$ corresponding to this minimum phase speed remains unchanged. It seems that the wavenumber and thus the wavelength corresponding to the minimum phase speed $c_{\min}$ are unaffected by the uniform current u_0, even though it causes a linear shift in the phase speed, either increasing or decreasing, based on the current direction. In physical terms, this indicates that the flow simply affects the dispersion curve without changing its shape because the background current has no effect on the balance between flexural and gravitational restoring forces, which determines $k_{\min}$.

The following physical parameter values, as in Takizawa (1985), are considered: $E = 5.1 \times 10^8 \mathrm{N/m^2}$, $h = 0.17\mathrm{m}$, $H = 6.80\mathrm{m}$, $\nu = 1/3$, $g = 9.81\mathrm{m/s^2}$, and $\rho = 1026\mathrm{kg/m^3}$. Figure 5.2 illustrates the variation of phase speed c and group speed c_g against wavenumber k in the absence of a uniform current, whereas Fig. 5.3 depicts the corresponding curves for different values of the uniform current u_0. These figures clearly show that the phase and group speed curves show a linear shift due to the addition of a uniform current; however, their overall shape and spatial properties remain unchanged. In terms of physics, this means that the background flow alters the dispersion relation linearly without altering its basic shape, modifying simply the propagation speed by superposing its speed on the intrinsic wave motion.

5.2 A Particular Loading Function

We consider a special type of distributed harmonic line load that is spatially located over a finite length ($2l_0$) on the ice sheet, and the motion of the load is governed by a variable

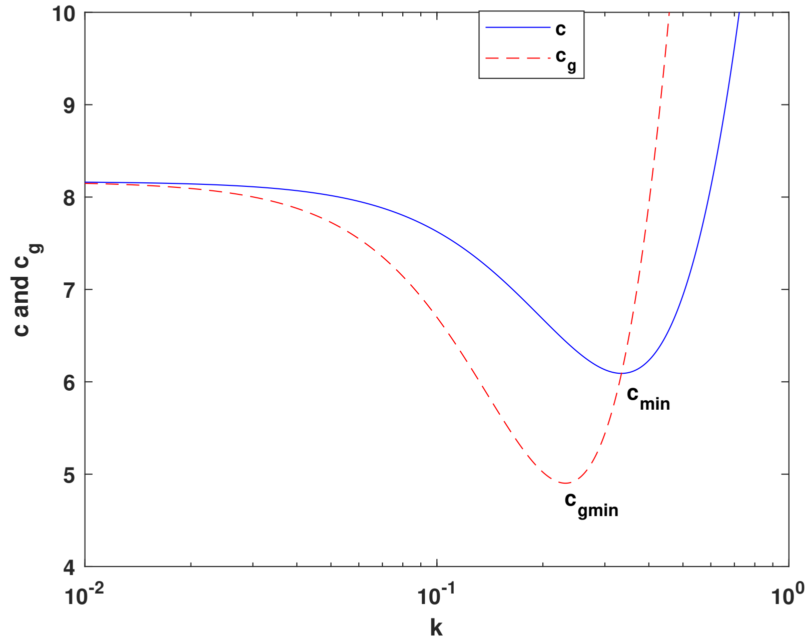

Figure 5.2: Variation of phase and group speeds in the absence of uniform current u_0.

speed function $\mathcal{V}(t)$. Therefore, the loading function is defined as follows:

$$f(x,t) = F_0 e^{\mathrm{i}\Omega t}\left\{\frac{u[l_0^2 - (x - \mathcal{V}(t))^2]}{2l_0}\right\}, \tag{5.21}$$

where F_0 is the weight of the load, Ω is the angular wave frequency of the load that is different from the standard angular wave frequency ω, and $u(.)$ is the Heaviside step function given by

$$u(x - x_0) = \begin{cases} 0 & \text{if} \quad x < x_0, \\ 1/2 & \text{if} \quad x = x_0, \\ 1 & \text{if} \quad x > x_0. \end{cases}$$

We employ the Laplace-Fourier transform on $f(x,t)$ to get

$$\begin{aligned} \hat{\bar{f}}(k,s) &= \int_{-\infty}^{\infty}\int_{0}^{\infty} f(x,t) e^{-\mathrm{i}kx} e^{-st}\, dt\, dx, \\ &= \int_{-\infty}^{\infty}\int_{0}^{\infty} F_0 e^{\mathrm{i}\Omega t}\left\{\frac{u[l_0^2 - (x - \mathcal{V}(t))^2]}{2l_0}\right\} e^{-\mathrm{i}kx} e^{-st}\, dt\, dx. \end{aligned} \tag{5.22}$$

The integral involving the Heaviside function is given by

$$\int_{-\infty}^{\infty} u[l_0^2 - (x - \mathcal{V}(t))^2] e^{-\mathrm{i}kx} dx = \int_{\mathcal{V}(t)-l_0}^{\mathcal{V}(t)+l_0} e^{-\mathrm{i}kx} dx = 2\frac{\sin(kl_0)}{k} e^{-\mathrm{i}k\mathcal{V}(t)}. \tag{5.23}$$

From Eqs. (5.22) and (5.23), we have

$$\hat{\bar{f}}(k,s) = F_0 \mathcal{G}\frac{\sin(kl_0)}{kl_0}, \tag{5.24}$$

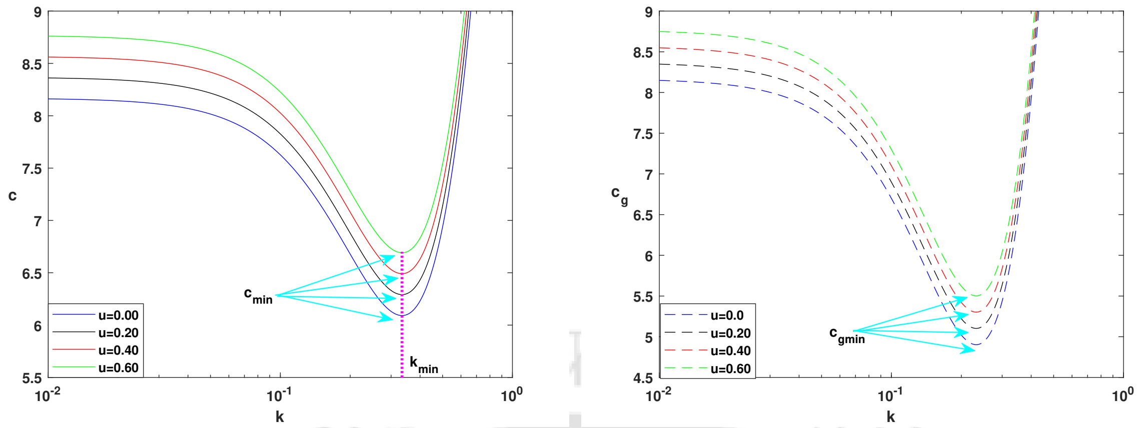

(a) (b)

Figure 5.3: Phase and group speed curves versus wavenumber for different uniform current u_0: (a) phase speed c, (b) group speed c_g.

where

$$\mathscr{I} = \int_0^\infty e^{(-s+\mathrm{i}\Omega)t} e^{-\mathrm{i}k\mathscr{V}(t)} dt. \tag{5.25}$$

Therefore, $\hat{\hat{\xi}}(k, s)$ can be written as

$$\hat{\hat{\xi}} = -F_0 \mathscr{I} \frac{k\tanh(kH)}{\rho\mathscr{B}} \frac{\sin(kl_0)}{kl_0}. \tag{5.26}$$

The original function $\xi(x, t)$ can be reconstructed using the corresponding inverse Laplace-Fourier transform, which is given by

$$\xi(x, t) = \mathscr{L}^{-1}\mathscr{F}^{-1}\{\hat{\hat{\xi}}(k, s)\},$$

where $\mathscr{L}^{-1}$ and $\mathscr{F}^{-1}$ denote the inverse Laplace and Fourier transforms, respectively. Therefore,

$$\xi = \frac{F_0}{\sqrt{2\pi}\rho} \int_{-\infty}^{\infty} \frac{\sin(kl_0)}{kl_0} k\tanh(kH) \left(\mathscr{L}^{-1}\left\{\frac{1}{\mathscr{B}}\mathscr{I}\right\}\right) e^{\mathrm{i}kx}\, dk. \tag{5.27}$$

The convolution theorem of Laplace transform is given by

$$\mathscr{L}^{-1}\{\mathbf{g}_1(s)\mathbf{g}_2(s)\} = \mathscr{G}_1 * \mathscr{G}_2 = \int_0^t \mathscr{G}_1(\tau)\mathscr{G}_2(t-\tau)\, d\tau,$$

where $\mathscr{L}^{-1}\{\mathbf{g}_1(s)\} = \mathscr{G}_1(t)$ and $\mathscr{L}^{-1}\{\mathbf{g}_2(s)\} = \mathscr{G}_2(t)$. Thus, with the help of convolution theorem, we get the expression of ξ as

$$\xi = \frac{-F_0}{\sqrt{2\pi}\rho} \int_{-\infty}^{\infty} \frac{\sin(kl_0)}{kl_0} \frac{\tanh(kH)}{(c-u_0)} e^{\mathrm{i}kx} \mathscr{I}_c\, dk, \tag{5.28}$$

where $\mathscr{I}_c = \left\{\int_0^t e^{\mathrm{i}\Omega\tau} e^{-\mathrm{i}k\mathcal{V}(\tau)} e^{-\mathrm{i}ku_0\tau} \sin(k(c-u_0)(t-\tau))\, d\tau\right\}$. We simplify $\mathscr{I}_c$ as

$$\begin{aligned}
\mathscr{I}_c &= \int_0^t e^{\mathrm{i}\Omega\tau} e^{-\mathrm{i}k\mathcal{V}(\tau)} e^{-\mathrm{i}ku_0\tau} \sin(k(c-u_0)(t-\tau))\, d\tau \\
&= \int_0^t e^{\mathrm{i}\Omega\tau} e^{-\mathrm{i}k\mathcal{V}(\tau)} e^{-\mathrm{i}ku_0\tau} \left\{ \frac{e^{\mathrm{i}k(c-u_0)(t-\tau)} - e^{-\mathrm{i}k(c-u_0)(t-\tau)}}{2\mathrm{i}} \right\} d\tau \\
&= \frac{1}{2\mathrm{i}} \left[\mathscr{I}_1 e^{\mathrm{i}k(c-u_0)t} - \mathscr{I}_2 e^{-\mathrm{i}k(c-u_0)t} \right], \qquad (5.29)
\end{aligned}$$

where

$$\mathscr{I}_1 = \int_0^t e^{\mathrm{i}(\Omega-ku_0)\tau} e^{-\mathrm{i}k(\mathcal{V}(\tau)+(c-u_0)\tau)}\, d\tau, \qquad (5.30)$$

$$\mathscr{I}_2 = \int_0^t e^{\mathrm{i}(\Omega-ku_0)\tau} e^{-\mathrm{i}k(\mathcal{V}(\tau)-(c-u_0)\tau)}\, d\tau. \qquad (5.31)$$

Now, Eq. (5.28) becomes

$$\xi = \frac{-F_0}{\sqrt{2\pi}\rho} \int_{-\infty}^{\infty} \frac{\sin(kl_0)}{kl_0} \frac{\tanh(kH)}{2\mathrm{i}(c-u_0)} \left[\mathscr{I}_1 e^{\mathrm{i}k(c-u_0)t} - \mathscr{I}_2 e^{-\mathrm{i}k(c-u_0)t} \right] e^{\mathrm{i}kx}\, dk. \qquad (5.32)$$

If a concentrated point load replaces the distributed line load, taking the limit ($l_0 \to 0$) of Eq. (5.32), we get

$$\xi_p = \frac{-F_0}{\sqrt{2\pi}\rho} \int_{-\infty}^{\infty} \frac{\tanh(kH)}{2\mathrm{i}(c-u_0)} \left[\mathscr{I}_1 e^{\mathrm{i}k(c-u_0)t} - \mathscr{I}_2 e^{-\mathrm{i}k(c-u_0)t} \right] e^{\mathrm{i}kx}\, dk, \qquad (5.33)$$

where ξ_p is the deflection corresponding to the concentrated point load. If we consider a particular case in which there is no uniform current, i.e., $u_0 = 0$, and that a moving load, represented by $f(x,t) = F_0\delta(x - \mathcal{V}(t))$, is applied instead of a time-dependent line load, Eq. (5.33) yields

$$\xi_p = \frac{-F_0}{\sqrt{2\pi}\rho} \int_{-\infty}^{\infty} \frac{\tanh(kH)}{2\mathrm{i}c} \left[\mathscr{I}_1^* e^{\mathrm{i}kct} - \mathscr{I}_2^* e^{-\mathrm{i}kct} \right] e^{\mathrm{i}kx}\, dk, \qquad (5.34)$$

where $\mathscr{I}_1^* = \int_0^t e^{-\mathrm{i}k(\mathcal{V}(\tau)+c\tau)}\, d\tau$ and $\mathscr{I}_2^* = \int_0^t e^{-\mathrm{i}k(\mathcal{V}(\tau)-c\tau)}\, d\tau$. Eq. (5.34) is the same as Eq. (2.8) that is presented by Hosking and Milinazzo (2022) for this particular case.

We examine the dynamic response of the floating ice sheet for different natures of the moving loads. In particular, we take into account an impulsively started steadily moving load, a uniformly accelerating load, and a uniformly decelerating load.

5.2.1 Response due to an Impulsively Started Steadily Moving Load

We analyze the deflection $\xi(x,t)$ (Eq. (5.32)) of the ice sheet due to a line load that starts moving with a constant speed V in the positive x-direction at time $t = 0$, such that

$\mathscr{V}(t) = Vt,\ t > 0$. Therefore, Eqs. (5.30) and (5.31) lead to

$$\mathscr{I}_1 = \frac{e^{\mathrm{i}(\Omega - kV - kc)t} - 1}{\mathrm{i}(\Omega - kV - kc)}, \tag{5.35}$$

$$\mathscr{I}_2 = \frac{e^{\mathrm{i}(\Omega - 2ku_0 - kV + kc)t} - 1}{\mathrm{i}(\Omega - 2ku_0 - kV + kc)}. \tag{5.36}$$

We substitute the values of $\mathscr{I}_1$ and $\mathscr{I}_2$ in Eq. (5.32) to get

$$\xi = \frac{F_0}{\sqrt{2\pi}\rho}\int_{-\infty}^{\infty} \frac{\sin(kl_0)}{kl_0}\frac{\tanh(kH)}{2(c-u_0)}\left\{\frac{2k(c-u_0)e^{\mathrm{i}\Omega t}e^{\mathrm{i}k(x-Vt-u_0t)}}{[(\Omega - k(V+u_0))^2 - k^2(c-u_0)^2]}\right.$$
$$\left. - \frac{e^{\mathrm{i}k(x+ct-u_0t)}}{[(\Omega - k(V+u_0)) - k(c-u_0)]} + \frac{e^{\mathrm{i}k(x-ct-u_0t)}}{[(\Omega - k(V+u_0)) + k(c-u_0)]}\right\}\, dk. \tag{5.37}$$

We can write it in a more simplified form as

$$\xi = \frac{F_0}{\sqrt{2\pi}\rho}\{I_1 + I_2 + I_3\}, \tag{5.38}$$

where

$$I_1 = \int_{-\infty}^{\infty} \frac{\sin(kl_0)}{kl_0}\frac{k\tanh(kH)}{\mathscr{D}_1(k)\mathscr{D}_2(k)}e^{\mathrm{i}\Omega t}e^{\mathrm{i}k(x-Vt-u_0t)}\, dk, \tag{5.39}$$

$$I_2 = -\int_{-\infty}^{\infty} \frac{\sin(kl_0)}{2kl_0}\frac{\tanh(kH)}{(c-u_0)\mathscr{D}_1(k)}e^{\mathrm{i}k(x+ct-u_0t)}\, dk, \tag{5.40}$$

$$I_3 = \int_{-\infty}^{\infty} \frac{\sin(kl_0)}{2kl_0}\frac{\tanh(kH)}{(c-u_0)\mathscr{D}_2(k)}e^{\mathrm{i}k(x-ct-u_0t)}\, dk. \tag{5.41}$$

Here, $\mathscr{D}_1(k) = [\Omega - k(V+u_0)] - k(c-u_0)$ and $\mathscr{D}_2(k) = [\Omega - k(V+u_0)] + k(c-u_0)$. The behavior of these integrals depends on the zeros the denominator, i.e., zeros of $\mathscr{D}_1$ and $\mathscr{D}_2$. In other words, we utilize the Residue Theorem to study the behavior of the integrals. $\mathscr{D}_1(k) = 0 \implies \Omega/k - V = c$ and $\mathscr{D}_2 = 0 \implies \Omega/k - V = -\omega_D/k + u_0$. In a physical sense, this is the interaction among the parameters of the moving load such as frequency Ω, speed V and the wave dynamics, i.e., the phase speed c of the waves or the Doppler-shifted frequency ω_D. This interaction is important for determining and analyzing the behavior of the generated waves and the energy transfer within the system.

We consider the range of load frequency Ω in connection with the natural frequency $\omega(= kc)$ ($\Omega = \omega$, $\Omega < \omega$ and $\Omega > \omega$). These configurations enable a thorough evaluation of the frequency-response behavior of the ice sheet. The results for these scenarios and the accompanying figures are shown in Section 5.3 to illustrate how changes in the load frequency affect the amplitude and behavior of the waves generated by the oscillatory load.

5.2.2 Response due to a Uniformly Accelerating Line Load

We analyze the response of the ice sheet due to a line load influenced by a uniform acceleration. In this case, the load starts from rest at time $t = 0$ and moves in the positive

x-direction with a constant acceleration. The acceleration term is given by $At^2/2$, $t > 0$ (Miles and Sneyd (2003)), where A denotes the constant acceleration. For this case, the integral $\mathcal{I}_1$ is evaluated as follows:

$$\begin{aligned}\mathcal{I}_1 &= \int_0^t e^{\mathrm{i}(\Omega - ku_0)\tau} e^{-\mathrm{i}k(V\tau + A\tau^2/2 + (c-u_0)\tau)}\, d\tau \\ &= \int_0^t e^{\mathrm{i}(-\alpha_1\tau^2 + \alpha_2\tau)}\, d\tau = e^{-\mathrm{i}\alpha} \int_0^t e^{-i\alpha_1\left(\tau - \frac{\alpha_2}{2\alpha_1}\right)^2}\, d\tau, \end{aligned} \tag{5.42}$$

where $\alpha_1 = kA/2$, $\alpha_2 = \Omega - k(c+V)$ and $\alpha = \alpha_2^2/(4\alpha_1)$.

Equation (5.42) contains a Fresnel-type integral that can be represented using the Fresnel sine and cosine integrals. These integrals are commonly seen in wave propagation and diffraction problems, especially in systems that show oscillating behavior regulated by quadratic phase functions. The Fresnel integral is given by

$$\mathcal{F}(\beta) = \int_0^\beta e^{\mathrm{i}\gamma^2}\, d\gamma = \sqrt{\frac{\pi}{2}}\mathcal{C}\left(\sqrt{\frac{2}{\pi}}\beta\right) + \mathrm{i}\sqrt{\frac{\pi}{2}}\mathcal{S}\left(\sqrt{\frac{2}{\pi}}\beta\right), \tag{5.43}$$

where $\mathcal{C}(x)$ and $\mathcal{S}(x)$ are the Fresnel cosine and sine integrals, respectively. As a consequence, Eq. (5.42) can be written as

$$\mathcal{I}_1 = e^{-\mathrm{i}\alpha}\sqrt{\frac{\pi}{2\alpha_1}}\left[(\mathcal{C}(\gamma_2) - \mathcal{C}(\gamma_1)) - \mathrm{i}(\mathcal{S}(\gamma_1) - \mathcal{S}(\gamma_2))\right], \tag{5.44}$$

where

$$\gamma_1 = -\frac{\alpha_2}{\sqrt{2\pi\alpha_1}}, \quad \gamma_2 = \sqrt{\frac{2\alpha_1}{\pi}}\left(t - \frac{\alpha_2}{2\alpha_1}\right).$$

The expression of $\mathcal{I}_2$ is similar to Eq. (5.44), with only α_2 replaced by $\alpha_2 = \Omega - k(2u_0 + V - c)$. We can say that, when the load moves with a uniform acceleration, the integrand does not exhibit any singularities.

5.2.3 Response due to a Uniformly Decelerating Line Load

We analyze the response of the ice sheet due to a line load influenced by a uniform deceleration. In this case, the load starts from rest at time $t = 0$ and moves in the positive x-direction with a constant deceleration $(-A)$. The load position as a function of time is given by $\mathcal{V}(t) = Vt - At^2/2$, $t > 0$ (Miles and Sneyd (2003)). Hence,

$$\mathcal{I}_1 = \int_0^t e^{\mathrm{i}(\alpha_1\tau^2 + \alpha_2\tau)}\, d\tau = e^{-\mathrm{i}\alpha}\int_0^t e^{i\alpha_1\left(\tau + \frac{\alpha_2}{2\alpha_1}\right)^2}\, d\tau, \tag{5.45}$$

where $\alpha_2 = \Omega - k(2u_0 + V - c)$, while α and α_1 expressions are the same as in the last case in the expression of $\mathcal{I}_1$. The expression of $\mathcal{I}_1$ is similar to Eq. (5.44) with changes only in γ_1 and γ_2 given by

$$\gamma_1 = \frac{\alpha_2}{\sqrt{2\pi\alpha_1}}, \quad \gamma_2 = \sqrt{\frac{2\alpha_1}{\pi}}\left(t + \frac{\alpha_2}{2\alpha_1}\right).$$

The expression of $\mathcal{I}_2$ is similar to the expression of Eq. (5.45), with only α_2 replaced by $\alpha_2 = \Omega - k(2u_0 + V - c)$. As in the case a uniformly accelerating load, in this case when the load moves with a constant deceleration, the integrand does not exhibit any singularities.

5.3 Numerical Results

We carry out numerical experiments to illustrate and examine the deflection behavior of the floating ice sheet under a moving load, based on the analytical conclusions obtained in the preceding section. For the moving load, we take into account three different speeds: subcritical speed $V = 5.5\text{m/s} < c_{\min}$, $c_{\min} < V = 7.1\text{m/s} < \sqrt{gH}$, and supercritical speed $V = 9.1\text{m/s} > \sqrt{gH}$. Here, $c_{\min} = 6.01\text{m/s}$ and $\sqrt{gH} = 8.16\text{m/s}$. These values correspond to the case without the uniform current u_0. The inclusion of u_0 modifies the value of the minimum phase speed $c_{\min}$, as given by Eq. (5.20). The upward-pointing arrow in all of these figures indicates the position of the load, i.e., the load exists at this spot.

5.3.1 Validation and Results for Constant Speed

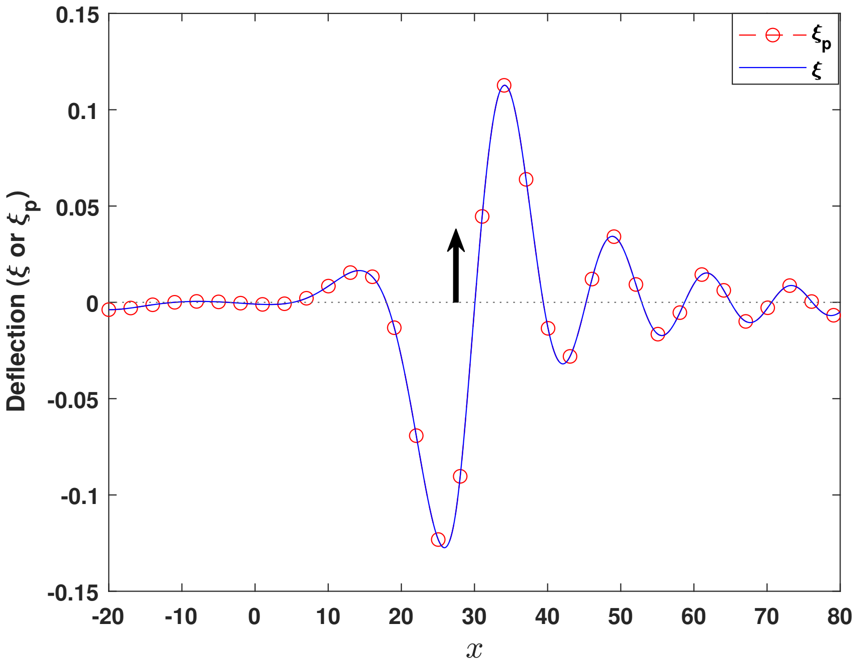

Figure 5.4: Comparison of deflection ξ with ξ_p. The deflection ξ approaches ξ_p as the load frequency Ω, load half-length l_0, and uniform current u_0 tend to zero. The load moves with a speed 5.5 m/s at time $t = 5$s.

At the initial time $t = 0$, the load is assumed to move at a constant speed V. After some time t, it reaches the point $x = Vt$, giving the location of the load at time t by $x = Vt$.

The deflection ξ derived from our model (Eq. (5.32)) and the reference solution ξ_p (Eq. (5.34)) are shown in Figs. 5.4, 5.5 and 5.6 for load speed $V = 5.5$, 7.1 and 9.2m/s, respectively. We notice that our results converge to the deflection profile corresponding to a concentrated point load as the parameters $\Omega \to 0$, $l_0 \to 0$, and $u_0 \to 0$.

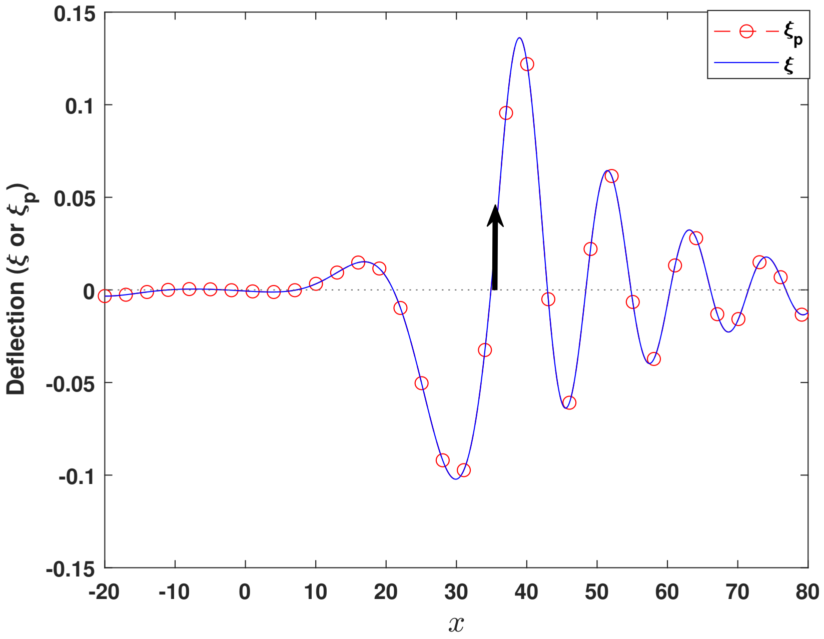

Figure 5.5: Comparison of deflection ξ with ξ_p. The deflection ξ approaches ξ_p as the load frequency Ω, load half-length l_0, and uniform current u_0 tend to zero. The load moves with a speed $c_{\min}$ <7.1 m/s< $\sqrt{gH}$ at time $t = 5$s.

The accuracy and congruence of our formulation with established theoretical predictions are validated by the observation that this limiting scenario closely matches the results published by Hosking and Milinazzo (2022).

It is noted that the highest depression occurs just beneath the load as it moves at $V = 5.5$m/s (Fig. 5.4). As the speed increases (for $V = 7.1$m/s and 9.2m/s) (Figs. 5.5 and 5.6), the location of the maximum depression moves behind the position of the load. Furthermore, the waves behind the load have a longer wavelength, whereas the waves in front of the load have a shorter wavelength. The waves generated behind the load get noticeably longer at supercritical speed ($V > \sqrt{gH}$), and the depression gets wider as the load speed increases (Takizawa (1988)).

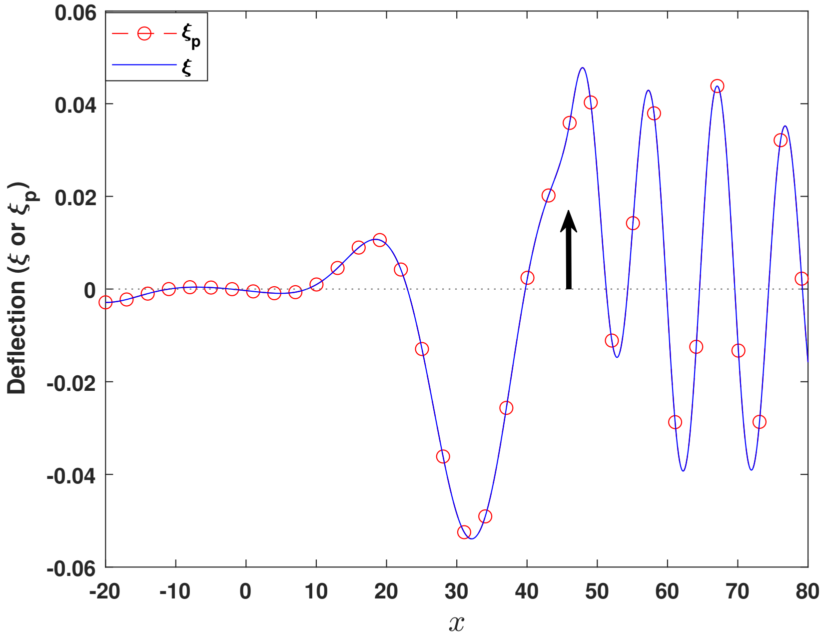

Figure 5.6: Comparison of deflection ξ with ξ_p. The deflection ξ approaches ξ_p as the load frequency Ω, load half-length l_0, and uniform current u_0 tend to zero. The load moves with a speed 9.2 m/s> $\sqrt{gH}$ at time $t = 5$s.

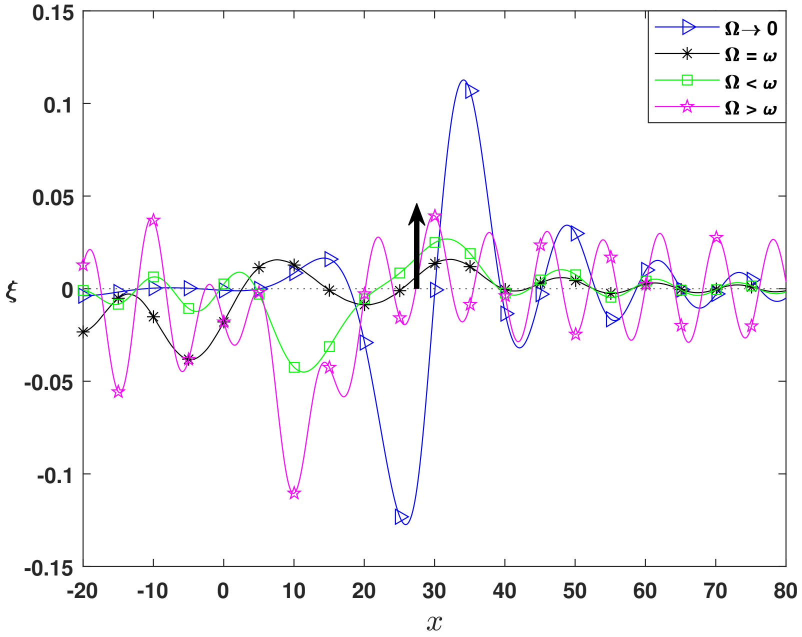

Figure 5.7: The deflection for load speed $V = 5.5$m/s at $t = 5$s corresponding to different cases of load frequency Ω.

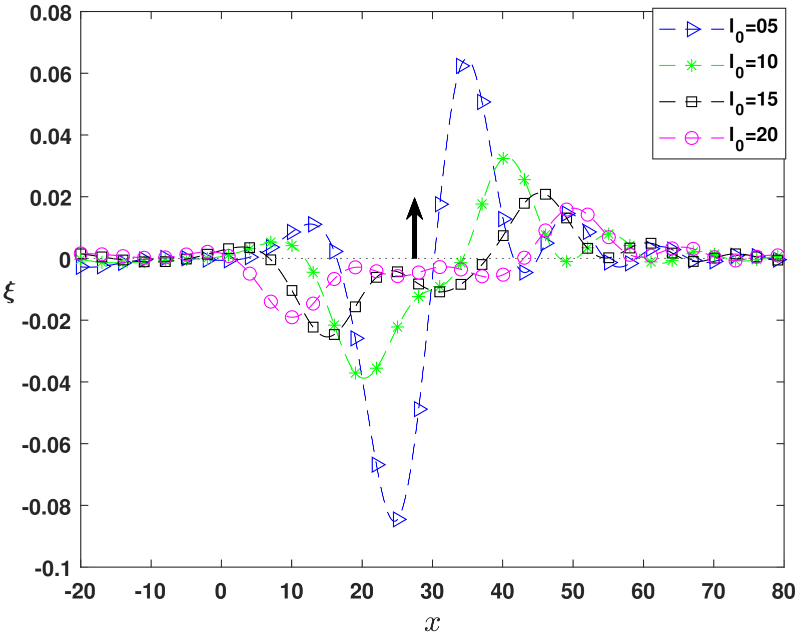

Figure 5.8: The deflection for load speed $V = 5.5$m/s at $t = 5$s corresponding to different values of l_0.

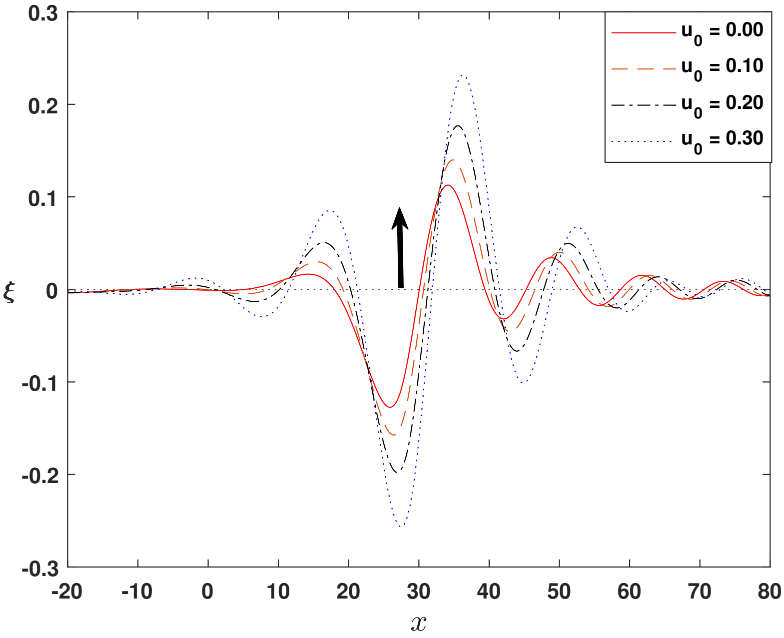

Figure 5.9: The deflection for load speed $V = 5.5$m/s at $t = 5$s corresponding to different values of u_0.

Figure 5.7 illustrates the effect of the load frequency Ω on the generated waves for l_0, $u_0 \to 0$. Three load frequency instances are taken into consideration, which correspond to ω ($\Omega = \omega$, $\Omega < \omega$ and $\Omega > \omega$). When $\Omega > \omega$, the generated waves show a more oscillatory pattern with an almost constant amplitude over distance similar to sinusoidal waves with a constant phase. On the other hand, waves corresponding to $\Omega \leq \omega$ are less oscillatory and decrease in amplitude as the distance from the load increases. This behavior is consistent with the wave-structure interaction theory: when the excitation frequency matches or is lower than the natural frequency, the system releases energy more effectively, resulting in a reduction of the wave amplitude.

It is observed that the maximum deflection, which occurs immediately below the load and moves with it, significantly decreases as the load length increases (Fig. 5.8). Furthermore, the shape of the resulting depression varies: it is narrow when $l_0 \to 0$, following the effect of a concentrated point load, but it expands as $l_0 > 0$ increases. This behavior demonstrates the dispersive nature of the wave response, as well as the role of the distributed load in changing the amplitude and spatial nature of the deflection.

Figure 5.9 illustrates the variation of the deflection profile corresponding to different values of the uniform current u_0 with Ω, $l_0 \to 0$. The changes in the uniform current correlate to variations in the maximum deflection beneath the load. The wave patterns resemble those shown in Fig. 5.4 when there is no uniform current present.

5.3.2 Results for Accelerated and Decelerated Load

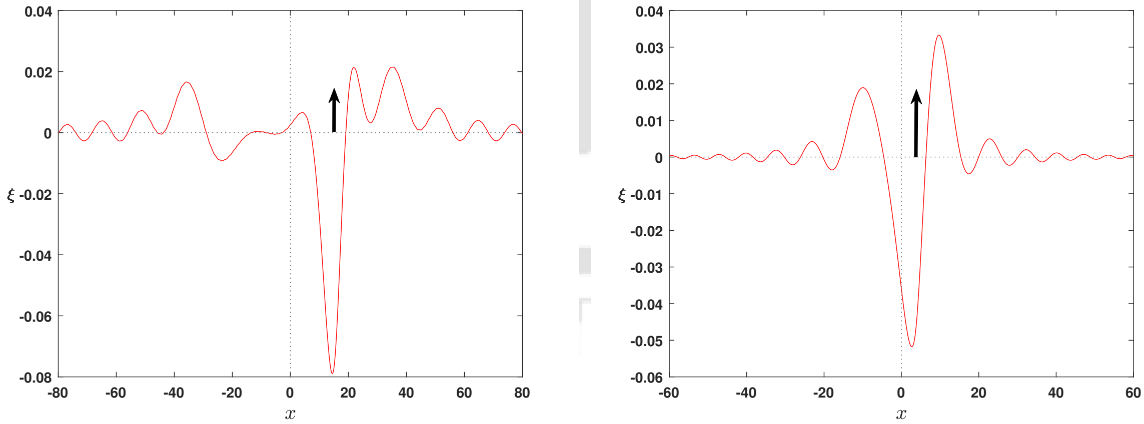

(a) (b)

Figure 5.10: The generated wave pattern for $V = 5.5$m/s due to an impulsively started load with uniform acceleration from $t = 0$: (a) $A = 1\text{m/s}^2$ and $t = 5.5$s, (b) $A = 4\text{m/s}^2$ and $t = 1.375$s.

At starting time $t = 0$, we suppose that the load starts from rest, i.e., $V = 0$. It immediately starts moving with a constant acceleration A. For this instance, $At^2/2$ gives the distance covered by the load. Two constant accelerations taken into consideration are $A = 1\text{m/s}^2$ and $A = 4\text{m/s}^2$.

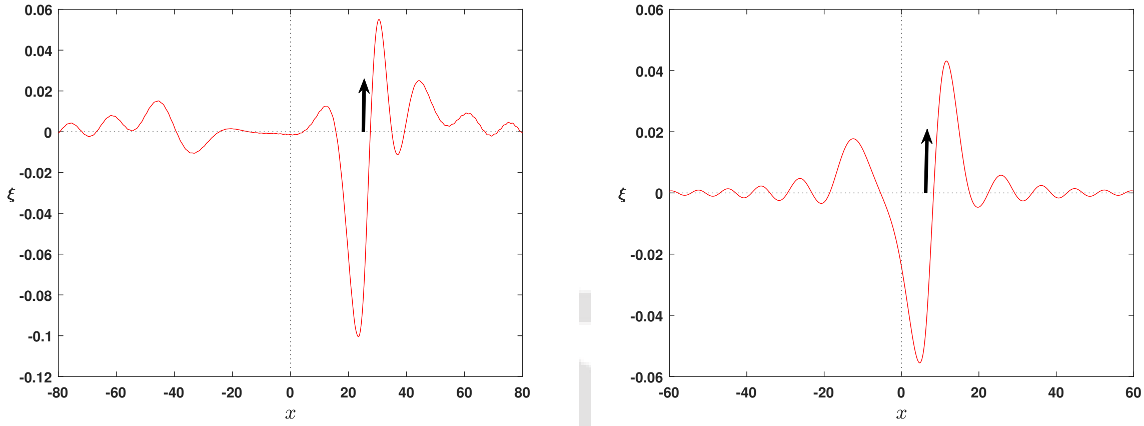

(a) (b)

Figure 5.11: The generated wave pattern for $V = 7.1\text{m/s}$ due to an impulsively started load with uniform acceleration from $t = 0$: (a) $A = 1\text{m/s}^2$ and $t = 7.1\text{s}$, (b) $A = 4\text{m/s}^2$ and $t = 1.775\text{s}$.

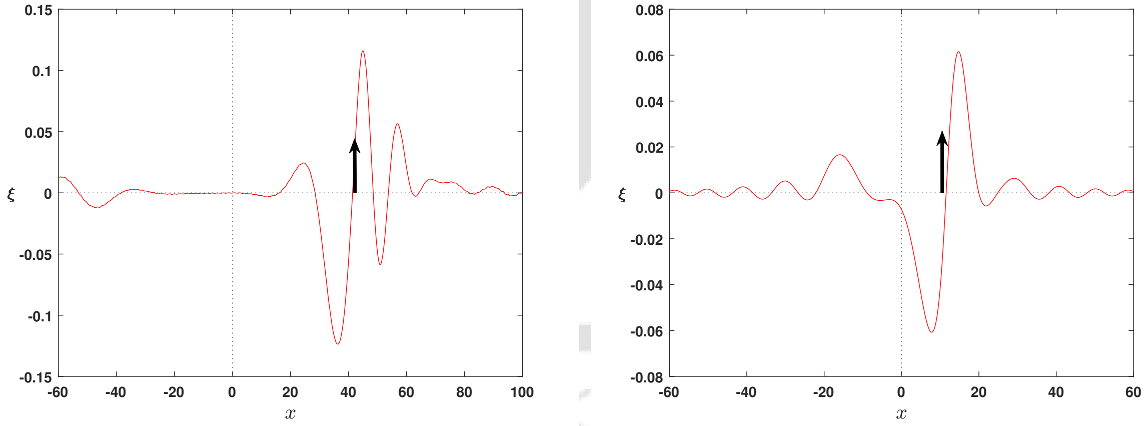

(a) (b)

Figure 5.12: The generated wave pattern for $V = 9.2\text{m/s}$ due to an impulsively started load with uniform acceleration from $t = 0$: (a) $A = 1\text{m/s}^2$ and $t = 9.2\text{s}$, (b) $A = 4\text{m/s}^2$ and $t = 2.3\text{s}$.

Figures 5.10, 5.11, and 5.12 illustrate how these accelerations affect the generated waves when all of l_0, Ω and $u_0 \to 0$. We consider the cases when the load reaches the speed $V = 5.5$, 7.1 and 9.2m/s under the accelerations $A = 1\text{m/s}^2$ and 4m/s^2. When the load moves with a uniform acceleration $A = 1\text{m/s}^2$, it attains the speed regime

$V = 5.5\text{m/s}$ at $t = 5.5\text{s}$. Similarly, at $t = 7.1\text{s}$ and $t = 9.2\text{s}$, it reaches the speed regimes $V = 7.1\text{m/s}$ and $V = 9.2\text{m/s}$, respectively. In the case of higher acceleration $A = 4\text{m/s}^2$, due to the higher rate of velocity change, the corresponding periods required to attain these speed regimes are substantially shorter.

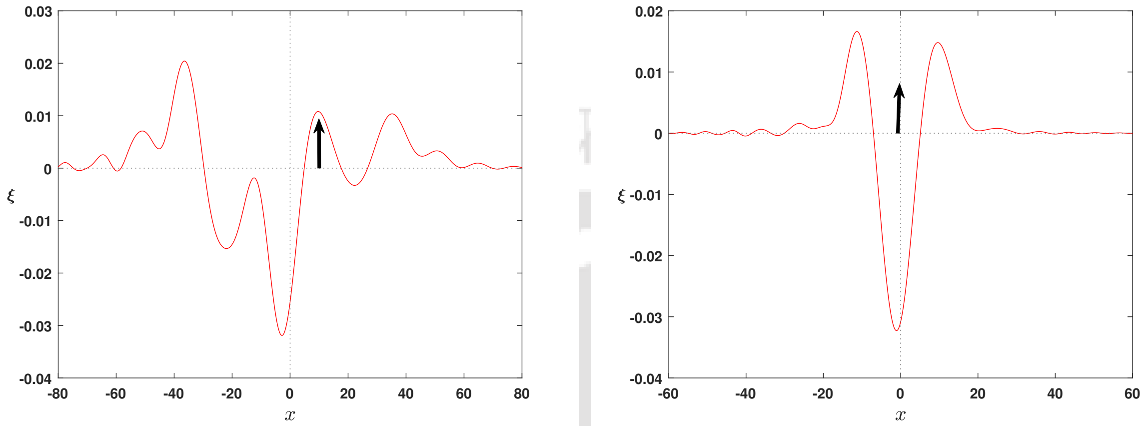

(a) (b)

Figure 5.13: The generated wave pattern for $V = 5.5\text{m/s}$ due to an impulsively started load with uniform acceleration from $t = 0\text{s}$, considering the effects of uniform current u_0, load frequency Ω, and load length l_0: (a) $A = 1\text{m/s}^2$ and $t = 5.51\text{s}$, (b) $A = 4\text{m/s}^2$ and $t = 1.375\text{s}$.

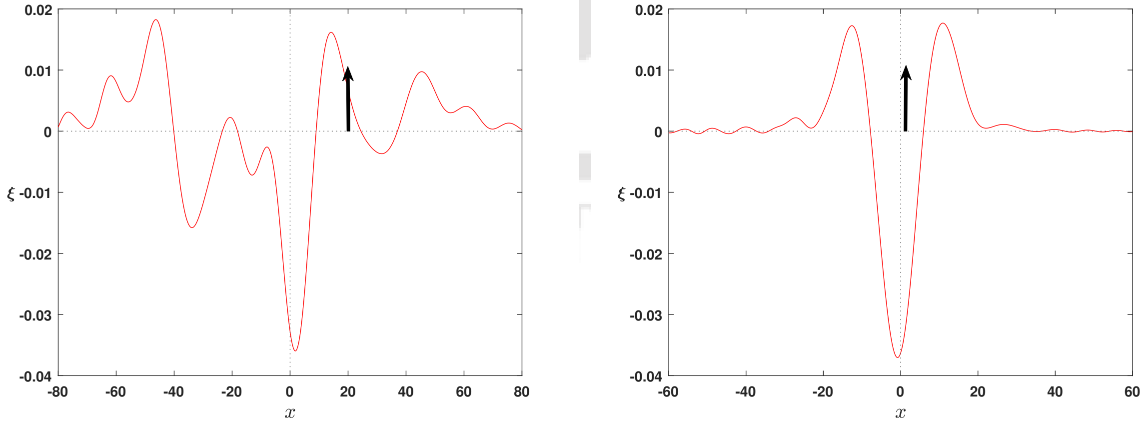

(a) (b)

Figure 5.14: The generated wave pattern for $V = 7.1\text{m/s}$ due to an impulsively started load with uniform acceleration from $t = 0\text{s}$, considering the effects of uniform current u_0, load frequency Ω, and load length l_0: (a) $A = 1\text{m/s}^2$ and $t = 7.1\text{s}$, (b) $A = 4\text{m/s}^2$ and $t = 1.775\text{s}$.

Figure 5.10 depicts the deflection profile of a uniformly accelerated load. For both acceleration instances, the large amplitude observed near the load is consistent with a quasi-static response. Higher acceleration ($A = 4\text{m/s}^2$) results in a wider depression in comparison with lower acceleration ($A = 1\text{m/s}^2$). Moreover, for higher acceleration, the amplitude just beneath the load is smaller compared to that for lower acceleration. Similar types of responses are also observed for speed regimes $V = 7.1\text{m/s}$ and $V = 9.2\text{m/s}$ (Figs. 5.11, 5.12).

Similarly, in Figs. 5.13 ($V = 5.5\text{m/s}$), 5.14 ($V = 7.1\text{m/s}$), and 5.15 ($V = 9.2\text{m/s}$), we study the impacts of load frequency, load length, and uniform current, considering $\Omega < \omega$, $l_0 = 5\text{m}$ and $u_0 = 0.1\text{m/s}$. The findings demonstrate that, when all of these factors are considered, the wave pattern for lower acceleration becomes more disturbed, and for higher acceleration, it remains comparable to a quasi-static condition, with the largest deflection occurring just beneath the load position. However, at lower acceleration, the maximum deflection transfers to a position behind the load across all speed ranges. This shift suggests that wave energy lags the moving load substantially in lower acceleration circumstances, resulting in an unbalanced disturbance profile when compared to higher acceleration conditions.

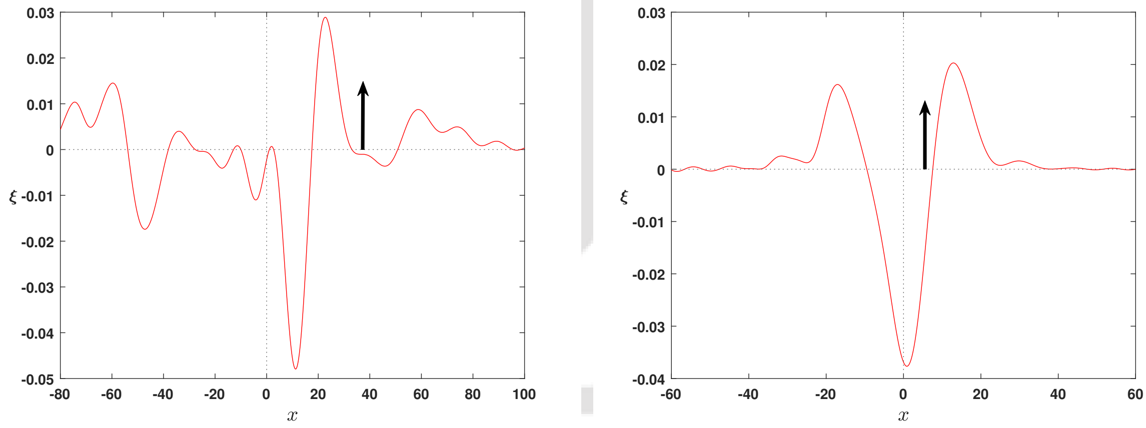

(a) (b)

Figure 5.15: The generated wave pattern for $V = 9.2\text{m/s}$ due to an impulsively started load with uniform acceleration from $t = 0\text{s}$, considering the effects of uniform current u_0, load frequency Ω, and load length l_0: (a) $A = 1\text{m/s}^2$ and $t = 9.2\text{s}$, (b) $A = 4\text{m/s}^2$ and $t = 2.3\text{s}$.

For a constant deceleration ($-A$) from an initial speed V, the position of the load after time t is $x = Vt - At^2/2$. Figures 5.16 and 5.17 illustrate the case of a load starting at a constant supercritical speed of $V = 9.2\text{m/s}(> \sqrt{gH})$ and undergoing a uniform deceleration of $A = -1\,\text{m/s}^2$ until coming to rest at $t = 9.2\text{s}$. For the considered depth of water ($H = 6.8$m), this scenario covers all three response regimes during the deceleration phase. The snapshots corresponding to $t = 2.10$, 4.30, 6.45 and 8.50s are presented.

The initial, predominantly flexural component formed ahead of the decelerating load remains present. However, due to the continuous approach of predominantly gravity waves from behind, its amplitude is eventually surpassed in the vicinity of the load. Notably, the predicted deflection corresponding to a uniformly decelerating load shows no singular behavior during its evolution (Miles and Sneyd (2003)). When the parameter effects (l_0, u_0 and Ω) are taken into account, the trailing waves exhibit greater disturbance due to the oscillatory nature of the load. The maximum deflection is also reduced compared to the case without these parameter influences (Fig. 5.17).

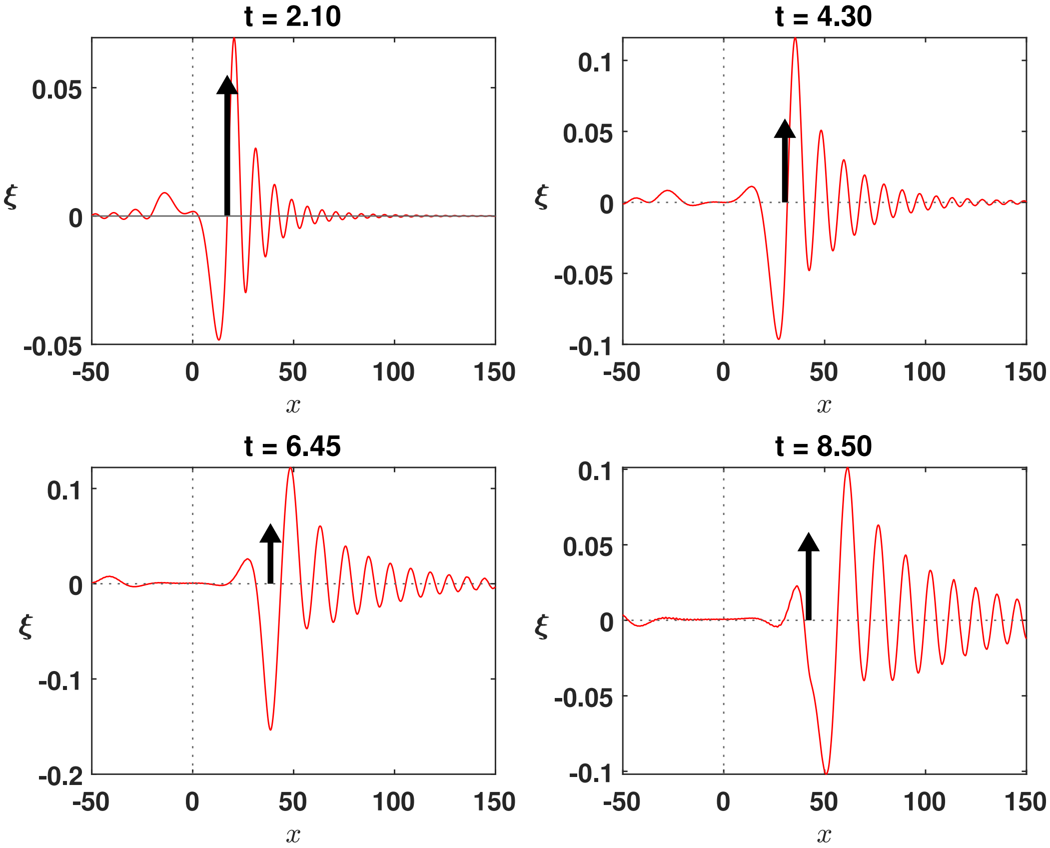

Figure 5.16: Deflection formation for an impulsively starting load decelerating at a constant rate of $A = 1\text{m/s}^2$ and coming to rest from a supercritical initial speed of 9.2m/s with l_0, u_0 and $\Omega \to 0$.

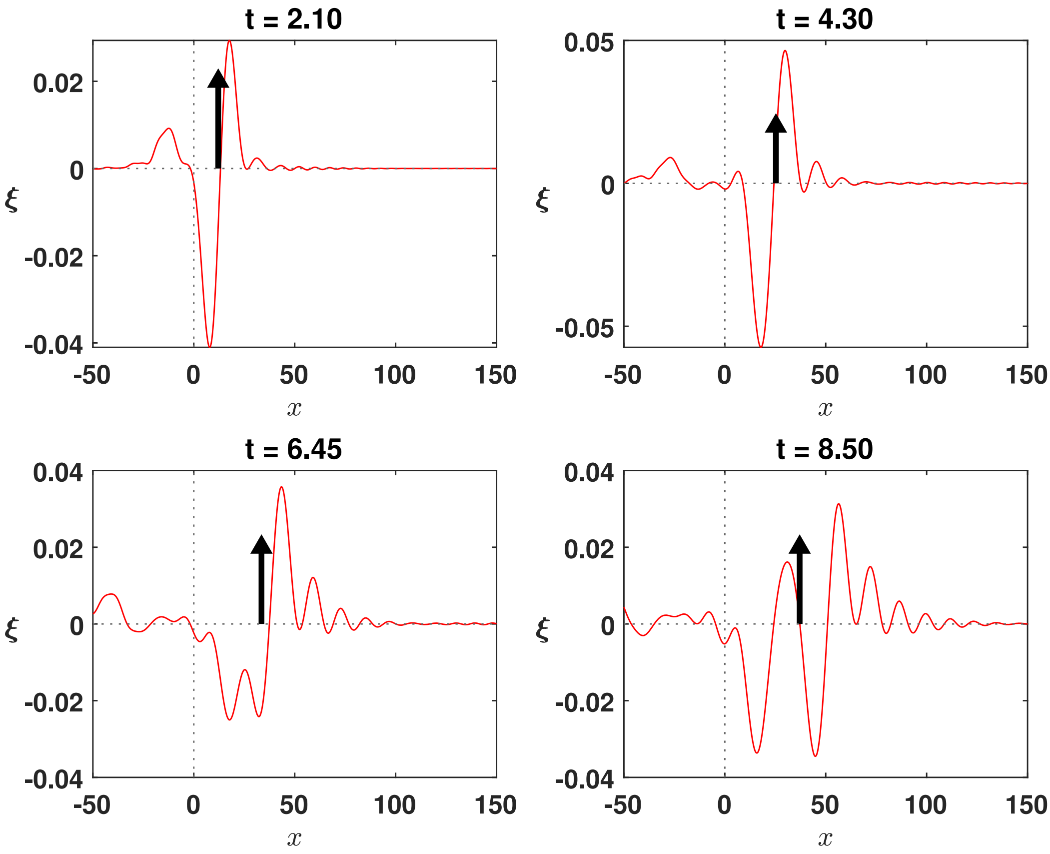

Figure 5.17: Deflection formation for an impulsively starting load decelerating at a constant rate of $A = 1\text{m/s}^2$ and coming to rest from a supercritical initial speed of 9.2m/s with $l_0 = 05\text{m}$, $u_0 = 0.1\text{m/s}$ and $\Omega < \omega$.

5.4 Conclusions

We propose a mathematical model to study the wave response of a thin floating ice sheet under a moving load in the presence of a uniform underlying current. A set of linear partial differential equations describes the corresponding physical scenario. It is taken into consideration that the external force is distributed over the finite length on the ice sheet and is harmonic in time. Additionally, the load moves with a variable speed, which introduces additional complexity to the analysis. To solve this system, we employ the Laplace-Fourier transform technique. The load moves at a variable speed; in order to account for this, we explore various scenarios, such as when the load moves at constant speed with or without uniform acceleration/deceleration. Inverse Laplace-Fourier transform is employed to obtain the final expression for the ice sheet deflection, which is obtained in an integral form.

The maximum deflection occurs directly beneath the moving load. The resulting depression has a narrow shape in low-speed regimes. The depression increases and starts to lag behind the position of the load as the load velocity increases. Longer waves appear on the back side of the load, whereas shorter waves appear in front of it. This behavior strongly demonstrates that the wave patterns depend on load speed.

It is observed that the generated waves show a more oscillatory pattern with an almost constant amplitude over distance similar to sinusoidal waves with a constant phase when $\Omega > \omega$. On the other hand, waves corresponding to $\Omega \leq \omega$ are less oscillatory and decrease in amplitude as the distance from the load increases. Both the amplitude and the spatial distribution of the deflection of the ice sheet are significantly impacted by the load frequency.

The maximum deflection significantly decreases as the load length increases significantly. This suggests that a larger spatial distribution of the load results in a more uniform distribution of applied forces within the structure, which in turn reduces the localized concentrations of stress, strain, and bending and eventually increases the structural durability. The changes in the uniform current correlate with the variations in the maximum deflection beneath the load. The wave patterns look similar to the case when there is no uniform current present.

The deflection caused by a uniformly accelerating line load is also found to remain consistently regular throughout the motion. The findings demonstrate that, when all of these factors (Ω, u_0 and l_0) are considered, the wave pattern for lower acceleration becomes more disturbed, and for higher acceleration, it remains comparable to a quasi-static condition, with the largest deflection occurring just beneath the load position.

An initially impulsively started load is taken into consideration when examining the response to a uniformly decelerating load. The initial, predominantly flexural component formed ahead of the decelerating load remains present, but its amplitude is eventually surpassed near the load due to the continuous approach of the predominantly gravity waves from behind. We also observe that, when the effects of loading frequency, uniform current, and load length are taken into account, the load amplitude is found to be lower for both uniformly accelerating and decelerating loads, compared with the case without considering these parameters.

The observations from this study provide important information on various aspects: (a) the behavior of a floating ice sheet under a distributed time-dependent moving line load, (b) the effect of a uniform current, and (c) the effect of load frequency on the deflection of the ice sheet due to a moving load.

CHAPTER 6

Impact of sea-bed trench on the deflection of a floating ice sheet due to a moving load

6.1 Mathematical Formulation

We consider the two-dimensional propagation of linear water waves over a rectangular trench of width L where the water depths before and after the trench are constant and equal. We consider an infinitely long ice sheet with homogeneous properties. The ice sheet thickness is h and density is ρ_i. Additionally, the ice sheet is modeled as a thin elastic plate since its thickness is much smaller than its horizontal dimensions, allowing the use of the thin plate theory (Milinazzo et al. (1995)). The contact between the plate and the water is represented by $z = 0$, with the z-axis pointing vertically upward. The depth of the sea is considered as $z = -H_1$ excluding the trench, which has a depth $z = -H_2$. The fluid is assumed to be homogeneous, inviscid and incompressible, experiencing irrotational motion, with a constant density represented by ρ. Therefore, the velocity potential function $\Phi(x, z, t)$ satisfies the Laplace's equation

$$\begin{gathered}\Phi_{xx} + \Phi_{zz} = 0, \ -\infty < x < 0, \ -H_1 \leq z \leq 0; \ 0 \leq x \leq L, \ -H_2 \leq z \leq 0; \\ L < x < \infty, \ -H_1 \leq z \leq 0. \end{gathered} \tag{6.1}$$

The kinematic boundary conditions and the bending equation of the ice sheet (dynamic condition) are applied at $z = 0$ (Davys et al. (1985)). Thus, the conditions at $z = 0$ are

$$\Phi_z = \xi_t, \tag{6.2}$$

$$D\nabla^4\xi + \rho_i h \xi_{tt} = p - f(x, t), \tag{6.3}$$

where ξ is the small vertical ice displacement, $D = \dfrac{Eh^3}{12(1-\nu^2)}$ denotes the effective flexural rigidity of the plate with Young's modulus E and Poisson's ratio ν, p is the pressure of water at $z = 0$, $f(x,t)$ denotes the external force applied to the ice sheet.

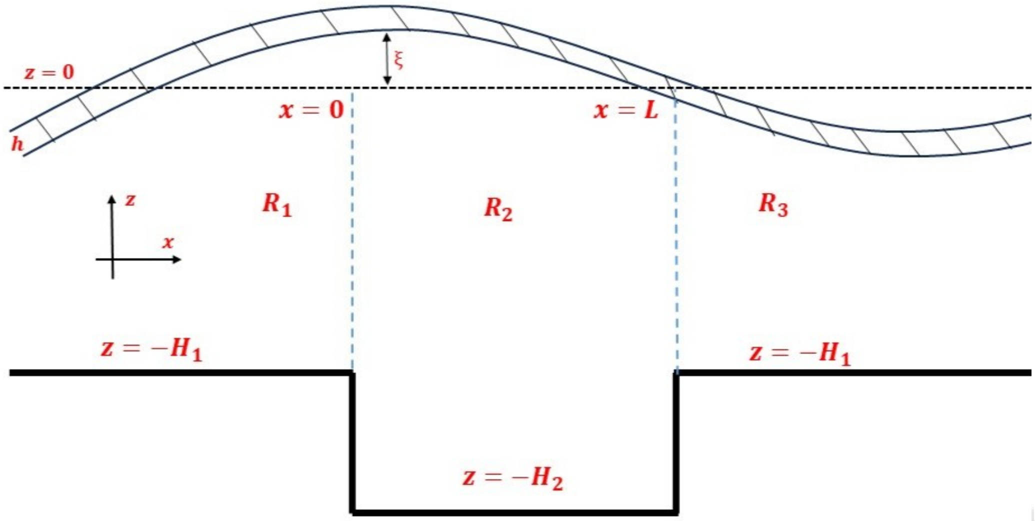

Figure 6.1: Sketch of the problem in the framework of a sea-ice sheet over a rectangular shaped trench.

A simplified Bernoulli pressure equation is used to describe the interaction between the plate and the water, assuming an implicit non-cavitation criterion at the ice-water contact. Therefore, Bernoulli's equation is

$$p = -\rho g\xi - \rho\Phi_t \quad \text{at} \quad z = 0. \tag{6.4}$$

Thus, from Eqs. (6.3) and (6.4), we can write

$$D\nabla^4\xi + \rho g\xi + \rho\Phi_t = -f(x,t);\ t \geq 0\ , -\infty < x < \infty. \tag{6.5}$$

In Eq. (6.5), the term $\rho_i h\xi_{tt}$ is left out since we focus on waves with significantly large wavelengths as compared with the ice thickness. The motion in such long waves penetrates the fluid to a depth determined by the wavelength, which is usually much more than the thickness of the plate and frequently equal to the depth of the fluid. As a result, the underlying inertia of fluid predominates, with the exception of very short waves, rendering the inertia of plate contribution negligible.

The visual representation of the problem is shown in Fig. 6.1. The sea-bed has a rectangular-shaped trench. Based on this, we divide the fluid region vertically into three virtual regions. The middle region corresponds to the trench, while the regions on either side of it have equal fluid depth. The fluid regions are indicated as follows:

$$R_1 \ :\ -H_1 \leq z \leq 0\ ;\ -\infty < x < 0,$$

$$R_2 \;:\; -H_2 \leq z \leq 0\,;\; 0 \leq x \leq L,$$
$$R_3 \;:\; -H_1 \leq z \leq 0\,;\; L < x < \infty.$$

Accordingly, the velocity potentials in each region R_j are represented by the notation Φ_j, $j = 1, 2, 3$, respectively. Likewise, the ice sheet deflection in each region is represented by ξ_j. Based on the division of the fluid region, we now rewrite the equations accordingly as follows:

$$\Phi_{jxx} + \Phi_{jzz} = 0 \quad \text{in} \quad R_j,\, j = 1, 2, 3, \tag{6.6}$$
$$\Phi_{jz} = \xi_{jt} \quad \text{at} \quad z = 0, \tag{6.7}$$
$$D\nabla^4 \xi_j + \rho g \xi_j + \rho \Phi_{jt} = -f(x,t) \quad \text{at} \quad z = 0. \tag{6.8}$$

Under the present circumstances, the bottom conditions are as follows:

$$\Phi_{1z} = 0 \quad \text{at} \quad z = -H_1,\; -\infty < x < 0, \tag{6.9a}$$
$$\Phi_{2z} = 0 \quad \text{at} \quad z = -H_2,\; 0 \leq x \leq L, \tag{6.9b}$$
$$\Phi_{3z} = 0 \quad \text{at} \quad z = -H_1,\; L < x < \infty. \tag{6.9c}$$

The matching conditions on the common virtual boundary due to the continuity of the pressure and mass flux are given by

$$\Phi_1 = \Phi_2 \quad \text{at} \quad x = 0,\; -H_1 < z < 0, \tag{6.10a}$$
$$\Phi_{1x} = \Phi_{2x} \quad \text{at} \quad x = 0,\; -H_1 < z < 0, \tag{6.10b}$$
$$\Phi_2 = \Phi_3 \quad \text{at} \quad x = L,\; -H_1 < z < 0, \tag{6.10c}$$
$$\Phi_{2x} = \Phi_{3x} \quad \text{at} \quad x = L,\; -H_1 < z < 0. \tag{6.10d}$$

The vanishing of the horizontal velocity on the rigid vertical sides of the trench implies the following condition at $x = 0$ and $x = L$:

$$\Phi_{2x} = 0, \quad -H_2 \leq z \leq -H_1. \tag{6.11}$$

In addition, Φ_j's must satisfy the edge condition: $r^{1/3}\nabla\Phi_j$ $(j = 1, 2, 3)$ is bounded as $r \to 0$, where r is the distance from the submerged edges of the trench.

Our aim is to determine the deflection of the ice sheet given by

$$\xi(x,t) = \begin{cases} \xi_1, & x \in R_1, \\ \xi_2, & x \in R_2, \\ \xi_3, & x \in R_3. \end{cases} \tag{6.12}$$

Since the fluid region is divided into three regions, the velocity potentials in neighboring regions must satisfy the continuity of pressure and mass flux at each internal boundary (Eqs. (6.10a)-(6.10d)). According to these continuity requirements, the fluid motion cannot abruptly jump across the interface. As a result, the plate deflection ξ must also remain smooth at the boundary between the regions, i.e.,

$$\xi_1(0,t) = \xi_2(0,t) \quad \text{and} \quad \xi_2(L,t) = \xi_3(L,t). \tag{6.13}$$

Furthermore, the continuity of mass flux (Eqs. (6.10b), (6.10d)) across the interface, combined with the kinematic condition, enforces continuity of the slope of the ice sheet. In terms of mechanics, the horizontal fluid velocity must stay continuous across the internal boundary; any disruption in this velocity field would cause the plate to abruptly bend. Therefore, we have

$$\xi_{1x}(0,t) = \xi_{2x}(0,t) \quad \text{and} \quad \xi_{2x}(L,t) = \xi_{3x}(L,t). \tag{6.14}$$

Along with the continuity of deflection and slope, the interface must also satisfy continuity of bending moment and shear force. As the bending moment and shear force are dependent on the second and third derivatives of the deflection, any discontinuity would indicate an unphysical rotational or transverse pressure at the interface. As a result, both must be continuous to ensure smooth and physically consistent plate deformation. Thus, we have

$$\xi_{1xx}(0,t) = \xi_{2xx}(0,t) \quad \text{and} \quad \xi_{2xx}(L,t) = \xi_{3xx}(L,t), \tag{6.15}$$

$$\xi_{1xxx}(0,t) = \xi_{2xxx}(0,t) \quad \text{and} \quad \xi_{2xxx}(L,t) = \xi_{3xxx}(L,t). \tag{6.16}$$

The plate deformation is smooth and dynamically consistent with the fluid response throughout all regions because of the continuity of deflection (Eq. (6.13)), slope (Eq. (6.14)), bending moment (Eq. (6.15)), and shear force (Eq. (6.16)).

For this purpose, we use the plan wave approximation theory (Kirby and Dalrymple (1983)), and solve Eqs. (6.6)-(6.8) by using the appropriate bottom boundary conditions corresponding to the fluid regions. Therefore, we obtain the following equations:

$$D\nabla^4\xi_j + \rho g \xi_j + \frac{\rho}{k_1}\coth(k_1 H_1)\xi_{jtt} = -f(x,t), \quad j = 1,3, \tag{6.17}$$

$$D\nabla^4\xi_2 + \rho g \xi_2 + \frac{\rho}{k_2}\coth(k_2 H_2)\xi_{2tt} = -f(x,t). \tag{6.18}$$

The dispersion relation provides the relationship among the wavenumber, fluid depth, and angular frequency, which is written as

$$\omega^2 = \left(\frac{Dk_j^4}{\rho} + g\right) k_j \tanh(k_j H_j), \quad j = 1,2. \tag{6.19}$$

The phase speed and group speed of waves are given, respectively, by

$$c = \frac{\omega}{k_j} \quad \text{and} \quad c_g = \frac{d\omega}{dk_j}; \quad j = 1,2. \tag{6.20}$$

For shallow-water scenarios where the water depth is considerably smaller than the wavelength, the linear form of the hyperbolic tangent term in the dispersion relation can be used to approximate it as $\tanh(k_j H_j) \approx k_j H_j$. Substituting this approximation in Eq. (6.19) yields the shallow-water dispersion relation

$$\omega^2 = \left(\frac{Dk_j^4}{\rho} + g\right) k_j^2 H_j, \quad j = 1, 2. \tag{6.21}$$

The above equation demonstrates that the flexural rigidity term D continues to affect the wave dynamics even in shallow water, whereas its effect on the water depth H_j becomes noticeable.

Using the above dispersion relation, the corresponding phase speed is obtained as

$$c^2 = H_j \left(\frac{Dk_j^3}{\rho} + \frac{g}{k_j}\right). \tag{6.22}$$

The group speed is given by

$$c_g = \frac{k_j H_j}{\omega} \left[\frac{3Dk_j^4}{\rho} + g\right]. \tag{6.23}$$

For deep-water scenarios when the water depth is much greater than the wavelength, the hyperbolic tangent term in the dispersion relation becomes $\tanh(k_j H_j) \approx 1$. Therefore, Eq. (6.19) takes the form

$$\omega^2 = \left(\frac{Dk_j^5}{\rho} + gk_j\right). \tag{6.24}$$

Furthermore, the phase and group speed are given, respectively, by

$$c = \sqrt{\frac{Dk_j^3}{\rho} + \frac{g}{k_j}} \quad \text{and} \quad c_g = \frac{1}{2\omega} \left[\frac{5Dk_j^4}{\rho} + g\right]. \tag{6.25}$$

6.2 Method of Solution

We consider a concentrated point load that travels in the positive x-direction with a constant speed V. Although the load acts only at the instantaneous position of the moving point, the associated loading function is expressed as $f(x,t) = F_0\,\delta(x - Vt)$, which represents a load of magnitude F_0 applied at the position $x = Vt$ at time t, where $\delta(.)$ is the Dirac delta function.

Since the sea-bed has a trench-like shape, the moving load is assumed to act only in Region 2, which represents the trench. Hence, the loading function term $f(x,t) = 0$ in Regions 1 and 3. For Region 2, we consider a concentrated point load that moves with a constant speed V from left to right over the ice sheet. A steady-state solution is conceivable if the motion of the coupled system seems motionless to an observer moving with the load. An observer moving with the load can describe the motion of the system using a relative variable $X = x - Vt$, where x corresponds to a fixed coordinate. A steady-state solution can be found by simplifying the problem to a steady-state situation by introducing this new coordinate system. Therefore, the functions are rewritten as

$$\xi(x,t) = \xi(X), \;\; f(x,t) = f(X), \tag{6.26}$$

where $\xi(X)$ and $f(X)$ represent the coordinate transformation of ice deflection, and external force relative to the moving load, respectively. Therefore, the initial partial derivative operators are ordinary as follows:

$$\frac{\partial}{\partial x} = \frac{d}{dX}, \; \frac{\partial}{\partial t} = -V\frac{d}{dX}.$$

Therefore, we write Eqs. (6.17) and (6.18) in the new coordinate system as follows:

$$\frac{d^4\xi_j}{dX^4} + 4r_1^2\frac{d^2\xi_j}{dX^2} + 4r_3^4\xi_j = 0, \quad j = 1, 3, \tag{6.27}$$

$$\frac{d^4\xi_2}{dX^4} + 4r_2^2\frac{d^2\xi_2}{dX^2} + 4r_3^4\xi_j = -\frac{f(X)}{D}, \tag{6.28}$$

where

$$4r_1^2 = \frac{\rho V^2}{Dk_1}\coth(k_1H_1), \quad 4r_2^2 = \frac{\rho V^2}{Dk_2}\coth(k_2H_2), \quad 4r_3^4 = \frac{\rho g}{D}, \quad f(X) = F_0\delta(X). \tag{6.29}$$

Let us assume $\xi_j = e^{\gamma X}$ to be solutions of Eq. (6.27). Therefore, the auxiliary equation is

$$\gamma^4 + 4r_1^2\gamma^2 + 4r_3^4 = 0 \quad \text{for} \quad j = 1, 3. \tag{6.30}$$

This auxiliary equation has four roots, given by

$$\gamma_{1,2,3,4} = \pm\sqrt{-2\left(r_1^2 \mp \sqrt{(r_1^4 - r_3^4)}\right)}. \tag{6.31}$$

Since $r_1^4 - r_3^4 = (r_1^2 + r_3^2)(r_1^2 - r_3^2)$, the nature of the roots is dependent on the sign of $(r_1^2 - r_3^2)$. This is the general algebraic form; we now provide more straightforward, concrete forms in the three scenarios that depend on the sign of $(r_1^2 - r_3^2)$.

Case 1:- When $r_1^2 < r_3^2$,

$$V^2 < \left(\frac{4Dg}{\rho}\right)^{1/2} k_1\tanh(k_1H_1). \tag{6.32}$$

In this context, the roots of the auxiliary equation become complex conjugates.

Case 2:- When $r_1^2 = r_3^2$,

$$V^2 = \left(\frac{4Dg}{\rho}\right)^{1/2} k_1\tanh(k_1H_1). \tag{6.33}$$

In this case, the auxiliary equation yields repeated purely imaginary roots.
Case 3:- When $r_1^2 > r_3^2$,

$$V^2 > \left(\frac{4Dg}{\rho}\right)^{1/2} k_1 \tanh(k_1 H_1). \tag{6.34}$$

In this case, the auxiliary equation admits purely imaginary roots (not repeated), indicating oscillatory behavior of the solution.
The same analysis applies to Region 2 upon replacing k_1 by k_2 and H_1 by H_2.

For **Case 1**, the roots of Eq. (6.30) are complex conjugates given by

$$\gamma_{1,2,3,4} = \pm s_1 \pm \mathrm{i} s_2,$$

where $s_1 = \sqrt{r_3^2 - r_1^2}$ and $s_2 = \sqrt{r_1^2 + r_3^2}$. Thus, the general solution of Eq. (6.27) can be found in the following manner.

We add the condition that the solution to Eq. (6.27) must remain bounded as $X \to \pm\infty$. From a physical point of view, this condition guarantees that the deflection of the ice sheet does not expand rapidly away from the area of applied load or disturbance. As a result, the displacement must disappear as $X \to -\infty$ in Region 1 and as $X \to +\infty$ in Region 3. These assumptions lead to the following solutions:

$$\xi_1(X) = e^{s_1 X}(B_1 \cos(s_2 X) + B_2 \sin(s_2 X)), \quad -\infty < X < -Vt, \tag{6.35}$$
$$\xi_3(X) = e^{-s_1 X}(B_{11} \cos(s_2 X) + B_{12} \sin(s_2 X)), \quad L - Vt < X < +\infty. \tag{6.36}$$

In a similar manner, we solve Eq. (6.28) for Region 2. The simplest approach to solve Eq. (6.28) is to first put the right-hand side equal to zero and find the homogeneous solution. Furthermore, the effect of the concentrated point load may be included by applying the appropriate matching conditions to the position of the load, i.e., $X = 0$. Thus, the solution in Region 2 is

$$\xi_2(X) = \begin{cases} \xi_2^-, & X < 0, \\ \xi_2^+, & X \geq 0, \end{cases} \tag{6.37}$$

where

$$\xi_2^- = e^{s_3 X}(B_3 \cos(s_4 X) + B_4 \sin(s_4 X)) + e^{-s_3 X}(B_5 \cos(s_4 X) + B_6 \sin(s_4 X)), \tag{6.38}$$
$$\xi_2^+ = e^{s_3 X}(B_7 \cos(s_4 X) + B_8 \sin(s_4 X)) + e^{-s_3 X}(B_9 \cos(s_4 X) + B_{10} \sin(s_4 X)), \tag{6.39}$$

with $s_3 = \sqrt{r_3^2 - r_1^2}$ and $s_4 = \sqrt{r_1^2 + r_3^2}$. Here, ξ_2^- represents the solution in the region behind the load, and ξ_2^+ represents the solution in the region ahead of the load. It can be seen that there are a total of 12 unknowns (B_j; $j = 1, 2, \ldots, 12.$) in Eqs. (6.35) to (6.39).

To ensure the structural integrity of the system, we consider a continuous ice sheet with smooth deflection. To preserve continuity, the bending behavior of the ice sheet must transition smoothly between the surfaces, ensuring that forces and deformations are distributed uniformly. This indicates that, at the edges of the trench, the continuity conditions for displacement, slope, bending moments, and shear forces must be satisfied. These constraints prevent no abrupt changes in the deflection profile, slope, or internal stresses, resulting in a physically realistic and stable design. The governing equations for these continuity conditions at $X = -Vt$ are

$$\xi_1 = \xi_2^-, \quad \xi_1' = (\xi_2^-)', \quad \xi_1'' = (\xi_2^-)'', \quad \xi_1''' = (\xi_2^-)''', \tag{6.40}$$

and at $X = L - Vt$, they are

$$\xi_2^+ = \xi_3, \quad (\xi_2^+)' = \xi_3', \quad (\xi_2^+)'' = \xi_3'' \quad (\xi_2^+)''' = \xi_3'''. \tag{6.41}$$

Furthermore, conditions at the position of the load, i.e., at $X = 0$ are

$$\xi_2^- = \xi_2^+, \quad (\xi_2^-)' = (\xi_2^+)', \quad (\xi_2^-)'' = (\xi_2^+)'', \quad (\xi_2^+)''' - (\xi_2^-)''' = -\frac{F_0}{D}. \tag{6.42}$$

The third derivative jump condition in Eq. (6.42) physically represents how a mechanical structure reacts instantaneously to a concentrated force; the displacement is smooth, but the internal shear force jumps, indicating the localized movement of the load through the beam or plate.

There are 12 linear equations for the 12 unknown coefficients:

$$\mathbf{Q} = [B_1 \quad B_2 \quad B_3 \quad B_4 \quad B_5 \quad B_6 \quad B_7 \quad B_8 \quad B_9 \quad B_{10} \quad B_{11} \quad B_{12}]^T.$$

Each interface condition can be written in the general linear form as

$$\sum_{j=1}^{12} \mathcal{m}_{ij}\, \mathbf{Q}_j = q_i, \qquad i = 1, 2, \ldots, 12, \tag{6.43}$$

where $\mathcal{m}_{ij}$ are the coefficients obtained from Eqs. (6.40) to (6.42) and $\mathbf{q}_i$ is the right-hand-side vector corresponding to the forcing term. For this problem, all $q_i = 0$ except for the equation representing the jump in the third derivative at $X = 0$, which gives $q_i = -F_0/D$. Thus, the system of equations can be expressed in the matrix form as

$$\mathcal{m}\, \mathbf{Q} = \mathbf{q}, \tag{6.44}$$

where $\mathcal{m}$ is a 12×12 matrix containing combinations of cosine, sine and exponential functions evaluated at the interface points $X = -Vt,\ 0,\ L - Vt$. The right-hand side vector $\mathbf{q}$ is given by

$$\mathbf{q} = \begin{bmatrix} 0 & 0 & \cdots & 0 & -F_0/D & 0 & \cdots & 0 \end{bmatrix}^T.$$

The unknown coefficients can then be determined by solving

$$\mathbf{Q} = \mathcal{M}^{-1}\mathbf{q}. \tag{6.45}$$

Once $\mathbf{Q}$ is obtained, substitution into the corresponding expressions for ξ_1, ξ_2^-, ξ_2^+, and ξ_3 yields the complete piecewise solution ξ that satisfies all boundary and continuity conditions.

For **Case 2**, the solution is oscillatory (since the roots are on the imaginary axis and are repeated), but not entirely bounded oscillation. The solution is composed of cosine and sine terms modulated by X. Therefore, the increase in amplitude happen linearly with $|X|$. As $X \to \pm\infty$, the solution can increase without limitation (algebraic growth). That is, we can say that, for

$$V = \sqrt{\left(\frac{4Dg}{\rho}\right)^{1/2} k_1 \tanh(k_1 H_1)} = v_k \, (say), \tag{6.46}$$

the deflection grows.

For **Case 3**, the auxiliary equation has purely imaginary roots, i.e., $\gamma_{1,2,3,4} = \pm i s_5, \pm i s_6$, where $s_5 = \sqrt{r_1^2 + r_3^2} - \sqrt{r_1^2 - r_3^2}$ and $s_6 = \sqrt{r_1^2 + r_3^2} + \sqrt{r_1^2 - r_3^2}$. In the absence of the real part, the solution only contains sine and cosine terms. Thus, we can write

$$\xi_1 = C_1 \cos(s_5 X) + C_2 \sin(s_5 X) + C_3 \cos(s_6 X) + C_4 \sin(s_6 X), \tag{6.47}$$

$$\xi_3 = C_{13} \cos(s_5 X) + C_{14} \sin(s_5 X) + C_{15} \cos(s_6 X) + C_{16} \sin(s_6 X). \tag{6.48}$$

The deflections at $X \to \pm\infty$ do not decay to zero, and it becomes clear that, for **Case 3**, the assumed steady-state response cannot be achieved, because harmonic waves propagate left and right, resulting in $\xi \not\to 0$ as $X \to \pm\infty$. Similarly, for Region 2, the solution is given by

$$\xi_2 = \begin{cases} \xi_2^-, & X < 0, \\ \xi_2^+, & X \geq 0, \end{cases} \tag{6.49}$$

where

$$\xi_2^- = C_5 \cos(s_7 X) + C_6 \sin(s_7 X) + C_7 \cos(s_8 X) + C_8 \sin(s_8 X), \tag{6.50}$$

$$\xi_2^+ = C_9 \cos(s_7 X) + C_{10} \sin(s_7 X) + C_{11} \cos(s_8 X) + C_{12} \sin(s_8 X), \tag{6.51}$$

with $s_7 = \sqrt{r_2^2 + r_3^2} + \sqrt{r_2^2 - r_3^2}$ and $s_8 = \sqrt{r_2^2 + r_3^2} - \sqrt{r_2^2 - r_3^2}$. There are sixteen unknowns $(C_1, C_2, \ldots, C_{16})$. The boundary conditions at the virtual boundaries $X = -Vt$ and $X = L - Vt$, along with conditions at the load position $X = 0$ (as shown in Eqs. (6.40)–(6.42)), yield twelve equations. The system is undetermined since there are more unknowns than the number of equations. As a result, these boundary conditions alone cannot be used to uniquely identify the values of all sixteen constants.

6.3 Numerical Results

The process outlined in the previous section is used to evaluate each parameter numerically. The deflection profile of the ice sheet and the unknown coefficients are computed using the following physical parameter values Takizawa (1985): $E = 5.1 \times 10^8\,\mathrm{N/m^2}$, $\nu = 1/3$, $h = 0.18\,\mathrm{m}$, $\rho = 1000\,\mathrm{kg/m^3}$, $\rho_i = 947\,\mathrm{kg/m^3}$, $g = 9.8\,\mathrm{m/s^2}$, $H_1 = 6.8\,\mathrm{m}$ and $t = 5\mathrm{s}$.

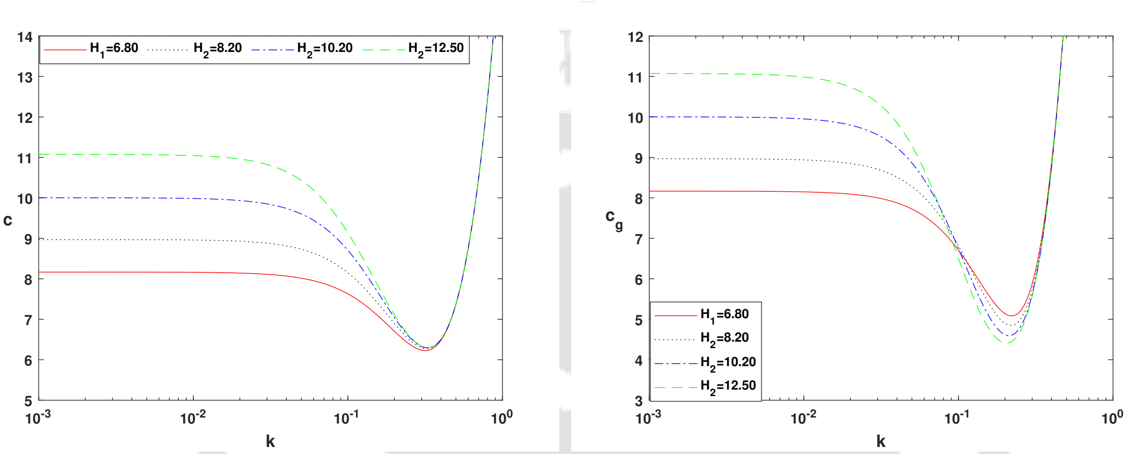

(a) (b)

Figure 6.2: Phase and group speeds variation with wavenumber for different water depths. The wavenumber axis is presented on a logarithmic scale. (a) phase speed, (b) group speed.

The phase speed and group speed variations as functions of the wavenumber k for various water depths are shown in Fig. 6.2. Long waves show non-dispersive behavior in Fig. 6.2(a), where the phase speed is almost constant in the low-wavenumber domain. The significant impact of long-wave propagation on depth is demonstrated for this regime, where an increase in water depth leads to a higher phase speed. Dispersive effects become noticeable as the wavenumber increases, and the phase speed decreases until it reaches a minimum at intermediate values of k. The phase speed increases rapidly at higher wavenumbers, and the curves corresponding to various depths tend to align, indicating that water depth has less of an impact on short-wave propagation.

For the group speed, Fig. 6.2(b) displays a similar overall pattern. The group speed is almost constant at small wavenumbers and increases with water depth, indicating faster energy transmission in more deep water. Figure 6.3 shows that, under shallow-water conditions, both phase and group speeds for long waves are substantially independent of the wavenumber and are mainly affected by the water depth. These findings clearly demonstrate the difference between shallow-water and intermediate/deep-water wave dynamics. The phase and group speeds remain almost constant over a broad range of wavenumbers,

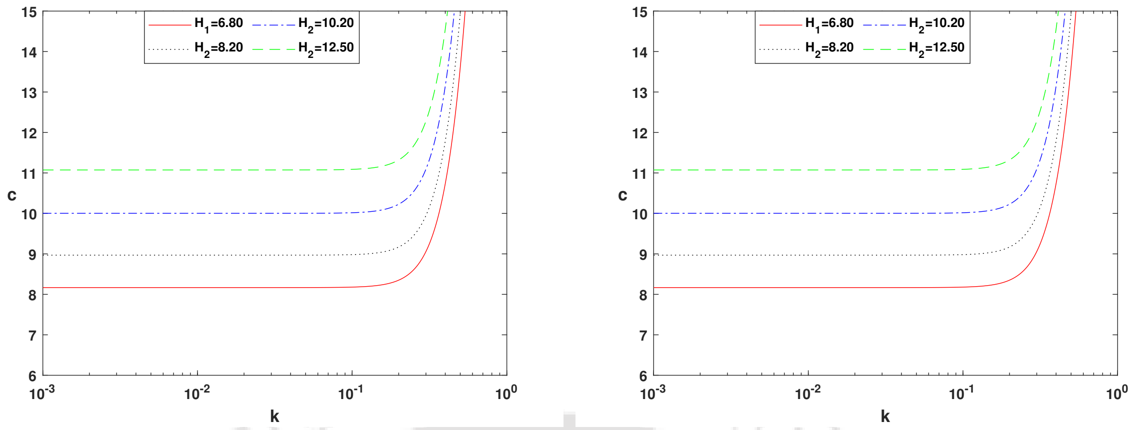

(a) (b)

Figure 6.3: Phase and group speeds variation with wavenumber under shallow-water condition. The wavenumber axis is presented on a logarithmic scale. (a) phase speed, (b) group speed.

which is a characteristic feature of shallow-water waves. In this regime, the phase/group speed depends primarily on the water depth.

The pattern of the ice sheet deflection $\xi(X)$ for a fixed trench width ($L = 50$m) with water depths ($H_1 = 6.8$m, $H_2 = 10.5$m), corresponding to various moving load speeds (V), are presented in Fig. 6.4. The boundaries of the trench region are shown by the vertical dashed lines.

Figure 6.4 demonstrates that the ice deflection amplitude increases with an increasing load speed. At low speeds, the deformation is largely confined to the neighborhood of the load position, similar to the response of a stationary point load. As the speed increases, waves are formed, and the ice response spreads beyond the trench boundaries, resulting in oscillations. The system transitions from a quasi-static response at low speeds to a dynamic regime at higher speeds, characterized by enhanced coupling between the moving load and flexural-gravity waves propagating both upstream and downstream of the trench, with large-amplitude oscillations dominating at the highest speed ($V = 5.5$m/s). Consequently, the wave generated by a load moving at a constant speed $V\,(< v_k)$ is symmetric about the load. When $V < v_k$, no energy is radiated as $X \to \infty$, since the steady-state deflection amplitude decays exponentially with distance from the load. As a result, once transient effects have dissipated, the continued motion of the load does not lead to any energy loss through wave propagation. Although the values of v_k vary with wavelength, the resulting wave pattern remains similar to that shown in Fig. 6.4, with no significant change in the overall structure of the generated waves for this case.

Figure 6.5 shows the ice deflection ($\xi(X)$) for a given load speed ($V = 5.5$m/s) and

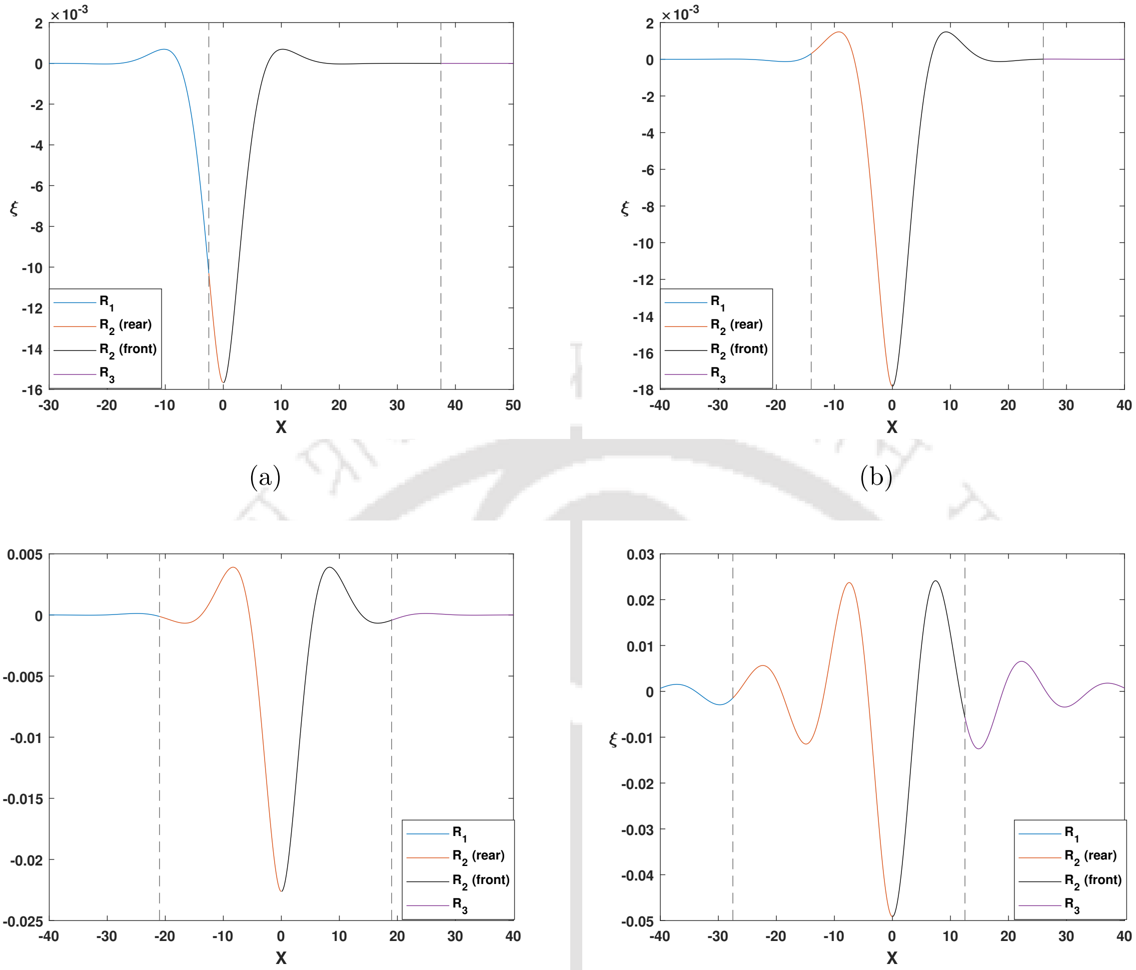

(a)

(b)

(c)

(d)

Figure 6.4: Ice sheet deflection profiles for a fixed trench width $L = 50$m and water depths $H_1 = 6.8$m and $H_2 = 10.5$m, shown for different load speeds: (a) $V = 0.5$m/s, (b) $V = 2.8$m/s, (c) $V = 4.2$m/s, (d) $V = 5.5$m/s.

trench width ($L = 50$m), while altering the trench depth (H_2). The vertical dashed lines represent the trench region. The results are displayed for four distinct depths $H_2 = 6.8$, 8.2, 10.2, and 12.5m, demonstrating the effect of the trench depth on the ice deformation response.

Within the trench region, a deflection just beneath the load is observed for all depth cases. As the trench depth increases, the magnitude of this central deflection decreases slightly. The amplitude and wavelength of these oscillations are influenced by the trench depth. Shallower trench depths produce relatively larger oscillation amplitudes, whereas deeper trenches lead to smoother profiles with reduced wave amplitudes. Although the overall shape of the deflection profiles remains similar for all depths, increasing H_2 systematically modifies both the peak deflection within the trench and the amplitude of

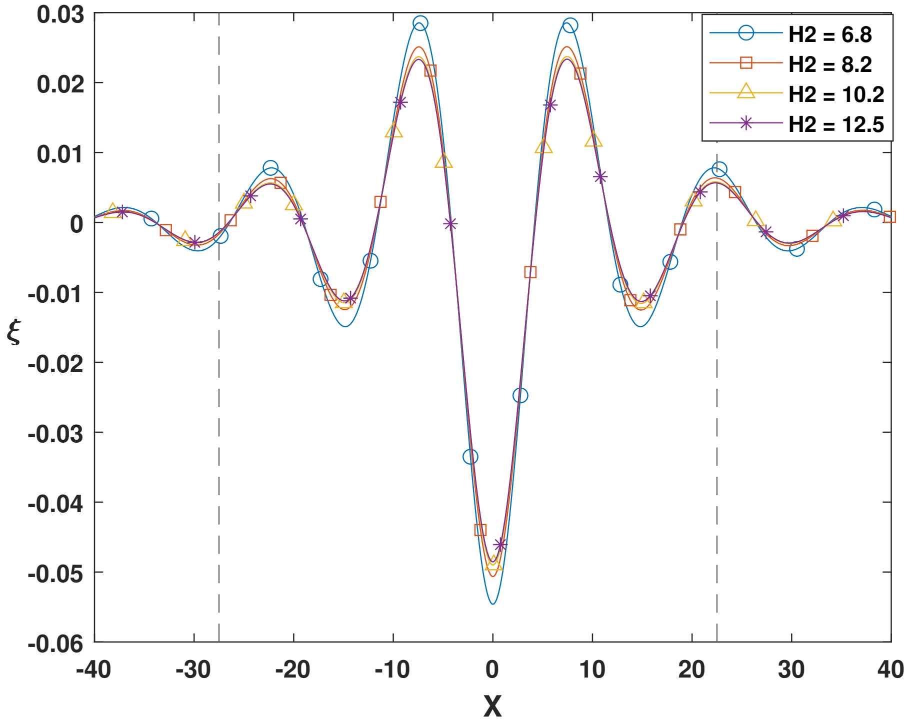

Figure 6.5: Ice sheet deflection profiles for a load speed $V = 5.5$m/s and trench width $L = 50$m, illustrating the effect of varying trench depth on the deflection of ice sheet

oscillations outside it.

Figure 6.6 illustrates the variation in the ice sheet deflection profiles for a fixed load speed of $V = 5.5$m/s and constant water depths against $X = x - Vt$. The trench geometry is varied by changing its width, while keeping the first trench edge fixed and shifting the second edge. It is observed that, when the trench is narrow, the generated waves continue to propagate into Region 3, producing noticeable disturbances there. However, as the trench width increases, the wave disturbance in Region 3 gradually diminishes and eventually becomes negligible. Despite this change in wave transmission, the peak deflection amplitude remains essentially unchanged for different trench widths, indicating that trench width primarily affects wave propagation rather than the magnitude of the ice deflection.

The smooth wave behavior observed at the trench edges is a consequence of both physical continuity and mathematical constraints of the ice-water system. Since the ice sheet remains continuous across regions of varying water depth, abrupt changes in deflection or slope are physically inadmissible. Mathematically, the governing fourth-order flexural-gravity wave equation requires continuity of deflection, slope, bending moment, and shear force at the trench boundaries. These matching conditions ensure a smooth transition of the wave field across the trench edges, even in the presence of depth variations, and prevent the formation of discontinuities in the deflection profile.

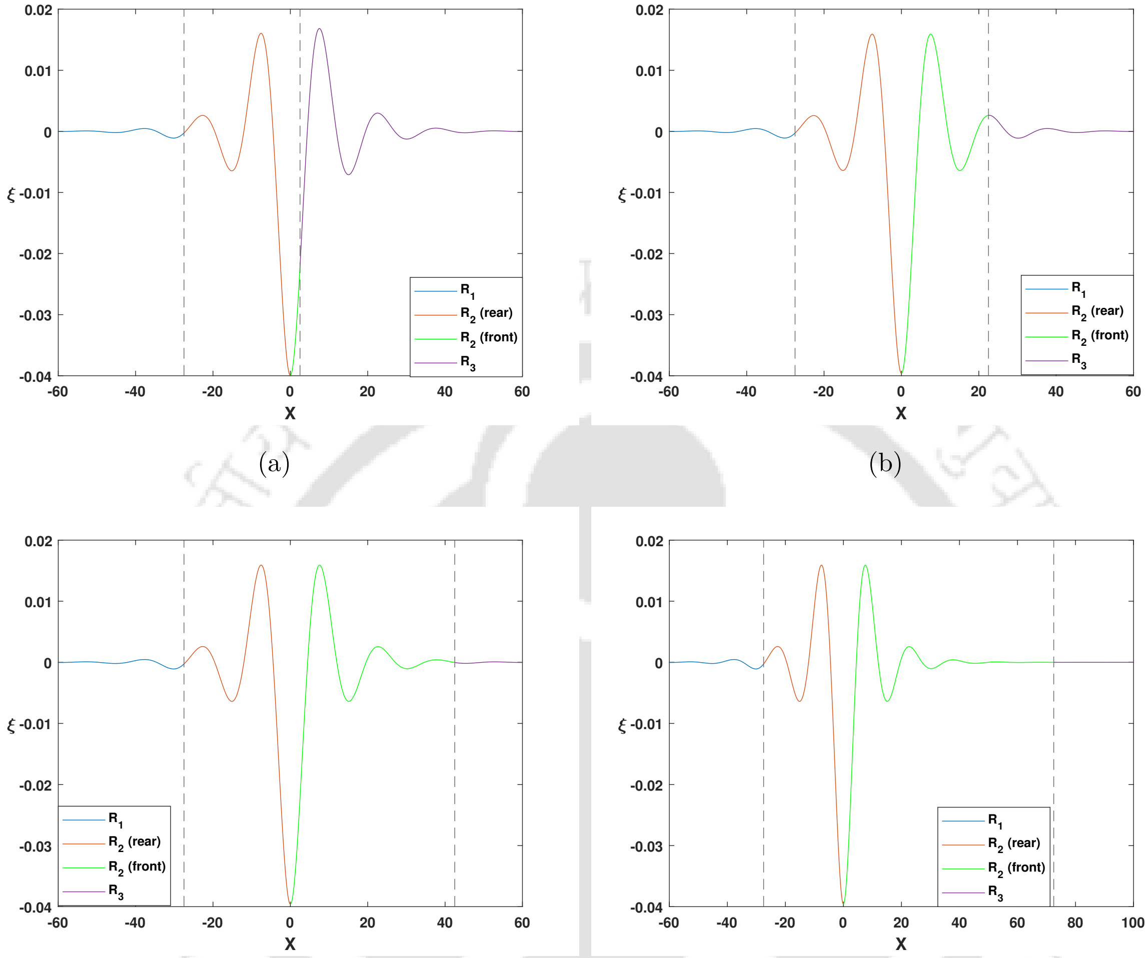

(a) (b)

(c) (d)

Figure 6.6: Ice sheet deflection profiles for $V = 5.5$m/s and water depths $H_1 = 6.8$m and $H_2 = 10.5$m, shown for different trench width: (a) $L = 30$m, (b) $L = 50$m, (c) $L = 70$m, (d) $L = 100$m.

6.4 Conclusion

The wave response of a thin floating ice sheet under a moving load in the presence of a rectangular trench is examined in this study using a mathematical model. Together with the necessary boundary and continuity requirements related to the trench geometry, the governing equations defining the coupled ice-water system are established. The fluid domain is divided into three virtual regions to account for the influence of the trench, and appropriate matching conditions are applied at the virtual boundaries. The analysis is made simpler by using a plane-wave approximation. Continuity of slope, bending moment, and shear force are among the continuity requirements associated with ice deflection that are imposed at the ice-water interface.

The governing equations are simplified to a set of ordinary differential equations by introducing a moving coordinate system in order to calculate the ice sheet deflection. Applying the conditions at the location of the moving load yields the desired analytical solutions and a piecewise equation for the ice deflection. Within a certain range of load speeds, the resultant solution remains feasible.

The analysis demonstrates that the ice sheet response is significantly influenced by trench depth. The ice deflection decreases as the trench depth increases, suggesting that deeper trenches reduce the deformation of the ice sheet. Additionally, the deflection profile is similar to a stationary load for very low load speeds. Wave generation intensifies and the dynamic wave response of the ice sheet takes center stage as the load speed rises.

The findings are applicable to ice-structure interaction problems in polar and subpolar locations, and they provide a foundation for future extensions that may include nonlinear effects, regionally changing ice characteristics, and more complex trench geometry.

CHAPTER 7

Summary and future directions

The outcomes and contributions of this thesis are briefly outlined in this chapter. It also offers a framework for possible future investigations and expansions of the present study.

7.1 Summary

This thesis includes a comprehensive mathematical and analytical examination into wave generation and ice sheet deflection due to moving loads on a floating ice sheet under a variety of realistic circumstances in the environment. The study methodically investigates the interaction between the ice cover and sea-bed properties, external forces, and hydrodynamic effects, and how these interactions affect wave propagation, phase and group speeds, and ice deflection patterns.

Chapter 2 provides a mathematical model for the study of wave generation and deflection of a floating ice sheet subjected to a moving concentrated line load over a porous sea-bed. The analysis focuses on the influence of sea-bed porosity and in-plane stress on the dispersion characteristics, particularly the phase and group speeds of flexural-gravity waves. A significant modification in phase speed is observed at small wavenumbers when sea-bed porosity is taken into account, while the minimum phase and group speeds remain similar to those corresponding to an impermeable sea-bed. However, the presence of in-plane stress is shown to considerably affect both phase and group speeds.

The study further reveals that sea-bed porosity influences the amplitude of ice deflection without altering the wavelength of the generated waves. Increasing either the porous-effect parameter or the stress parameter results in a reduction in wave amplitude. Two critical load speeds are identified for the porous sea-bed case, at which the ice displacement grows proportionally to $(t^{1/2})$, while for other speeds, the response approaches a steady state with algebraically decaying transients. These findings highlight the important role of sea-bed permeability in modifying transient and near critical responses of floating ice sheets under moving loads.

Chapter 3 presents an analysis with the incorporation of sea-bed topography in the form of a sinusoidal ripple bed. A mathematical model is proposed to examine the interaction between a moving load, a floating ice sheet, and an undulating sea-bed. By representing the moving load using Dirac delta and Heaviside step functions, the ice deflection is expressed in an integral form, and asymptotic methods are employed to evaluate the dominant wave contributions across different load speed regimes.

The results demonstrate that sea-bed ripples significantly influence the ice sheet response, with increasing ripple amplitude producing stronger disturbances in the ice sheet. The phenomenon of Bragg resonance plays a crucial role in shaping the wave field. Although larger ripple amplitudes lead to enhanced wave interactions, the deflection directly beneath the moving load decreases. The study also shows that the wavelength of the waves ahead of the load decreases with increasing load speed, while longer waves develop behind the load, eventually forming a shadow zone at very high speeds. As the ripple frequency increases, the ice deflection converges to that obtained for a flat sea-bed, indicating the diminishing influence of short wavelength bottom undulations.

In **Chapter 4**, the wave response of a floating ice sheet under a moving load is examined in the presence of a uniform underlying current and a flexible sea-bed modeled as an elastic plate. Using Fourier transform techniques and asymptotic analysis, the dispersion relation is derived and studied under various physical assumptions. The analysis shows that, in the absence of current and bottom elasticity, both phase and group speeds approach the classical gravity wave speed for long waves and attain minimum values at intermediate wavenumbers.

When the bottom elasticity is included, the minimum phase speed is significantly altered, and the phase speed tends to infinity as the wavenumber approaches zero. The introduction of a uniform current results in a proportional shift of the dispersion curves due to the Doppler effect. While long wavelength waves are only weakly affected by the combined effects of current and bottom elasticity, noticeable changes occur in the intermediate and short wavelength regimes. The group speed increases monotonically, emphasizing enhanced energy transport at shorter wavelengths. The ice deflection beneath the moving load is found to decrease with increasing bottom elasticity, but increase with stronger uniform currents, underscoring the crucial role of sea-bed flexibility in regulating wave energy and ice deformation.

Chapter 5 investigates the response of a floating ice sheet subjected to a distributed, time-dependent moving load in the presence of a uniform current. The load is assumed to act over a finite length and to move with variable speed, including cases of constant velocity, uniform acceleration, and uniform deceleration. The governing equations are solved using the Laplace-Fourier transform technique, yielding integral expressions for the ice deflection.

The results show that the maximum deflection always occurs beneath the moving load, with the deflection profile strongly dependent on load speed, frequency, and spatial extent. As the load speed increases, longer waves appear behind the load and shorter waves form ahead of it. Increasing the load length significantly reduces the maximum deflection, indicating a more uniform distribution of stresses within the ice sheet. Load frequency and uniform current are also found to influence both the amplitude and spatial distribution of the deflection. For accelerating loads, higher acceleration leads to quasi-static behavior, whereas lower acceleration produces more disturbed wave patterns. In the case of decelerating loads, gravity waves approaching from behind eventually dominate the response near the load position.

Chapter 6 examines the wave response of a floating ice sheet under a moving load in the presence of a rectangular trench in the sea-bed. By dividing the fluid domain into multiple regions and imposing appropriate continuity conditions at the interfaces, analytical solutions for the ice deflection are obtained using a plane-wave approximation and a moving coordinate system.

The analysis shows that trench depth has a pronounced influence on the ice sheet response. Increasing trench depth leads to a reduction in ice deflection, suggesting that deeper trenches mitigate ice deformation. At very low load speeds, the deflection profile closely resembles that due to a stationary load, while at higher speeds, dynamic wave effects become dominant. This study highlights the importance of localized sea-bed features in ice-water interaction problems and demonstrates how sea-bed geometry can significantly alter the wave response of floating ice sheets.

7.2 Future Directions

The works in the present thesis can be extended in several meaningful directions to achieve a more realistic and comprehensive understanding of ice-water-structure interactions. One important extension would be to incorporate nonlinear effects in the governing equations.

Studying the ice sheet under more realistic dynamic climatic conditions, such as time-dependent loading and changeable external forcing, is another option. In addition, stratified ocean conditions with varying densities can be represented by a two-layer fluid flow system using the existing single-layer fluid assumption.

By taking into account a porous sea-bed, which permits fluid flow within the sea-bed to interact with the water and ice sheet above, the sea-bed conditions can also be enhanced. In shallow water regions, where sea-bed permeability can have a major impact on wave damping and energy dissipation, such a model would be useful.

Future research may take into account a heterogeneous ice sheet with spatially changing material qualities including thickness, elasticity, and density rather than assuming a homogeneous ice sheet. This will enhance the accuracy of forecasts concerning deformation, wave propagation, and structural safety and more accurately reflect natural ice covers.

Furthermore, the analysis can be expanded to examine the dynamic response of the system during aircraft landing and take-off operations and to incorporate a finite length floating structure, such as a floating runway or platform. This would be highly relevant for applications in polar engineering, where logistical assistance is provided by ice covered or floating runways.

Therefore, there are still many potential to further this field of study. The analysis can be made more realistic by using models with less simplifying assumptions. However, these improvements will undoubtedly result in new computational and theoretical challenges. In order to properly examine the resulting difficulties, addressing these challenges may necessitate the creation or adoption of novel analytical approaches, numerical methods, or hybrid techniques.

Bibliography

A Aggarwal, K K Barman, S C Martha, and C-C Tsai. Water wave interaction with ice-sheet of variable geometry in the presence of uniform current. *Physics of Fluids*, 36 (4):042108, 2024.

K K Barman and S N Bora. Interaction of oblique water waves with a single chamber caisson type breakwater for a two-layer fluid flow over an elastic bottom. *Ocean Engineering*, 238:109766, 2021.

K K Barman, A Chanda, C Tsai, and T Hsu. Bragg scattering of gravity waves by a sea bed of varying depth in the presence of uniform current covered by a floating membrane. *Physics of Fluids*, 36(1), 2024a.

K K Barman, A Chanda, C Tsai, and S Mondal. Flexural-gravity wave interaction with undulating bottom topography in the presence of uniform current: An asymptotic approach. *Applied Mathematical Modelling*, 133:41–64, 2024b.

C M Bender and S A Orszag. *Advanced mathematical methods for scientists and engineers I: Asymptotic methods and perturbation theory*. Springer Science & Business Media, 2013.

B J Binder, M G Blyth, and S Balasuriya. Steady free-surface flow over spatially periodic topography. *Journal of Fluid Mechanics*, 781:R3, 2015.

P Blondeaux. Sand ripples under sea waves part 1. ripple formation. *Journal of Fluid Mechanics*, 218:1–17, 1990.

S Boral and B Ni. Dynamic response of a floating flexible plate to a localised time-periodic and moving load. *Applied Mathematical Modelling*, 143:115993, 2025.

A Chanda and S N Bora. Effect of a porous sea-bed on water wave scattering by two thin vertical submerged porous plates. *European Journal of Mechanics-B/Fluids*, 84: 250–261, 2020.

A Chanda and S N Bora. Investigation of water wave scattering by an elastic sea-bed of varying depth in two superposed fluids covered by an ice-sheet. *Ocean Engineering*, 221:108510, 2021.

M Chávez-Pichardo, M A Martínez-Cruz, A Trejo-Martínez, D Martínez-Carbajal, and T Arenas-Resendiz. A complete review of the general quartic equation with real coefficients and multiple roots. *Mathematics*, 10(14):2377, 2022.

M Chávez-Pichardo, M A Martínez-Cruz, A Trejo-Martínez, A B Vega-Cruz, and T Arenas-Resendiz. On the practicality of the analytical solutions for all third-and fourth-degree algebraic equations with real coefficients. *Mathematics*, 11(6):1447, 2023.

H Chen, R P Gilbert, and P Guyenne. Dispersion and attenuation in a porous viscoelastic model for gravity waves on an ice-covered ocean. *European Journal of Mechanics-B/Fluids*, 78:88–105, 2019.

A D D Craik. The origins of water wave theory. *Annual Review of Fluid Mechanics*, 36: 1–28, 2004.

R A Dalrymple and J T Kirby. Water waves over ripples. *Journal of Waterway, Port, Coastal, and Ocean Engineering*, 112(2):309–319, 1986.

A G Davies. Some interactions between surface water waves and ripples and dunes on the seabed. Technical report, Institute of Oceanographic Sciences, 1980.

A G Davies. On the interaction between surface waves and undulations on the seabed. *Journal of Marine Research*, 40:331–368, 1982a.

A G Davies. The reflection of wave energy by undulations on the seabed. *Dynamics of Atmospheres and Oceans*, 6(4):207–232, 1982b.

A G Davies and A D Heathershaw. Surface-wave propagation over sinusoidally varying topography. *Journal of Fluid Mechanics*, 144:419–443, 1984.

A G Davies, E Guazzelli, and M Belzons. The propagation of long waves over an undulating bed. *Physics of Fluids A: Fluid Dynamics*, 1(8):1331–1340, 1989.

J W Davys, R J Hosking, and A D Sneyd. Waves due to a steadily moving source on a floating ice plate. *Journal of Fluid Mechanics*, 158:269–287, 1985.

E Dinvay, H Kalisch, and E I Părău. Waves generated by moving loads on ice plates: Viscoelastic approximations. *Wave Motion*, 114:1–10, 2022.

S Earnshaw. The mathematical theory of the two great solitary waves of the first order. *Transactions of the Cambridge Philosophical Society*, 8:326–341, 1847.

G Green. On the motion of waves in a variable canal of small depth and width. *Transactions of the Cambridge Philosophical Society*, 6:457–462, 1838.

A G Greenhill. Wave motion in hydrodynamics. *American Journal of Mathematics*, pages 62–96, 1886.

P Guyenne and E I Părău. Finite-depth effects on solitary waves in a floating ice sheet. *Journal of Fluids and Structures*, 49:242–262, 2014.

A D Heathershaw. Seabed-wave resonance and sand bar growth. *Nature*, 296(5855): 343–345, 1982.

R J Hosking and F Milinazzo. Two-dimensional response of a floating ice plate to a line load moving at variable speed. *Journal of Fluid Mechanics*, 938:A2, 2022.

R J Hosking, A D Sneyd, and D W Waugh. Viscoelastic response of a floating ice plate to a steadily moving load. *Journal of Fluid Mechanics*, 196:409–430, 1988.

S Hossain, S Paul, S De, and A Das. Generation of waves by moving oscillatory pressure disturbances in presence of porous bottom. *Archive of Applied Mechanics*, 92:2713–2731, 2022.

S Hossain, A Das, and S De. The influence of flexible bottom on wave generation by an oscillatory disturbance in the presence of surface tension. *Geophysical & Astrophysical Fluid Dynamics*, 117(3):177–212, 2023.

S Hossain, A Das, S De, and B N Mandal. Gravity waves generated by an oscillatory surface pressure in a two-layer fluid with a porous bottom. *Journal of Engineering Mathematics*, 143:2, 2023a.

C Huang, C Chen, and H Chang. Propagation of water waves over permeable rippled beds. *Ocean Engineering*, 38(4):579–591, 2011.

S Jain and S N Bora. Impact of two vertical porous barriers in reflection of water waves and mitigation of wave forces on a rigid floating structure with consideration of uniform current over a porous sea-bed. *International Journal of Applied Mechanics*, 16(4): 2450049, 2024.

P Kelland. On the theory of waves. *Report of the British Association for the Advanced of Science*, pages 50–52, 1840.

T Khabakhpasheva, K Shishmarev, and A Korobkin. Large-time response of ice cover to a load moving along a frozen channel. *Applied Ocean Research*, 86:154–165, 2019.

D Y Kheisin. Some non-stationary problems of dynamics of the ice cover. *Studies in Ice Physics and Ice Engineering (ed. GN Iakolev). Israel program for Scientific Translation*, 1971.

J T Kirby and R A Dalrymple. Propagation of obliquely incident water waves over a trench. *Journal of Fluid Mechanics*, 133:47–63, 1983.

P Kundu and R Chakraborty. Gravity wave generated by initial axisymmetric disturbance at the surface of an ice-covered ocean with porous bed. *Journal of Marine Science and Application*, 20(4):632–645, 2021.

J Lighthill. *Waves in Fluids*. Cambridge University Press, 2001.

Y Liu and D K P Yue. On generalized bragg scattering of surface waves by bottom ripples. *Journal of Fluid Mechanics*, 356:297–326, 1998.

P Maiti and B N Mandal. Water wave scattering by an elastic plate floating in an ocean with a porous bed. *Applied Ocean Research*, 47:73–84, 2014.

Z V Malenko and A A Yaroshenko. Flexural-gravity waves in an ice cover exited by periodically varying moving perturbations. *Fluid Dynamics*, 59:415–426, 2024.

A Marchenko. Damping of surface waves propagating below solid ice, 2016. Paper presented at the The 26th International Ocean and Polar Engineering Conference, Rhodes, Greece, June 2016.

S C Martha and S N Bora. Oblique surface wave propagation over a small undulation on the bottom of an ocean. *Geophysical and Astrophysical Fluid Dynamics*, 101(2):65–80, 2007.

C C Mei. Resonant reflection of surface water waves by periodic sandbars. *Journal of Fluid Mechanics*, 152:315–335, 1985.

J Miles and A D Sneyd. The response of a floating ice sheet to an accelerating line load. *Journal of Fluid Mechanics*, 497:435–439, 2003.

F Milinazzo, M Shinbrot, and N W Evans. A mathematical analysis of the steady response of floating ice to the uniform motion of a rectangular load. *Journal of Fluid Mechanics*, 287:173–197, 1995.

S C Mohapatra and T Sahoo. Surface gravity wave interaction with elastic bottom. *Applied Ocean Research*, 33(1):31–40, 2011.

S Panda and S C Martha. Interaction of water waves with small undulations on a porous bed in a two-layer ice-covered fluid. *Journal of Marine Science and Application*, 12: 381–392, 2013.

E I Părău and F Dias. Nonlinear effects in the response of a floating ice plate to a moving load. *Journal of Fluid Mechanics*, 460:281–305, 2002.

A V Pogorelova, V M Kozin, A A Matiushina, and A O Goncharic. Moving load on ice plate of varying thickness. In *ISOPE Pacific/Asia Offshore Mechanics Symposium*, pages ISOPE–P. ISOPE, 2016.

B Rayleigh. On waves. *Philosophical Magazine*, 5:257–279, 1876.

J S Russell and S J Robinson. Report on waves. *Report of the British Association for the Advancement of Science*, pages 417–496, 1837.

S Saha and S N Bora. Elastic bottom effect on trapped waves in a two-layer fluid. *International Journal of Applied Mechanics*, 7(2):1550028, 2015.

S Saha, S K Mohanty, and S N Bora. Flexural gravity wave resonance in the presence of current. *Journal of Waterway, Port, Coastal, and Ocean Engineering*, 148(3):04022003, 2022.

R M S M Schulkes and A D Sneyd. Time-dependent response of floating ice to a steadily moving load. *Journal of Fluid Mechanics*, 186(8):25–46, 1988.

R M S M Schulkes, R J Hosking, and A D Sneyd. Waves due to a steadily moving source on a floating ice plate. part 2. *Journal of Fluid Mechanics*, 180:297–318, 1987.

K Shishmarev, T Khabakhpasheva, and K Oglezneva. Steady-state motion of a load on an ice cover with linearly variable thickness in a channel. *Journal of Marine Science and Engineering*, 11(5):1045, 2023.

R Silva, P Salles, and A Palacio. Linear waves propagating over a rapidly varying finite porous bed. *Coastal Engineering*, 44:239–260, 2002.

V Squire, R J Hosking, A D Kerr, and P Langhorne. *Moving Loads on Ice Plates*, volume 45. Springer Science & Business Media, 1996.

G G Stokes. On the theory of oscillatory waves. *Transactions of the Cambridge Philosophical Society*, 8:441–455, 1847.

I V Sturova. Motion of a load over an ice sheet with non-uniform compression. *Fluid Dynamics*, 56:503–512, 2021.

T Takizawa. Deflection of a floating sea ice sheet induced by a moving load. *Cold Regions Science and Technology*, 11(2):171–180, 1985.

T Takizawa. Field studies on response of a floating sea ice sheet to a steadily moving load. *Contributions from the Institute of Low Temperature Science*, 36:31–76, 1988.

L A Tkacheva. Initial-value problem on the behavior of an ice cover under the load in the presence of shear current. *Fluid Dynamics*, 57(2):173–182, 2022.

L A Tkacheva. Motion of a load on an ice cover in the presence of a current with velocity shear. *Fluid Dynamics*, 58(2):263–273, 2023.

J V Uspensky. *Theory of Equations*. Grupo Noriega Editored, Editiorial Limusa S.A de C.V.: Mexico City, Mexico, 2005.

K Wang, R J Hosking, and F Milinazzo. Time-dependent response of a floating viscoelastic plate to an impulsively started moving load. *Journal of Fluid Mechanics*, 521:295–317, 2004.

P Wang, D Q Lu, and L D Fu. Steady-state hydroelastic waves generated by a moving load in a uniform current. *Wave Motion*, 122:103190, 2023.

J T Wilson. Moving loads on floating ice sheets. Technical report, 1958.

Z Wu, Y Cheng, and S Wang. Numerical study on effect of waving bed on the surface wave. *Journal of Hydrodynamics, Ser. B*, 18(4):464–468, 2006.

Y Z Xue, L D Zeng, B Y Ni, A A Korobkin, and T I Khabakhpasheva. Hydroelastic response of an ice sheet with a lead to a moving load. *Physics of Fluids*, 33(3):037109, 2021.

X Yu. Diffraction of water waves by porous breakwaters. *Journal of Waterway, Port, Coastal, and Ocean engineering*, 121:275–282, 1995.

S Zhu. Water waves within a porous medium on an undulating bed. *Coastal Engineering*, 42:87–101, 2001.

APPENDIX A

Appendix

The zeros of Ψ_1 are the places where the phase speed (c) of waves interacts with the load speed (V), i.e.,

$$\Psi_1 = 0 \quad \Rightarrow \quad kc - kV = 0 \quad \Rightarrow \quad c = V.$$

This indicates that the zeros of Ψ_1 occur when the phase speed (c) equals the load speed (V). Physically, this corresponds to the wave generation condition, where the moving load excites waves that propagate with exactly the same speed as the load.

Furthermore, the stationary points of Ψ_1 are the places where the group speed (c_g) of the waves matches with the load speed (V), i.e.,

$$\Psi_1' = \omega' - V = 0 \quad \Rightarrow \quad c_g - V = 0 \quad \Rightarrow \quad c_g = V.$$

Thus, stationary points occur when the group speed equals the load speed. Physically, this represents conditions where the load moves in synchrony with the energy transport of the wave system, leading to enhanced energy exchange between the load and the waves.

We describe the parameters in their dimensional form and use their corresponding expressions to compute their non-dimensional values since our problem is in non-dimensional form. For the physical parameters, the following values are considered (Davys et al. (1985)): $E = 5 \times 10^9 \text{Nm}^{-2}$, $h = 2.5\text{m}$, $H = 350\text{m}$, $\nu = 1/3$, $\rho = 1000\text{kg/m}^3$, $\rho_i = 947\text{kg/m}^3$ and $g = 9.8\text{m/s}^2$.

In figure A.1, the horizontal line $V = 0.51$ (non-dimensional) is drawn across the phase speed curve $c(k)$ and the group speed curve $c_g(k)$:

- On the phase speed curve, this line intersects at two wavenumbers, denoted by k_y and k_z. These are the points where the load speed equals the phase speed of the waves.

- On the group speed curve, the same line intersects at two wavenumbers, denoted by k_a and k_b. These are the stationary points where the load speed equals the group speed.

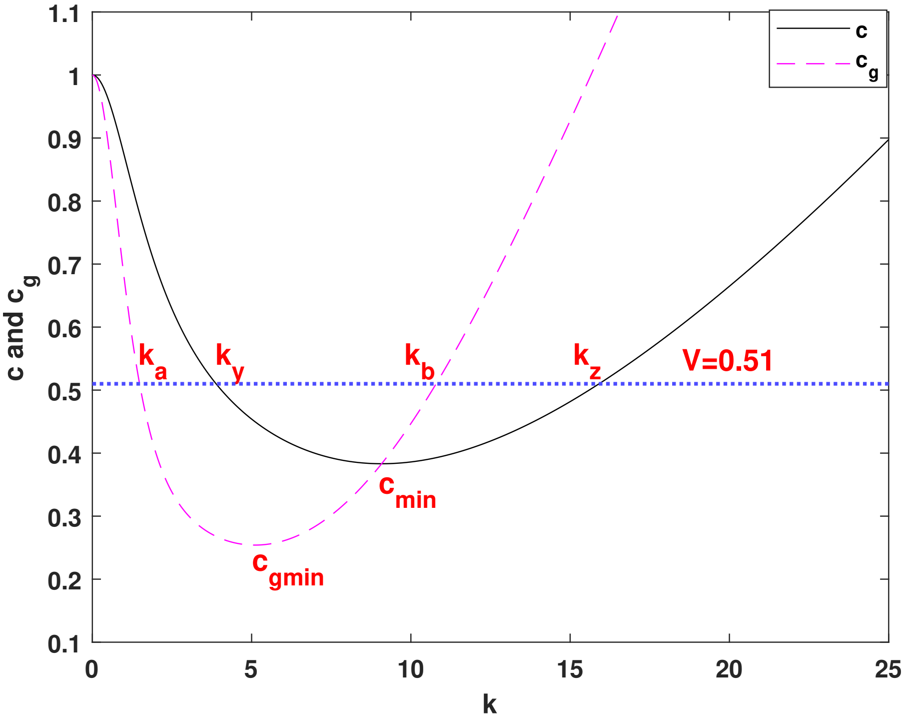

Figure A.1: Variation of phase velocity $c(k)$ and group velocity $c_g(k)$ with wavenumber k. The horizontal line $V = 0.51$ intersects the phase velocity curve at k_y and k_z (resonance points), and the group velocity curve at k_a and k_b (stationary points). These intersections illustrate the conditions for resonance ($c = V$) and effective energy transfer ($c_g = V$).

For $V \geq c_{\text{min}}$, $\Psi_1(k)$ has real zeros; therefore, the integrands $N_1(k)$ and $N_2(k)$ may have real poles. Moreover, when $V \geq c_{\text{gmin}}$, $\Psi_1(k)$ possesses stationary points. The zeros (k_y and k_z) identify the wave modes that are directly excited by the moving load, while the stationary points (k_a and k_b) indicate the wavenumbers at which the energy transfer between the load and the waves is most efficient. The combination of these conditions governs the dominant wave components generated by the moving load and determines the regions of possible resonance and energy accumulation.

It is emphasized that this explanation is provided for the general expressions of phase velocity and group velocity, without incorporating the effects of a uniform current or an elastic sea-bed. When such effects are included in the dispersion relation, the shapes of the phase and group velocity curves will get modified; however, the underlying concept remains the same. Thus, even in the presence of current and sea-bed elasticity, the physical interpretations of resonance ($c = V$) and effective energy transfer ($c_g = V$) remain valid.

Status of manuscripts out of the thesis

A. Published:

1. Mahesh Kumar Nehra and Swaroop Nandan Bora (2025), “Response of a floating ice sheet due to a moving load in the presence of a porous sea-bed.” *Journal of Ocean Engineering and Marine Energy*, **11**, 6578.
2. Mahesh Kumar Nehra and Swaroop Nandan Bora (2025), “Response of a floating ice sheet due to a moving load in the presence of an undulating sea bottom.” *Physics of Fluids*, **37**, 043603.
3. Mahesh Kumar Nehra and Swaroop Nandan Bora (2026), “Deflection of a floating ice sheet under a moving load: influence of uniform current and elastic bottom.” *Journal of Fluids and Structures*, **140**, 104465.

B. Unpublished manuscript:

1. Mahesh Kumar Nehra and Swaroop Nandan Bora (2025), “Deflection of a floating ice sheet caused by a distributed time-harmonic moving line load in the presence of a uniform current.” **(Under review).**
2. Mahesh Kumar Nehra and Swaroop Nandan Bora (2025), “Impact of sea-bed trench on the deflection of a floating ice sheet due to a moving load.” **(Under review).**